Small-scale dynamics and large-scale stability of the outer solar atmosphere

Dissertation
zur Erlangung des mathematisch-naturwissenschaftlichen Doktorgrades

"Doctor rerum naturalium"

der Georg-August-Universität Göttingen

im Promotionsstudiengang Physik
der Georg-August University School of Science (GAUSS)

vorgelegt von

Jamie S. Gorman

aus Anchorage, Alaska, Vereinigte Staaten von Amerika

Göttingen, 2024

Betreuungsausschuss

apl. Prof. Dr. Hardi Peter
Max-Planck-Institut für Sonnensystemforschung, Göttingen, Germany

Dr. Johann Hirzberger
Max-Planck-Institut für Sonnensystemforschung, Göttingen, Germany

Prof. Dr. Stefan Dreizler
Institut für Astrophysik und Geophysik, Georg-August-Universität, Göttingen, Germany

Mitglieder der Prüfungskommission

Referent: Prof. Dr. Stefan Dreizler
Institut für Astrophysik und Geophysik, Georg-August-Universität, Göttingen, Germany

Korreferent: apl. Prof. Dr. Hardi Peter
Max-Planck-Institut für Sonnensystemforschung, Göttingen, Germany

Weitere Mitglieder der Prüfungskommission:

Prof. Dr. Wolfram Kollatschny
Institut für Astrophysik und Geophysik, Georg-August-Universität, Göttingen, Germany

Dr. Lakshmi Pradeep Chitta
Max-Planck-Institut für Sonnensystemforschung, Göttingen, Germany

Prof. Dr. Ansgar Reiners
Institut für Astrophysik und Geophysik, Georg-August-Universität, Göttingen, Germany

Prof. Dr. Arnulf Quadt
II. Physikalisches Institut, Georg-August-Universität, Göttingen, Germany

Tag der mündlichen Prüfung: 29.05.2024

Printed in Germany

Contents

Summary

The Sun has long been utilized as an observatory for gaining a better understanding of high-energy plasma physics. With the advent of the space age and the continual improvement of Sun-observing instruments, physicists have gained even greater ability to see the finer details within the solar atmosphere. This has only led to more questions about how the physics of the Sun plays out.

One of the greatest questions in solar atmospheric physics has been in regards to coronal heating and the transfer of energy outward from the solar surface. Understanding the small-scale processes that are the primary components of coronal heating has become crucial for an understanding of the ultimate behavior of the solar wind. This also opens our eyes to which physical processes are actually relevant for sustained heating, and thereby the production and sustainability, of the corona. This thesis analyzes commonplace features of the solar atmosphere in order to understand and investigate energy transfer in the outer layers of the solar atmosphere.

The first work (Ch. 3) included in this thesis presents a case study of a transition region network jet. These small-scale jets are known to be highly prevalent across the solar disk and are proposed to be significant contributors to the solar wind, thereby aiding in the energy transfer through the corona. The analysis of the jet reveals multiple plasma flow components emanating from a small region of strong, mostly single-polarity magnetic field concentration. The mass flows associated with the jet, as determined from the spectral profiles of Mg II and Si IV, suggest that the jet is initiated and launched in the upper chromosphere, perhaps by magnetic reconnection, and then reaches the transition region. Although traces of the jet are not seen in the hotter coronal channels available for this observation, the energy associated with this single event matches what is required to power the solar wind, further supporting the hypothesis that such small-scale jet events are important components in coronal heating models.

The second work (Ch. 4) follows this notion up by inspecting the quiet solar corona as imaged in the extreme ultraviolet channel of the High Resolution Imager on board Solar Orbiter. While nanoflare heating and other models of coronal heating that consider a large number of discrete events (such as jets) would suggest a large number of detectable brightenings in the quiet Sun when imaged at high resolution and cadence, such as provided by this observation, no such outcome is observed. Instead, the scene appears steady and diffuse across supergranular-sized portions of the observation that make up most of the field of view. These areas of diffuse corona lack the evident structuring and highly variable intensity fluctuations that are seen in coronal bright points and loop-like regions

of the observation, despite having comparable overall intensity counts. The general diffuse nature of the observation is also significant in that it lasts for the entire 25 min observing period, raising the question of which processes could sustain such an observable phenomenon. This ultimately provides an important constriction to the heating processes of the corona, since the diffuse regions are such a dominant portion of the quiet coronal emission and therefore total coronal energy budget.

1 Introduction

1.1 Solar atmosphere

The central star of our solar system, the Sun, is often relegated as a mundane and predictable part of everyday experience, so determined by the presumed obviousness of its daily rising and setting. However, its observed physics remain anything but banal. In particular, the steep temperature increase from the lower, visible portions of the solar atmosphere (i.e., the photosphere) out towards its outer layers defies basic understanding of heat transfer in simple conductive models (see Fig. 1.1 for full-disk overview of the cooler versus hotter layers of the solar atmosphere). Thus, much of the current focus in solar atmospheric physics research is aimed at teasing out the reasoning behind this issue, including the work contained within this thesis.

1.1.1 Photosphere

The lowest layer of the Sun's atmosphere that is visible to the naked eye is the photosphere. It is from this layer that photons generated within the interior of the Sun are finally able to break free and travel out into interplanetary space. This is because the optical depth, a measure of photon absorption along a certain (column depth) travel path, becomes small enough for sufficient transmission of photons through the solar medium. With temperatures ranging roughly from 6000 K down to 4000 K, the light emitted from the photosphere is predominantly in the visible wavelength range.

A common feature of the photosphere is granulation. Granulation of the solar surface is a consequence of interior convection. Pockets of plasma rise vertically to the surface where they then diverge horizontally in the form of convection cells, the tops of which are witnessed as granulation. Thus, the lighter, inner portion of the granulation cells is the upflowing plasma that diverges outward towards the darker borders of converging downflows. These cell borders are referred to as intergranular lanes. Typical granular cells have diameters of 1000 km and lifetimes of 5–10 min, however convective patterns can be found at much larger scales (30 Mm) lasting for a day or so; these are known as supergranules. Solar surface convection is a crucial dynamic to understand because, since the plasma pressure overpowers magnetic pressure in the photosphere, it drives the motions of the magnetic field at the base of the solar atmosphere, which has important implications for atmospheric dynamics in the upper layers.

There is an exceptional hallmark of photospheric dynamics that sticks out against the

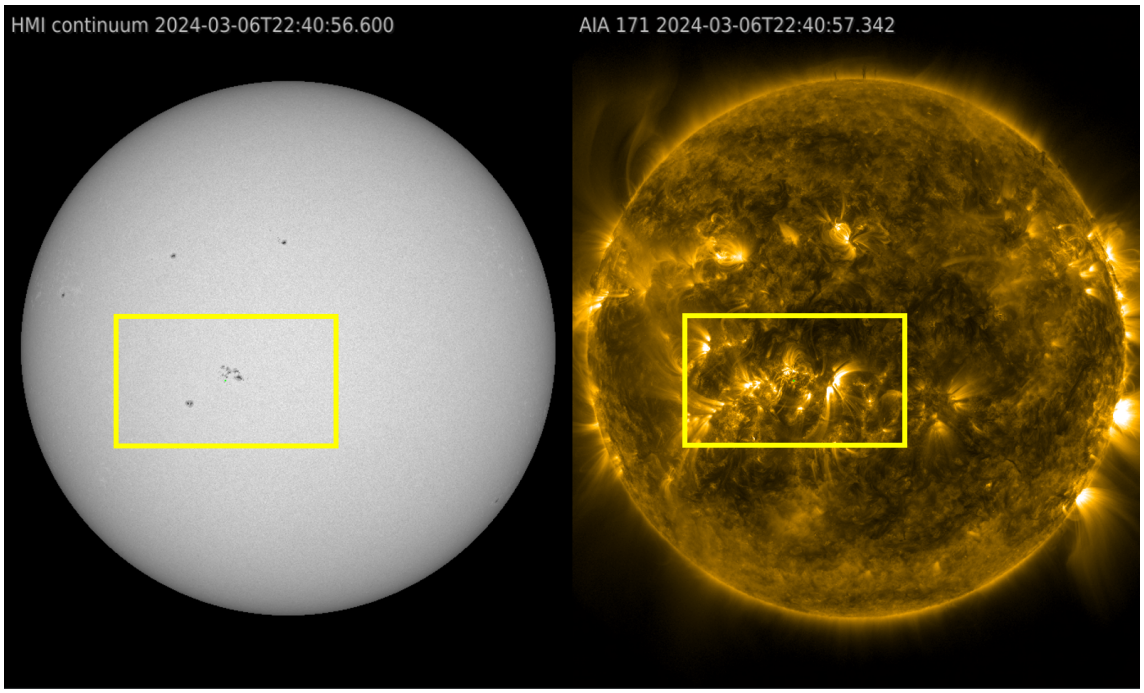

Figure 1.1: Full solar disk seen in two wavelength regimes. The image on the left shows the white light Sun as imaged by the HMI continuum filtergram (see Sect. 2.1.3 for instrument description). The image on the right shows the Sun at roughly the same time in the AIA 171Å channel (see Sect. 2.1.2 for instrument description). The yellow boxes outline the field of view shown in Fig. 1.2. Images courtesy of JHelioviewer (Müller et al. 2017).

granulation. Sunspots are strong magnetic field concentrations, whose typical diameters are around 10 Mm, that appear as dark blemishes on the surface in white light. Because the magnetic field strength (2000–4000 G) is two to ten times stronger than that associated with granulation (Lin and Rimmele 1999), the power dynamic between plasma and magnetic pressure is reversed at these locations such that the magnetic pressure dominates and suppresses the plasma convection. Consequently, the temperature in the spots is reduced by about 1000 K, which results in less emission compared to the surrounding surface.

1.1.2 Chromosphere

The next highest layer of the solar atmosphere is the chromosphere. Extending approximately 1500 km out from the surface, the chromosphere represents a layer of complex changes and dynamics. The base of the chromosphere is marked by the Sun's temperature minimum, 3800 K. However, although the density decreases with height, the temperature actually begins to increase. By the time the chromospheric layer has been fully traversed, the temperature will have increased to five times that of temperature minimum. As a result, the plasma regime transforms from being in a state of local thermodynamic equilibrium (LTE) in the dense photosphere to becoming non-LTE (nLTE), and thus the local radiation field is no longer coupled to the plasma (collisional) temperature. In addition, plasma pressure weakens with height in comparison to the magnetic pressure, resulting in a more organized, and explosive, magnetic environment.

The diverse regime of the chromosphere results in observable features that both hint at the photospheric environment below and show magnetically-dominated structures that provide a conduit for energy and mass to the atmospheric layers above. For instance, a bright network pattern can be observed in chromospheric spectral lines that roughly overlies the boundaries of supergranulation. This network pattern is linked to the large-scale magnetic field configuration, wherein the network boundaries (also called lanes) are regions of increased magnetic field concentration and, conversely, the internetwork regions constitute much weaker concentrations of magnetic field. More dynamic observables in the chromosphere are jet-like transients, such as spicules and dynamic fibrils, which are seen to occur in forest-like density at the limb or clustered about bright emission features known as active region plages, respectively. These jets are most readily observed within the chromospheric regime, but have also been seen at hotter transition region and coronal temperatures (Pereira et al. 2014, Mandal et al. 2023).

1.1.3 Transition region

A narrow interface region, commonly referred to as the transition region (TR), serves as a buffer between the chromosphere and the corona. This unique layer appears as almost a discontinuity in models of solar atmospheric temperature versus height since the temperature increases by two orders of magnitude, from 20 000 K to 1 MK, in only a few hundred kilometers. With this temperature increase, the density continues to decrease. The end result is that the plasma remains nLTE, the gas transforms from being partially to fully hydrogen ionized, and the radiative regime becomes optically-thin (i.e., small optical depth). Thus, the TR, like the corona above it and unlike the chromosphere and photosphere below, is dominated by ultraviolet (UV) and extreme ultraviolet (EUV) spectral emission lines.

The primary observational features of the TR include network structures and jets. The network structures are a vertical continuation of the network lanes found in the chromosphere, although the lanes seen in the TR tend to be larger than their chromospheric counterparts owing to the expansion of the magnetic field with height. Explosive events (EEs) are a form of randomly occurring jet seen to occur mostly in the TR (Dere et al. 1989, Teriaca et al. 2002) whose primary signature includes fast outflows away from the site of brightening (Innes et al. 1997). Emanating from the network boundaries, network jets, some of which may be the TR counterparts of chromospheric spicules, are small (widths of a few hundred km and lengths of a few Mm) yet ubiquitous. As such, they are considered to be a plausible contributor of mass and energy to the solar wind (Tian et al. 2014).

1.1.4 Corona

The corona is the hot, outermost layer of the Sun's atmosphere. In contrast to the mere ~6000 K temperature found at the solar surface, the corona has a typical temperature range of 1–3 MK, although it can reach 6 MK in areas of strong magnetic fields known as active regions or even tens of MK under flaring conditions. The plasma is also tenuous throughout this layer, with an average quiet Sun electron density range from the base to

the upper corona going from 10^8 to 10^6 cm^{-3} (Doschek et al. 1997). These characteristics result in a low plasma-β (ratio of gas to magnetic pressure) and the space-filling magnetic field dominates the movement of plasma in the corona.

The corona is often categorized into three major distinctive regions: coronal holes, active regions, and quiet Sun. Coronal holes occur in regions of open magnetic flux, often near the poles. These holes are so named because they appear dark in coronal spectral lines due to the evacuation of plasma out into the heliosphere along the magnetic field lines. Active regions, as previously mentioned, are also areas tied to strong magnetic concentrations, although in this case the field lines close back down to the surface. Active regions are bright and often associated with sunspots and plages on the surface (see Fig. 1.2). Finally, the remaining corona is poorly entitled quiet Sun because, before the advent of high-resolution spectral imaging, this part of the corona appeared to have little to no activity. Today it is known that the quiet Sun, however, is far from quiet.

The quiet Sun is home to a variety of small-scale dynamics. Coronal bright points are bright clusters of loops rooted to opposite polarity magnetic field elements (Madjarska 2019), similar to a scaled-down version of an active region. Small-scale transient brightenings, or campfires, are miniature flare-like events seen to cover the solar surface at 1 MK and are most often linked to underlying network lanes (Berghmans et al. 2021). In support of the nanoflare heating model of the corona discussed in Sect. 1.1.5, the rate of campfire occurrence is observed to increase as the event size decreases. Another broad classification (Harrison et al. 2003) of coronal transient is the blinker. Blinkers are flash-like coronal EUV brightenings that occur over small areas, and, unlike the TR EEs, are associated with density enhancements and not magnetic reconnection (Harrison 1997). Outside of these bright and rapidly evolving small-scale features, the quiet Sun is mostly composed of closed magnetic loops, which are discussed further in Sect. 1.2.

1.1.5 The coronal heating problem

The discrepancy between the very hot coronal layer and considerably cool photospheric layer of the Sun is called the coronal heating problem. In a purely convective atmosphere, the temperature should drop with distance from the surface. Since this is not the case for the Sun, other heating terms must be included in the overall energy balance. Magnetohydrodynamic (MHD) processes, including waves and magnetic reconnection, are the primary candidates that could sustain coronal heating (see Fig. 1.3 for simplified schematic comparison of proposed heating models).

Wave heating is often referred to as the alternating current (AC) model for coronal heating. Simply put, wave energy originating in the photosphere due to convective buffeting of the surface is transferred to the higher atmospheric layers via wave channeling by the magnetic field. Thus, the persistent sound waves observed at the solar surface travel upward by interacting with magnetic flux tubes, seeding MHD waves that then dissipate their energy in the outer solar atmosphere (see Sect. 1.2.3 for a more detailed description of this complex process). This is a simplified explanation, of course, as there are many obstacles to the upward transfer of wave energy generated in the lower atmospheric layers. For one, due to the density stratification of the solar atmosphere, low-frequency sound

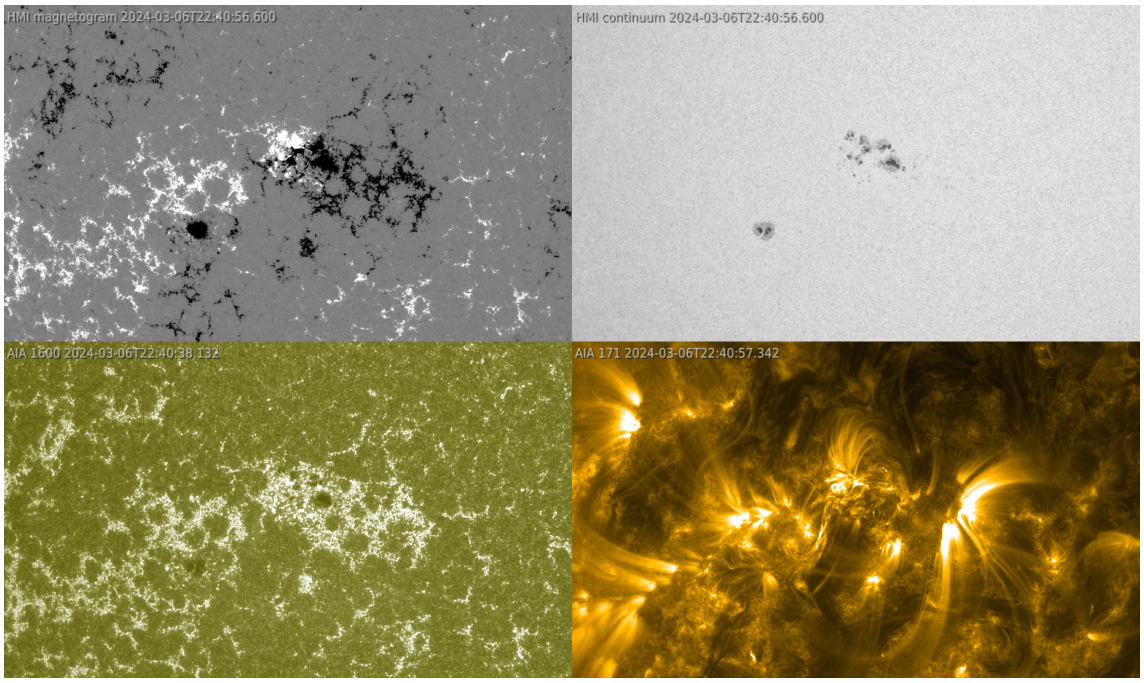

Figure 1.2: Imagery of four different solar atmospheric regimes. The images are focused on a group of sunspots as seen in the white light photosphere imaged by HMI's continuum filtergram (top right). These are associated with clusters of opposing magnetic field concentrations seen in HMI's magnetogram (top left). The AIA 1600Å channel (bottom left), which images the upper photosphere and TR in the UV, shows bright plage regions. Finally, the AIA 171Å channel, whose emission contribution is dominated by coronal plasma near 1 MK, shows the bright active regions overlying the sunspots. The FOV is the same as that highlighted by the yellow boxes in Fig. 1.1 and is approximately 575 Mm in the horizontal direction and 345 Mm in the vertical direction. Images courtesy of JHelioviewer (Müller et al. 2017).

waves generated within the Sun will be reflected in the photosphere due to the 3 min cut-off frequency found there. For another, the acoustic waves that do manage to propagate upward will steepen into shocks and dissipate their energy in the chromosphere, not the corona (Abbasvand et al. 2020). Finally, it is not clear exactly how MHD waves dissipate their energy in the corona, since the purely viscous dissipative length scales of Alfvénic waves in the coronal regime are much too large for efficient energy transfer (see, e.g., Van Doorsselaere et al. 2020, and references therein). Thus, the wave energy must first be transformed from these larger scales to smaller ones before effective energy dissipation can take place. Proposed mechanisms for this include phase mixing, resonant absorption, and MHD turbulence (see Sects. 1.2.3 and 1.2.4).

In contrast to coronal heating via MHD waves, there exists a counter theory involving more direct injections of energy via magnetic reconnection. The nanoflare heating model first proposed by Parker (1983) attributes the high temperatures of the corona to Ohmic dissipation of magnetic energy from reconnection of braided magnetic field lines. When the footpoints of field lines are shifted around at their base in the photosphere due to convective motions, this is theorized to lead to braided field lines at higher altitudes. Braided

field lines create strong currents as components of opposite magnetic polarity are brought together. The field lines will reconfigure and reconnect, resulting in their relaxation and a near instantaneous injection of kinetic energy into the surrounding plasma. These localized, impulsive heating events were termed nanoflares by Parker (1988) and determined to have an average energy of roughly 10^{24} erg per event. According to this nanoflare heating theory, there occurs a distribution of individual events whose energies range from 10^{27} erg downward, below the (then) resolution limit of observational capabilities. While larger flares observed in X-rays have energies surpassing this amount (10^{28}–10^{32} erg), Parker (1987) theorized that these larger events were actually composed of many smaller nanoflares. The primary significance of this theory is that, regardless of event size, magnetic reconnection is the driving process for flare-like events and the total occurrence of such events across a broad range of energy scales is what is heating the solar corona.

One major issue with this theory is that the number of observed flares on the Sun is too few to account for the required coronal energy budget. A variety of observational studies examining flare distributions have found that these distributions follow a power law across a range of energies. However, the rate of larger flares that occurs on the Sun is too few to explain coronal heating. Thus, an increasing number of flare-like events at smaller and smaller energy scales, such as Parker's nanoflares, are required to fill the gap. Specifically, there is a calculated power law distribution of flare occurrence to flare energy that has a critical slope steeper than -2 (Hudson 1991, Berghmans et al. 1998). While this critical slope has been found in some studies (Krucker and Benz 1998, Parnell and Jupp 2000), consistently achieving it has proven difficult (Berghmans et al. 1998, Aschwanden et al. 2000, Aschwanden and Parnell 2002, Joulin et al. 2016) due to differences in instrumentation and methodologies used for detecting individual flare-like events, the bulk of which are expected to only weakly standout against the background emission.

Currently, models for coronal heating are no longer fixated on which method, AC or DC, is dominant. Rather, it is understood that a proper heating model requires an understanding of under which regimes each mechanism is playing the leading role; then, in which proportions to add all these contributions together. The sum of this equation should be on the order of 3×10^5 erg cm^{-2} s^{-1}, or 100 W m^{-2}, to balance the losses for the quiet Sun corona (Withbroe and Noyes 1977).

1.2 Magnetic field

The magnetic field is generated on large- and small-scales within the Sun and then rises to the surface through the convective motions of the gas. At the surface, concentrations of magnetic field are able to build up in the intergranular lanes outlining the tops of the convection cells. Here in the photosphere, the gas motions dominate since plasma-β is greater than unity. The result of this is that the magnetic field is swept about by the gas flow. This changes with height in the atmosphere where plasma-β becomes less than one. In this regime, the magnetic field controls the motions of the gas such that plasma flows only along, and not across, field lines. With height, both the magnetic and plasma pressures decrease, although the plasma pressure does so at a greater rate. Thus, there is a relative increase in magnetic pressure compared to the plasma pressure, and the flux

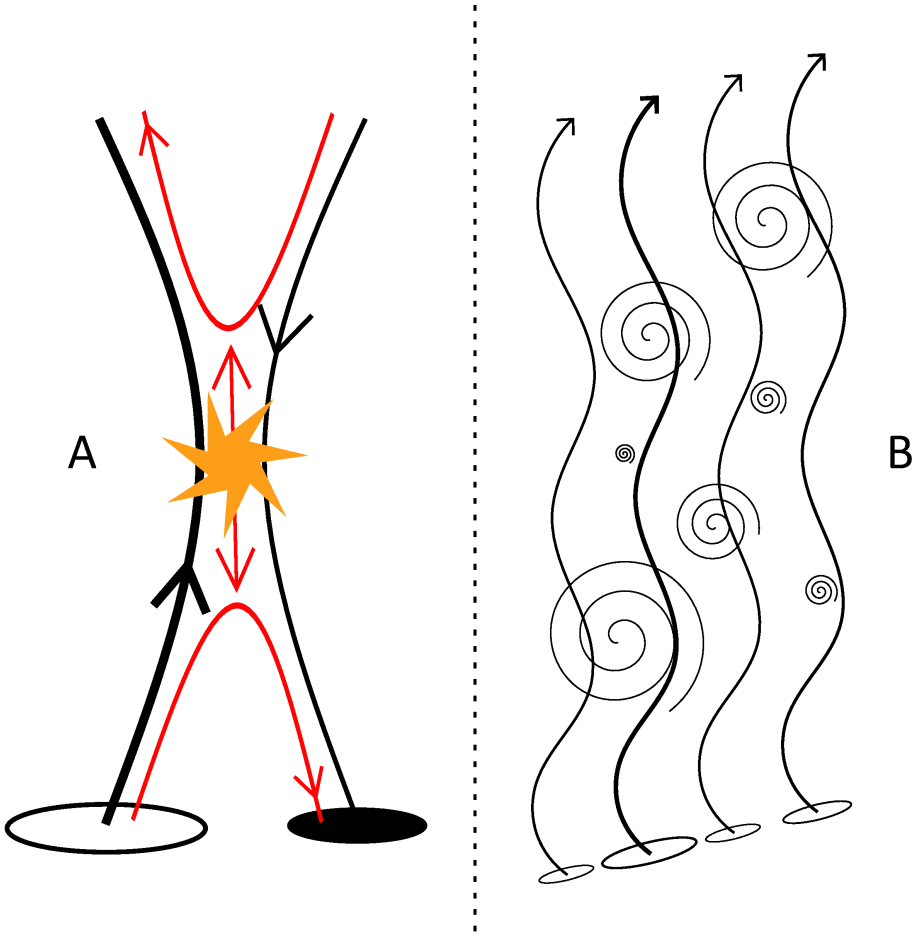

Figure 1.3: Schematic representation of basic theories of coronal heating. DC heating in the form of magnetic reconnection is sketched on the left (A), and AC heating via MHD waves and generated turbulence is sketched on the right (B).

tubes expand with height. This results in a magnetic environment where narrow flux tube footpoints are rooted in the photosphere and expand into the surrounding space with height to be space-filling in the corona.

Flux tubes will either be considered open or closed on the solar surface and rise to a variety of heights. Open flux tubes have no obvious connection back to the Sun and open up into interplanetary space, allowing for the solar wind to escape along their length. Open magnetic fields (although which are closed in the large-scale heliosphere) are most often associated with coronal holes, which are located in the polar regions during solar minimum and at lower latitudes during solar maximum. Conversely, closed flux tubes are rooted to the Sun at two different footpoints with opposing polarities. Coronal loops are denser and hotter than their surroundings and therefore stand out against the background emission (see, e.g., Reale 2014). Closed loops are characteristic of most of the solar surface and have typical heights in active regions of around 50 Mm, but can be as far-reaching as almost $2\,R_\odot$ in helmet streamers (Pneuman 1968). This all leads to a very complex magnetic configuration across the solar disk that is constantly changing due to photospheric flux emergence, cancelation, and footpoint motions, as well as reconnection

between magnetic field elements of opposing polarity in the upper atmospheric layers.

Observed dynamics related to the changing magnetic scene are numerous. On large scales, solar flares and coronal magnetic ejections (CMEs) (see respectively, e.g., Benz 2008, Webb and Howard 2012, for recent observational reviews) are perhaps the best-known results of magnetic field driven dynamics. On smaller scales, such dynamics are witnessed in different forms. Jets, such as chromospheric spicules, TR network jets, and coronal jets, are important facilitators of mass and energy movement at a wide range of length and temperature scales. Explosive events (Dere et al. 1989), Ellerman bombs (Ellerman 1917), and IRIS/UV bursts (Peter et al. 2014, Young et al. 2018) are examples of explosive brightenings resulting from magnetic field reconnection. Commonplace brightenings, such as coronal bright points (Madjarska 2019) and campfires (Berghmans et al. 2021) are also driven by magnetic field dynamics.

1.2.1 Jets

As mentioned above, jets are of particular significance to the mass and energy balance of the solar atmosphere. Easily recognized as explosive, collimated movements in intensity imagery, jets are fast, directed flows of plasma. Magnetic reconnection is the typical driver of larger types of jets (Yokoyama and Shibata 1995, Shen 2021), although even small-scale events have been linked to this process (Tian et al. 2018, Samanta et al. 2019, Chitta et al. 2023). Aside from reconnection, lower energy jets may be due to steepening acoustic shocks generated in the photosphere, as is the case for certain types of chromospheric spicules (de Pontieu et al. 2007, Heggland et al. 2007, Rouppe van der Voort et al. 2007). Regardless of the specific driver, since plasma is forced to move along field lines, the magnetic field is always involved in jet activity by channeling the plasma's outflow.

The velocity, energy density, and temperature characteristics associated with jets cover a wide range of scales. Some of the smallest jets seen to date are picoflares observed at 1 MK with Solar Orbiter. According to Chitta et al. (2023), these jets reach speeds of 100 $\mathrm{km\,s^{-1}}$, have diameters of a few 100 km, and a lower limit kinetic energy flux of 10^5 $\mathrm{erg\,cm^{-2}\,s^{-1}}$. This equates to an energy content of around 10^{21} erg per jet (in comparison, nanoflares have an energy content of 10^{24} erg per jet). Cooler (10^4 K) chromospheric spicules can reach similar velocities of 50–150 $\mathrm{km\,s^{-1}}$ (de Pontieu et al. 2007), although many only travel at 30–50 $\mathrm{km\,s^{-1}}$ (Beckers 1968). Spicules emanating from prominences are calculated to carry an energy flux of 10–1000 $\mathrm{W\,m^{-2}}$ (Chitta et al. 2019), which is on par with what is required to balance quiet Sun coronal losses. However, it has been determined that despite having such high energy and mass fluxes, most spicular material is assumed to return back to the lower atmospheric layers (Athay and Holzer 1982). Ubiquitous TR network jets imaged at temperatures between 10^4 and 10^6 K can reach apparent speeds of 250 $\mathrm{km\,s^{-1}}$ and are theorized to be a potential contributor to the solar wind (Tian et al. 2014). This is because even the slowest observed network jets have calculated energy fluxes near 4 $\mathrm{kW\,m^{-2}}$, an order of magnitude greater than that needed to power the solar wind. At larger scales, Wang et al. (1998) observed EUV coronal jets (T≈1.6 MK) ejected from polar coronal holes with impressive leading-edge velocities reaching up to around 1000 $\mathrm{km\,s^{-1}}$, although their more representative centroid velocities were typically closer to 200 $\mathrm{km\,s^{-1}}$. At hotter temperatures, Shimojo and Shibata (2000) studied X-ray

jets whose average temperature was 5.6 MK. For these events, the jet velocity was also on the order of several hundred km s^{-1} and their thermal energies ranged from 10^{27} to 10^{29} ergs.

Clearly, across the range of jet temperatures and sizes that have been observed, there exists a large source of energy available for atmospheric heating. Considering the high level of interest in jets in the study of coronal heating and solar wind generation, there remains some open questions about jet characteristics that observational solar physics still hopes to answer. For one, some have argued that apparent high-speed intensity propagations along jets are not true flows of mass but rather are merely propagating heating fronts (De Pontieu et al. 2017). If these intensity propagations are truly to be attributed to radial motions of plasma, only spectroscopic observations can prove if the perceived outward movement is actually linked to true-mass motions via the Doppler effect. Further, since the Doppler velocity is the velocity along the LOS, this value is best aligned with the jet's trajectory for on-disk observations. At the limb, the Doppler velocity is primarily a measurement of transverse motion. Thus, on-disk observations where the spectral data acquired are well-aligned with the emanating jet structure are in high-demand in order to fully tease out the quantifiable flow characteristics.

1.2.2 Magnetic reconnection

Magnetic reconnection is the reconfiguration of the magnetic field from a highly stressed state to one of a lower energy state. Since the solar magnetic field is highly dynamic and constantly evolving, this means that reconnection is a ubiquitous atmospheric process that plays a significant role in energy re-distribution.

Magnetohydrodynamics is the mathematical formalism that considers the interactions of a magnetic field in an electrically conducting fluid. In the case of ideal MHD, the plasma resistivity goes to zero, meaning that electrical conductivity goes to infinity. Also, the magnetic diffusivity, which is inversely related to electrical conductivity, becomes negligible. In practical terms, this means that the magnetic field is perfectly conducting and plasma will only flow along the field lines in a "frozen-in" state and that there is no diffusion of the magnetic field lines, either. However, there are certain conditions that will allow for this ideal state to break down.

To determine when the ideal MHD assumption is no longer valid, it is helpful to understand the implications of the magnetic Reynolds number, R_m. Similar to the Reynolds number utilized in fluid mechanics (and discussed in Sect. 1.2.4), R_m is the dimensionless ratio of magnetic induction to magnetic diffusion. Magnetic induction is the product of the flow's characteristic length and velocity scales, whereas the magnetic diffusion is encapsulated in the magnetic diffusivity term, ν, which is the inverse product of the permeability of free space and electrical conductivity. Thus, when R_m is large, as it is most often in the corona, there is no diffusion of magnetic field lines. However, when it is reduced, magnetic induction becomes less dominant and diffusivity takes over. This (i.e., small R_m) will occur either when magnetic induction is reduced via a reduction in the system's typical length and/or velocity scales, or when the magnetic diffusivity is increased via a decrease in electrical conductivity.

When field lines of opposing polarity move slowly together, so as not to generate waves, a current sheet will form in the zone between them. This thin region of increased current density allows for the diffusion of magnetic field, since the small length scales and increased resistivity will result in a reduced R_m. The magnetic field lines will diffuse across the current sheet region to reduce the overall magnetic shear, thus allowing for reconnection and reconfiguration of the magnetic topology. The end result is that the slow-moving inflow region of magnetic field is redirected through the current sheet region, that is also undergoing Ohmic heating, and quickly ejected in the outflow region. Thus, reconnection is an explosive process with the ability to provide strong, localized heating.

Observations of the Sun show a variety of reconnection signatures throughout the different atmospheric regimes. In the photosphere, where the longitudinal magnetic field is most accurately measured, concentrations of inward and outward flux are routinely seen to merge and coalesce in the reconnection-linked process of magnetic cancelation. Chitta et al. (2017a) observe chromospheric jets linked to small-scale photospheric magnetic flux cancelation wherein the average magnetic energy flux available for release is 10^9 erg cm^{-2} s^{-1}. They suggest the reconnection occurring at the coronal loop footpoints may provide enough energy for balancing coronal energy losses since the derived energy flux is two orders of magnitude greater than the magnetic Poynting flux generated by photospheric magnetic footpoint shuffling found in plage regions (as calculated in Welsch 2015). Higher up, explosive and propagating intensity brightenings such as chromospheric spicules, TR network jets, and coronal flares, are often attributed to reconnective processes, particularly when bi-directed mass flows are established. Interchange reconnection between closed magnetic field lines and the open field lines in coronal holes could be a significant source of energy for the solar wind. For example, Wang (2020) found the 10^5 erg cm^{-2} s^{-1} energy flux density associated with such a process to be consistent with the solar wind flux densities observed in-situ.

1.2.3 Magnetohydrodynamic waves

As in other dynamical systems, waves represent an efficient method for the transport of energy within the framework of MHD. Magnetohydrodynamic waves occurring in the solar atmosphere are fluctuations of a guiding magnetic field and are sometimes accompanied by density fluctuations of the plasma. These waves are seeded in the photosphere by the motions associated with granulation – primarily either through the convective buffeting of the surface layer or through random (horizontal) footpoint motions of the magnetic field. The different wave modes travel upwards in the atmosphere and, due to the complexly changing magnetic and plasma environments, these modes are either dissipated at certain locations, transformed into other wave modes, reflected, or are able to propagate outward into the solar wind (see, e.g., Nakariakov and Kolotkov 2020, for review).

There are three types of MHD waves: slow-mode magnetoacoustic (also called magnetosonic), fast-mode magnetoacoustic, and Alfvén. The two forms of magnetoacoustic modes are compression waves that either have their magnetic and gas pressure fluctuations anti-phase (slow) or in-phase (fast). Slow-mode waves damp rapidly with height and aren't expected to carry enough energy flux to power the corona (Bogdan et al. 2003), and fast-mode waves have been found to dissipate most of their energy in the chromo-

sphere where they are internally reflected (Osterbrock 1961, Rosenthal et al. 2002). Thus, it appears unlikely that the magnetosonic modes are the primary mechanisms for energy transfer from the solar surface up to the corona by themselves. Alfvén waves (also called Alfvénic waves – nomenclature discrepancies exist within the literature), on the other hand, are able to propagate through the chromosphere up into the corona (Hollweg 1978, Murawski and Musielak 2010) and so are expected to be able to transmit the greatest amount of energy from the lower atmospheric regions (De Pontieu et al. 2007). Alfvén waves are transverse, incompressible fluctuations of the magnetic field wherein the restoring force is magnetic tension. These waves travel at a characteristic speed, known as the Alfvén speed, that depends directly on the magnetic field strength and inversely on the square root of the mass density. With low density and comparatively strong magnetic fields in the corona, the Alfvén velocity exceeds the sound speed there, so field-driven dynamics are preferred. However, also due to this low density and subsequent small electron collision rate, resistivity and viscosity are very low in the corona. As a result, the dissipation of the magnetic energy via Alfvénic waves is weak considering their large typical damping length scale (e.g., for a wave traveling along a loop, the damping length is equal to the loop's radius of curvature (Wentzel 1974, Rosner et al. 1978)). Other processes must be occurring, then, in order for the effective conversion of wave energy into heat.

There are two primary MHD wave mode conversion processes that allow for effective localized wave heating in the corona, as compared to pure Alfvénic dissipation. These include resonant absorption and phase mixing. While the processes are often noted as separate, they are actually interlinked. The key ingredient for both mechanisms is inhomogeneity of the background field. This is easily achieved by the varying density profile across flux tube cross-sections. Consequently, the Alfvén speed will also vary radially across the flux tube, leading to the propagation of Alfvén waves with different phase speeds. In resonant absorption, a thin azimuthal layer within the flux tube will have a local Alfvénic frequency that matches the photospheric driving motions of the field. The transverse waves with matching phase speeds will experience a resonance with this layer and undergo mode conversion from primarily transverse to azimuthal (Ionson 1978). These azimuthal motions at the boundary of the field line introduce a velocity shear that enables efficient dissipation of the wave energy. Due to the nature of the resonant boundary layer, the energy deposition will be fairly localized. In contrast, phase mixing is effective over a wide range of frequencies, so is better able to spread heating over a larger range. Phase mixing is a component of resonant absorption and also results from variable Alfvén speeds across the field. In this picture, however, the waves traveling along neighboring field lines are out of phase and strong gradients develop that invoke frictional losses and, ultimately, heating due to viscous and Ohmic processes (Heyvaerts and Priest 1983).

While wave heating has been a historically important theory for coronal heating, calculating the energy carried by MHD waves has proved challenging due to observational constraints. One issue with determining accurate energy flux deposition in the solar atmosphere is the infeasibility of resolving the small-scale wave modes associated with energy dissipation. Another issue is that transverse Alfvén waves are, in general, incompressible. This means that diagnostics of these modes based only on intensity imagery (without spectroscopic information) could be incomplete. Despite these obstacles, sev-

eral observation-based estimates for wave heating fluxes have been computed. De Pontieu et al. (2007) reported observations of transverse magnetic waves associated with chromospheric spicules that transfer enough energy flux (120 $\mathrm{W\,m^{-2}}$) into the corona to heat the quiet Sun. In a similar vein, McIntosh et al. (2011) showed that observed Alfvénic motions in the transition region and corona had sufficient amplitudes and periods to be considered energetic enough (100–200 $\mathrm{W\,m^{-2}}$) to accelerate the solar wind, as well as to maintain the heat balance of the quiet solar corona.

1.2.4 Magnetohydrodynamic turbulence

Turbulence is considered another important mechanism for energy dissipation in the corona, especially since it can be seeded from both MHD waves and reconnection, the primary contributors to coronal heating. Turbulence allows for energy that has been injected at large scales to be transferred down through progressively smaller scales until it dissipates at the molecular level in the form of heat. This energy cascade enables kinetic energy to be transformed into thermal energy at the smallest possible scales, thereby resulting in an efficient and localized energy dump. From a solar physics perspective, this mechanism is seen as highly promising for explaining how energy transported upwards from the photosphere (e.g., MHD waves or reconnection of magnetic flux tubes) can be deposited in the upper atmospheric layers. Turbulence is found in flow regimes with large Reynolds numbers, which is the dimensionless ratio of inertial to viscous forces. When the kinetic energy of a flow overcomes its internal frictional and stabilizing forces, the flow becomes chaotic and generates vortices which interact with each other and break up into smaller sizes, leading to a downward energy cascade. This is the picture of turbulence as provided by hydrodynamics. A similar process occurs in the presence of a guiding magnetic field as is found in MHD turbulence, albeit with more complicated implications. Instead of vortices interacting with each other to produce an isotropic energy flux, MHD turbulence is now often described in terms of anti-propagating wave packets along the magnetic field. These wave packets interact in such a manner that there is a preferential direction (anisotropy) for the energy cascade that is perpendicular to the magnetic field (Shebalin et al. 1983, Sridhar and Goldreich 1994, Goldreich and Sridhar 1995). This allows for a large quantity of energy to be deposited locally over a short period of time, which is a necessary component of coronal heating. Observationally, MHD turbulence is impossible to observe directly due to the nature of the necessarily micro-length scales involved, although indirect measurements can be achieved through statistics performed on the velocity or magnetic field (Buchlin and Vial 2007). Regardless, due to the high Reynolds number in the corona and the ever-present magnetic field, turbulence most certainly plays an important role in atmospheric heating.

1.2.5 Zeeman effect

One interesting effect of the magnetic field pertains to its influence on atomic structure and subsequent alteration of the electromagnetic spectrum. In the presence of an external magnetic field, certain electron energy levels of an atom split discretely, due to the quantization of energy states, which results in multiple spectral lines in comparison to the case where no external magnetic field is present. This splitting of levels is attributed

to the interaction of the magnetic field and the atom's magnetic moment, which is due to its orbital angular momentum and electron spin. The energy difference between these split levels, and thus the amount of separation between the shifted lines of the spectrum, is directly dependent upon the strength of the imposed magnetic field. From this effect, the Zeeman effect (see, e.g., Littlefield and Thorley 1979, for a general overview), it is therefore possible to measure the magnetic field remotely using Zeeman sensitive spectral lines.

For most of the solar surface, the magnetic field is too weak to produce measurable splitting compared to the line's natural broadening, so another aspect of the Zeeman effect is used to determine the strength and orientation of the external magnetic field. As mentioned above, there are favorable lines for which the Zeeman splitting in the presence of strong fields greater than 2000 G is obvious and rather uncomplicated due to the emitting atom's orbital structure (Beckers 1971). However, most spectral line features in solar magnetic regimes do not meet these requirements, so measurements must use the Zeeman effect on line polarization to determine the presence of weak fields. When considering the orientation of the imposed magnetic field as the reference direction, the observed polarization of the emitted radiation will vary depending upon the view angle of the line of sight (LOS). From the viewer's perspective, only the circular components of polarization for the split levels that are shifted are seen if the LOS is parallel to the magnetic field, and the sign of this component flips depending upon if the longitudinal field is pointing either towards or away from the viewer. For a LOS perpendicular to the magnetic field, the transverse component of the magnetic field can be detected through the observation of all the split lines' linear components of polarization, whether they have been shifted or not. In this manner, even weak magnetic fields can be measured (Stenflo 1978).

1.3 Radiation field

To better understand the large-scale physics of the solar atmosphere, it is imperative to understand how such dynamics are actually observed and what fundamentally causes their observational output – in other words, the radiation spectrum. The Sun acts as a blackbody radiator whose outer atmospheric layers interact with the emerging radiative field to produce a distinct spectrum with varying spectral lines. From this spectrum, depending upon the intensity profiles corresponding to the various wavelength ranges, the physical processes occurring in a certain atmospheric regime can be deduced. Since the Sun has an effective temperature of 5772 K, the photosphere, from where most photons escape, has a spectrum that is primarily focused within the longer visible spectrum wavelengths. Conversely, the hotter temperatures found in the outer atmospheric layers allow for radiation at shorter wavelengths to dominate, with ultraviolet (UV) and extreme-ultraviolet (EUV) frequencies being especially important.

Not only does the characteristic wavelength range vary depending on the regime of origin, but also the type of spectral line. The two general forms of lines are either absorption or emission. For absorption lines, above a hotter emitting source there exists a negative temperature gradient (i.e., a drop in the temperature along the LOS), such as a cloud of cooler material. As the emitted photons pass through this gradient, the photons are ab-

sorbed at wavelengths corresponding to the specific atomic transitions of the plasma along the travel path. At these wavelengths, the spectrum will show a dip since there will be comparatively less emission than from the original blackbody radiator's spectrum. For an emission line, there is no preferred absorption occurring, rather there exists some hotter material along the LOS that produces more radiation at certain wavelengths compared to the cooler background emission. Consequently, extra peaks of intensity will stand out above the background continuum.

A simple spectral emission line, as is typically seen in the TR and corona, is often parameterized as a Gaussian function. This is both because of its simplicity and ease of application, as well as the dominance of thermal and instrumental broadening, which are both described by a Gaussian function. The necessary components of this function include the maximum height, position, and width. The maximum height is the calculated amount of greatest intensity. The line position corresponds to the location on the wavelength (or frequency) axis of the centroid, and also the peak intensity, of the function. A line is said to be shifted if this position is different than the calculated rest wavelength for the atomic transition in question. This Doppler shift corresponds to movement along the LOS, either away from the observer such that the line is shifted to longer wavelengths (redshift), or towards the observer such that the line is shifted to shorter wavelengths (blueshift). Finally, the width of the line is either measured as the width of the function at half the maximum intensity (FWHM) or as its standard deviation. There are several components that combine to result in the final width of the observed (and then fitted) spectral line. These primarily consist of natural broadening, instrumental broadening, thermal broadening, and non-thermal broadening. Natural broadening relates to the uncertainty of the energy of the atomic transition. This width will be greater for higher-energy lines at shorter wavelengths than for lower-energy transitions at longer wavelengths. The instrumental broadening is directly attributed to the makeup of the specific optical system being used for the observation. As such, it is often known a priori through instrumental testing. Thermal broadening, or the Doppler width, is the result of the distribution of emitting particle velocities along the LOS, which is an effect of the temperature of the plasma and follows the Maxwell distribution. Lastly, non-thermal broadening is a loose catch-all term for the remaining unaccounted-for width of the line. This is usually related to turbulence or other unresolved motions of the plasma.

While the Gaussian is the basic building block of a spectral line, things can become more complicated under a variety of circumstances. Blends occur when two or more atomic transitions occur at wavelengths close together on the spectrum. Double (or multiple Gaussians) can be found in situations where two or more unresolved structures associated with the same spectral line in roughly the same location have different Doppler velocities and will thus show a combination of two or more Gaussians near the transition's rest wavelength. Example spectra for such variable emission lines, including broadened and double-peaked Gaussians, are shown in Fig. 1.4. Finally, in a rapidly changing atmospheric regime, such as that found in the chromosphere, line reversals, wherein the observed spectral output changes from emission to absorption along the line, are common.

The radiation leaving the photosphere provides diagnostics for the coolest plasma in

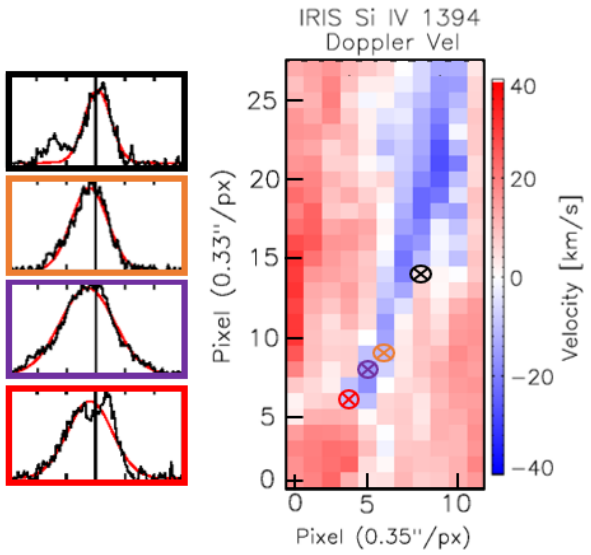

Figure 1.4: Example spectra taken by IRIS (see Sect. 2.1.1 for instrument description) with accompanying Dopplergram. Four single-pixel spectra from the Si IV 1394 Å line are shown on the left in ascending order that corresponds to their vertical location in the Dopplergram on the right. The pixel locations of the spectra are marked by a circled 'X' in the same color as that which outlines the spectra on the left. For each spectrum, the individual counts are shown by the black curve and the fitted Gaussian is shown by the red curve. The zero-velocity point is marked with a vertical black line. For the Dopplergram shown on the right, each pixel is color-coded to represent the derived Doppler velocity taken from its fitted-Gaussian with blue hues for upward motions (negative Doppler velocities) and red hues for downward motions (positive Doppler velocities). The velocity ranges from -40 km s^{-1} to 40 km s^{-1}. These data are the same as shown for the network jet event discussed in Ch. 3.

the solar atmosphere, since this layer extends from the visible surface out to temperature minimum. Being the lowest atmospheric layer, the plasma is quite dense and in a state of LTE, so that the radiation field is still well-coupled to the plasma temperature. As the temperature is decreasing with height within this region, the most obvious photospheric spectral features are absorption lines known as the Fraunhofer lines. Some of the most notable Fraunhofer lines come from the absorption of photons emitted via the hydrogen Balmer series. The Balmer series results from photon absorption leading to the excitation of the hydrogen electron from its second to third transition levels. For this to be possible, it means that a significant portion of hydrogen must not be stripped of its electron, and thus the photosphere is in a state of only partial hydrogen ionization.

Starting at temperature minimum and going outwards, the chromospheric regime contains a complex array of dynamics due to the increasing temperature and decreasing density. The state of hydrogen becomes progressively more ionized and the plasma evolves from a state of LTE to nLTE. Thus, the radiative regime is quite complicated and spectral lines exhibit very unique features compared to the photosphere or corona. For example, line reversals occur due to opacity broadening caused by nLTE effects. Essentially, under

low-density nLTE conditions, as are seen in the chromosphere, the source function for certain lines from abundant elements shows a wavelength dependence. This is not the case for most solar lines, so it is a rather unique feature for chromospheric observations. The source function in this scenario varies with wavelength, so the line wings will form at different (lower) depths than the line core. For the wings forming in the lower, cooler portions of the atmosphere, the source function is on par with the Planck function since the plasma is still in a state of LTE. With height and increasing temperature, the source function where the core is formed will no longer match the Planck function due to the shift in plasma state to nLTE. Thus, the optical thickness of the line core becomes further increased in comparison to its wings and results in a dipped, or reversed, core level.

The transition region and corona are hot, tenuous regimes in a state of nLTE. Thus, the plasma is optically thin, allowing for photons generated in the corona to escape and be observed as emission lines. Hydrogen is nearly fully ionized and the heavier elements also show high degrees of ionization. This means that the hot plasma is composed of fast-moving free electrons and, in comparison, stationary ions. The interactions between these two species set the stage for radiative emission. Radiation in the EUV and UV is generated primarily via spontaneous emission from collisionally excited ions. This occurs when a free electron interacts with an ion such that a bound electron of that ion is excited to a higher orbital level. Shortly thereafter, this excited electron will then de-excite back down to a lower, more stable level, resulting in photon emission with energy equal to the downward transition.

1.4 Motivation for this work

There remain many loose ends in the field of solar physics that require further information to be properly tied. Observational studies are of the utmost importance in this regard, because they provide the real solar constraints for answering these questions. Luckily, the current era provides an ever-burgeoning array of space missions with the Sun as their fixation, each one an improvement upon the last. An excess of data exists, waiting for proper analysis to be used in understanding the finer details of solar atmospheric heating.

The primary motivation of this thesis is to contribute to the body of knowledge surrounding the dynamics and heating of the solar atmosphere, from both the finer details at small scales to the grander implications across large scales. The preceding introduction hinted at several unknowns surrounding the nature of impulsive events that require additional probing.

For impulsive heating, as like that required in the DC heating model, observations and theory have pointed to the need for a wide range of energy injection scales, including small-scale events, events so small that they had been hitherto unresolved. Further, these events would need to occur at a high frequency to provide sufficient heating. But is this actually the case that is witnessed when the observational resolution, in both time and space, is improved? The use of the most recent data acquired by Solar Orbiter at the highest spatial and temporal scales to date should show signatures of such an ever-blinking and incoherent scene of energy injections over a broad range of energy scales in order for this theory to continue to hold water.

And what if this is not observed, then is the corona actually inherently steady as was once believed when the term 'Quiet Sun' was first coined? Perhaps wave heating, implicated in the AC model, is to blame for a steadily maintained corona. Over which length scales, then, would such coherency in heating and stability be expected to be maintained?

Returning to the idea of impulsive heating events, which indeed are observed at scales of a few Mm, what is really occurring within these so-called jets. For instance, TR network jets that contain a sizeable proportion of radiant energy have been mostly observed under conditions that make it hard to decipher if there are actual mass motions involved. This is important to know since these jets are considered a plausible source for the solar wind. It has been suggested that these jets may just be propagating intensity fronts, which would then not be able to provide mass for expulsion out of the solar atmosphere. Naturally, the answer to this question has implications for the dominant coronal heating mechanisms, depending upon whether it is determined that these jets are the result of magnetic reconnection, transverse wave motions, or traveling shock fronts. Finally, network jets are so obviously seen throughout the TR, but is the actual location of their launch also located within the TR, or is this maybe occurring elsewhere?

It is clear that the dynamics of the outer atmospheric layers of the Sun occur across a range of scales. Investigating the finer details of these ever-interesting dynamics remains a stimulating and worthwhile sector in observational solar physics, which is exactly what this work aims to achieve. The remaining thesis layout is as follows. First, a necessary chapter on the data collection and analysis methods used, including descriptions of the instrumentation providing the much-needed observations, is given as a background (Ch. 2). Next, for the questions regarding jet characteristics at a detailed level, Ch. 3 presents a case study of a TR network jet whose observed spectral features provide ample insight into some of these questions. Chapter 4 then turns to the larger scale coronal dynamics by investigating the stability of the diffuse corona seen at 1 MK and opens the door for further inspection. Finally, a discussion of the implications of these findings is given as a conclusion and motivation for future work (Ch. 5).

2 Data collection and analysis

2.1 Instrumentation

Data from several different instruments were used. In Ch. 3, observations were provided by the Interface Region Imaging Spectrograph (IRIS; De Pontieu et al. 2014b), the Atmospheric Imaging Assembly (AIA; Lemen et al. 2012), and the Helioseismic and Magnetic Imager (HMI; Scherrer et al. 2012), with the latter two instruments both being found on board the Solar Dynamics Observatory (SDO; Pesnell et al. 2012). In Ch. 4, observations were provided by the EUV High Resolution Imager (HRI_{EUV}) on board Solar Orbiter's (Müller et al. 2020) Extreme Ultraviolet Imager (EUI; Rochus et al. 2020). A description of these instruments (shown in Fig. 2.1) and their observations' processing for use in these studies are detailed in the following sections.

2.1.1 IRIS

Designed to study the TR between the chromosphere and corona, IRIS is comprised of a slit-spectrograph and an accompanying slit-jaw imager (SJI). The combined temperature range for these instruments spans from the photosphere at $\log T$ [K] = 3.7 up to the corona at $\log T$ [K] = 7.0. The spectrograph has two gratings to disperse light in separate passbands - one in the near-ultraviolet (NUV) and the other in the far-ultraviolet (FUV). This provides for spectral coverage in the wavelength ranges from 2783 to 2835 Å and 1332 to 1407 Å, respectively. The SJI also has multiple bandpass ranges, four of which are useful for solar applications: 1330, 1400, 2796, 2832. These are correspondingly dominated by emission from C II 1334/1335 Å and Si IV 1394/1403 Å in the TR, Mg II k 2796 Å in the chromosphere, and the Mg II wing near 2830 Å in the photosphere.

The novelty in IRIS lies in its ability to image the TR at high spatial and temporal resolutions with a good signal-to-noise ratio, a key necessity since the TR is a very dynamic regime changing at spatial scales of an arcsecond or less and temporal scales of a second or less. The spectrograph has a spatial resolution of 0.33″ in the FUV, which amounts to 480 km (per two pixels). The surrounding SJI, which provides excellent contextual information for interpreting the observed spectral data, has a FOV of 175 arcsec^2. The SJI shares the spectrograph's spatial pixel scale of 0.167″ per pixel. A variety of possible exposure and cadence times allow for adaptability in terms of different observation types. At the lowest possible exposure time of 2 s, a high signal-to-noise ratio is achieved in several bright lines to provide for accurate spectral analysis. Conversely, continuous eight hour observation periods can also be achieved at a high spectral cadence of 20 s along

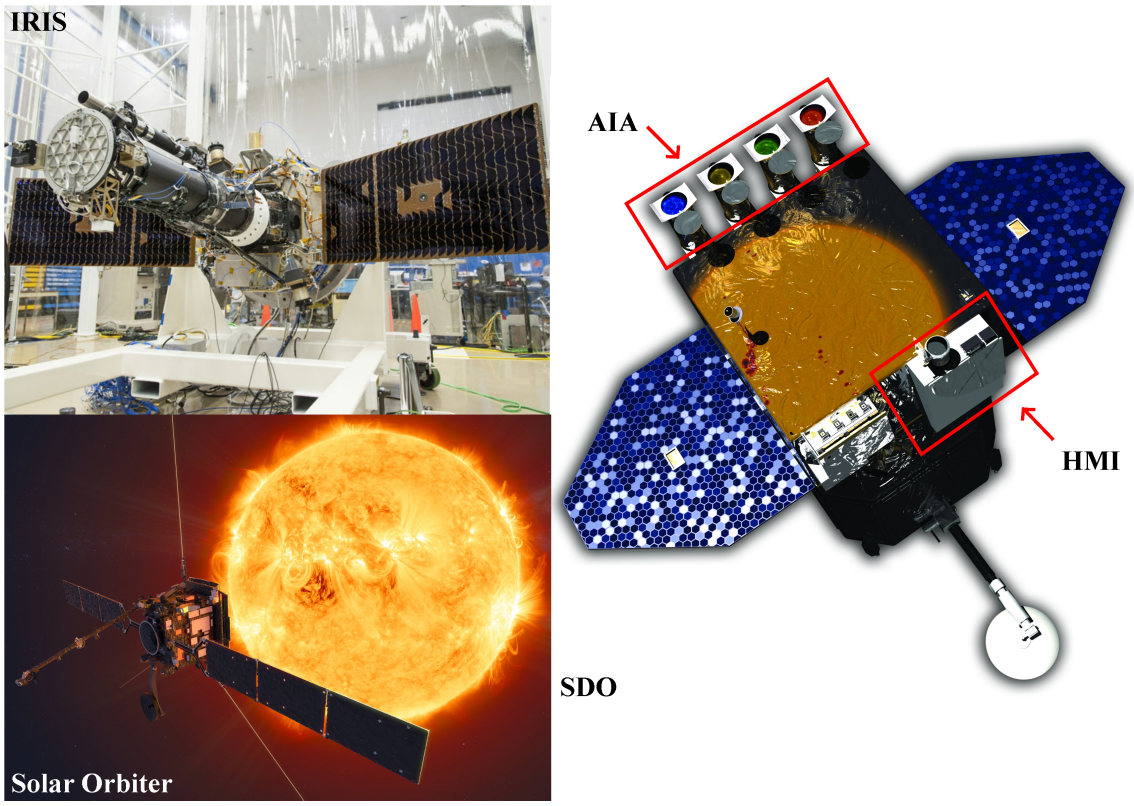

Figure 2.1: Overview of instrumentation used. Top left shows an image of the IRIS spacecraft (image courtesy of NASA). Right shows a depiction of the SDO spacecraft with its AIA and HMI instruments outlined in red (image courtesy of NASA/SDO and the AIA, EVE, and HMI science teams). Bottom left shows a depiction of the Solar Orbiter spacecraft in orbit (image courtesy of ESA/ATG medialab).

with accompanying 10 s cadence imagery. The instrument can provide scanning observation types, where the spectral slit slides across a target feature or location on the Sun, and it can also conduct sit-and-stare observations. For the sit-and-stare observations, the slit remains locked on its target feature, often at a high observational cadence.

2.1.2 SDO/AIA

The AIA images the full solar disk in ten different channels whose characteristic temperatures cover a broad range of the solar atmosphere and its dynamics. These range from temperature minimum in the photosphere at $\log T$ [K] = 3.7 up to hot coronal flare plasma at $\log T$ [K] = 7.3. The image cadences are 12 s for the EUV channels, 24 s for the UV channels, and 1 hr for the visible channel. Thus, AIA provides excellent contextual information for the entire solar atmosphere (as seen from Earth's orbit) at a nearly constant rate.

There are seven different AIA channels that are in the EUV, two in the UV, and one in the visible range. These bandpasses are achieved via the use of entrance filters and multilayer mirror coatings. Each channel has the same pixel size of 0.6″ per pixel, which

results in a theoretical spatial resolution of 1.5″, although in reality this changes slightly across the different bandpasses (see Boerner et al. 2012, for more information). The three visible/UV channels (4500 Å, 1700 Å, 1600 Å) image the photosphere and TR. The 304 Å EUV channel is centered on emission from He II and images the chromosphere and TR. The six remaining EUV channels (171 Å, 193 Å, 211 Å, 335 Å, 94 Å, 131 Å) are dominated by emission from highly ionized iron (some examples include Fe IX for AIA 171 Å, Fe XII for AIA 193 Å, and Fe XVIII for AIA 94 Å, with characteristic emission temperatures of $\log T$ [K] = 5.8, 6.2, and 6.8, respectively) and are primarily designed to image the corona under different conditions. These include active region and quiet Sun coronal environments, as well as the flaring corona.

2.1.3 SDO/HMI

Similar to AIA, HMI also provides continual full-disk imagery of the solar surface for several different types of data products at a relatively high cadence. Every 45 s, Doppler velocity, LOS magnetic flux, and continuum brightness proxy images are produced. Also, at a lower cadence of either 90 or 135 s, the vector magnetic field map for the entire solar disk is determined. The spatial scale for all data types is 0.5″ per pixel.

Only the LOS magnetic flux provided by HMI is used in this thesis, so an understanding of this data type is of particular use. HMI samples Fe I at six positions across the 6173 Å line for both right and left circularly polarized light. These 12 filtergrams are combined to calculate the Doppler velocity for both circular polarizations, the difference of which is used for computation of the LOS magnetogram (Couvidat et al. 2012). The typical noise level associated with the HMI LOS magnetograms is roughly 10 Mx cm^{-2} (Liu et al. 2012) and should be taken into account during analysis.

2.1.4 Solar Orbiter EUI

Launched in February 2020, Solar Orbiter is a multi-faceted helioscience mission with a unique elliptical orbit that allows it to acquire some of the highest resolved images of the Sun to date. The science payload includes four in-situ instruments and six remote-sensing instruments. The EUI is a part of these remote-sensing operations.

The EUI houses three telescopes: the Full-Sun Imager (FSI) and two HRIs. The suite of telescopes is optimized for imagery in Lyman-α (304 Å) and the EUV (174 Å). While the FSI has a very large FOV for an EUV imager (ranging from $(4.0\ R_\odot)^2$ to $(14.3\ R_\odot)^2$ depending upon the spacecraft distance from the Sun), the HRIs have a much smaller FOV that allows them to image the small-scale dynamics of the Sun at higher resolution. At 1 AU, the HRI FOV of 17′×17′ results in a $(1\ R_\odot)^2$ image size. However, at perihelion, this zooms into $(0.28\ R_\odot)^2$. Thus, the 0.49″ spatial pixel scale of the $\mathrm{HRI_{EUV}}$ instrument used in this work has a range of 355–100 km per pixel. The $\mathrm{HRI_{EUV}}$ can achieve an imaging cadence as high as 1 s, although this varies depending on the goal of the observation and the available data storage.

While not used in the work contained in this thesis, Solar Orbiter also hosts a dual magnetograph and helioseismology instrument called the Polarimetric and Helioseismic

Imager (PHI). Similar to HMI, PHI measures both the magnetic field at the solar surface and oscillations in LOS velocity fluctuations in order to better understand what is happening in the solar interior. Thanks to its high resolution (especially closer to perihelion) and unique vantage point, from the far side of the Sun to its polar regions, PHI will be an excellent addition to solar studies in the future, especially when observing plans are well-coordinated with the other instruments aboard Solar Orbiter.

2.2 Data analysis methods

2.2.1 Data alignment

In order to allow for proper data analysis included in this work, the observed data sets needed to undergo further alignment procedures. This alignment was outside of the built-in corrections provided by the various instrument teams at the point of data download (e.g., flat-field corrections, dark current removal, bad pixel removal, and so forth).

For Ch. 3, data from multiple instruments were used, so alignment between them was achieved through the implementation of the following series of steps:

1. Align IRIS SJI series images to one another within each separate channel:
   (a) Normalize each image by exposure
   (b) Rebin the data in both the vertical and horizontal directions to achieve a square pixel size of $[0.33'' \times 0.33'']$
   (c) Determine the transformation matrices needed for alignment using a modified version of the Interactive Data Language (IDL) procedure rigidalign1.pro[1]
   (d) Align the data set using the transformation matrices found above as input to the IDL procedure poly_2d.pro
2. Prepare AIA and HMI data for cross-correlation to IRIS data
   (a) Co-register all AIA channels and HMI to reference AIA 193 Å channel map using IDL procedure coreg_map.pro (found in the SolarSoft[2] (SSW) library) in order to correct for roll and view angles between the images
3. Cross-correlate IRIS and AIA using SJI1400 and AIA 1600 Å channels that have a similar spectral response
   (a) Determine input alignment parameters using IDL SSW procedure setpts.pro, which allows manual selection of locations of similar features seen in the different instrumental FOVs
   (b) Use the reference point coordinates outputted above (step 3a) as input for IDL procedure caltrans.pro in order to calculate the linear transformation matrix

[1] written by Lakshmi Pradeep Chitta (private communication)
[2] https://www.lmsal.com/solarsoft

(c) Use the outputted transformation matrix from step 3b as an initial guess input for the IDL SSW procedure auto_align_images.pro. The final output transformation matrix will be used in the next step

4. Align all the AIA channels to the aligned IRIS SJI data set (see step 1)

   (a) Co-register all AIA channels to IRIS1400 channel using IDL SSW procedure coreg_map.pro

   (b) Interpolate and align all AIA channels using poly_2d.pro and the transformation matrix found in step 3c. Note that AIA will now have the same resolution as the IRIS SJI data (0.33″ per pixel).

5. Align HMI to the aligned AIA 1600 Å channel using steps 3 and 4 above

For Ch. 4, the primary concern was a residual jitter within the data set. This jitter was removed in a similar manner to the data set alignment process outlined above for Ch. 3, although in a much simpler fashion. Since only rigid (non-rotational) offsets are expected through jitter, the offsets between images within the data set were determined using the rigidalign1.pro and this output was used in poly_2d.pro to create the final jitter-reduced set of images.

2.2.2 Errors

When analyzing intensity count rates or scrutinizing time-series fluctuations of any kind, it is imperative to have an understanding of the errors associated with the data. These errors provide the baseline for deciphering whether or not the variations are significant, or at least above the level of noise associated with the data. For optical systems, the final error worth considering is not only related to the photon counts involved, but also to the peculiarities of the observing instrument. The following[3] describes the calculation of errors for the observed emission analyzed in Ch. 4.

To better quantify and compare the intensity fluctuations, we calculated the total error, σ_{total}, associated with the observed emission in the following manner. First, we converted the observed spatially averaged intensities, I, from DN s^{-1} to DN by multiplying them by exposure time, t_{exp}, and then converted this to photon count by considering the current high gain estimate, a, for the HRI_{EUV} channel. Next, we used this to calculate the photon noise, σ_{ph}, by taking the square root of the total number of photons. This photon noise was then divided by the square root of the number of pixel values, N, averaged over to obtain the initial average intensity. After converting the photon noise back into DN with the conversion factor, a, the square of this amount was summed with the square of the read-out noise, R, and then the square root of this sum gave the final σ_{total}. A final, reduced equation for this is:

$$\sigma_{\text{total}} = \sqrt{R^2 + \frac{I\, t_{\text{exp}}\, a}{N}}\,, \tag{2.1}$$

[3]These paragraphs are a reproduction of Appendix A from Ch. 4 as it was originally published.

Here, σ_{total} is in DN, $R = 2$ DN, I is in DN s^{-1}, t_{exp} is in s, and $a = 6.85$ DN photon^{-1}. For a typical bright point with an average intensity of 3450 DN, we find a maximum error of 27 DN. For the diffuse regions, a typical average intensity of 2765 DN has a maximum error of 23 DN. Due to the current early stage of the Solar Orbiter mission, the error estimation calculation is not yet fully clarified. So, we expect that any reasonable calculated errors should be comparable to the root mean square (RMS) fluctuations, as these are expected as an upper limit. For this observation, the maximum errors estimated in the manner detailed above are comparable to the high-frequency (1 min) RMS fluctuations, which are typically of a few percent. Thus, we consider our error estimation to be reasonable.

3 Spectroscopic observation of a transition region network jet

[1] *This chapter's contents, including an online movie, were published in Astronomy and Astrophysics under the same title by J. Gorman, L.P. Chitta, and H. Peter (2022), A&A 660, A116, DOI:10.1051/0004-6361/202142995. Reproduced with permission from Astronomy & Astrophysics, © ESO*

Contributions to the paper: *I analyzed the data, generated the figures, and wrote the first draft of the manuscript, the majority of which has been preserved after the editing and review process.*

3.1 Abstract

Ubiquitous transition region (TR) network jets are considered to be substantial sources of mass and energy to the corona and solar wind. We conduct a case study of a network jet to better understand the nature of mass flows along its length and the energetics involved in its launch. We present an observation of a jet with the Interface Region Imaging Spectrograph (IRIS), while also using data from the Solar Dynamics Observatory (SDO) to provide further context. The jet was located within a coronal hole close to the disk center. We find that a blueshifted secondary component of TR emission is associated with the jet and is persistent along its spire. This component exhibits upward speeds of approximately 20–70 km s^{-1} and shows enhanced line broadening. However, plasma associated with the jet in the upper chromosphere shows downflows of 5–10 km s^{-1}. Finally, the jet emanates from a seemingly unipolar magnetic footpoint. While a definitive magnetic driver is not discernible for this event, we infer that the energy driving the network jet is deposited at the top of the chromosphere, indicating that TR network jets are driven from the mid-atmospheric layers of the Sun. The energy flux associated with the line broadening indicates that the jet could be powered all the way into the solar wind.

3.2 Introduction

The study of the transfer of energy from the cool, lower solar atmosphere through the transition region (TR) in order to sustain the hot corona remains an active field of research

[1] The acknowledgments for this chapter are located at the end of the thesis.

within solar physics. In particular, localized energetic events such as spicules and jets are believed to be important contributors of mass and energy to both coronal heating and the solar wind. Jets are seen at a broad range of temperatures and spatial scales, from hotter (≈ 1 MK) coronal jets with broader spires (≈ 10 Mm) (reviewed in, e.g., Raouafi et al. 2016) to much cooler (10^4 K) and narrower (down to a few hundred kilometers) chromospheric anemone jets (Nishizuka et al. 2011).

Recent observational works have been able to explore the ubiquity of jets in the TR using the Interface Region Imaging Spectrograph (IRIS; De Pontieu et al. 2014b). Transition region network jets are seen as collimated and propagating intensity fronts. These jets are ubiquitous and are generally rooted to the boundaries of network magnetic patches in the photosphere. They were first identified by Tian et al. (2014) with near-limb observations using the 1330 Å channel of IRIS' slit-jaw imager (SJI). These jet events were found to have characteristic velocities of 80–250 km s^{-1}, widths up to 300 km, and lifetimes of 20–80 s, reaching temperatures up to 10^5 K. A similar study done by Narang et al. (2016) compared network jets in the quiet Sun (QS) to their counterparts in coronal holes (CHs). The authors found that jets in CHs were longer and faster than QS jets. These differences were due to the effect of (interchange) reconnection with open field lines in CHs compared to that with the smaller, closed loops found in the QS.

Various observational and simulation studies have been designed to better understand the primary driving mechanisms behind small-scale jets, often pointing to the involvement of magnetic reconnection at different heights above the solar surface and/or upward moving shocks. Panesar et al. (2016, 2018) and McGlasson et al. (2019) have recently reported on the magnetic driver of on-disk QS coronal jets. They determined that flux cancelation at the neutral line of mini-filaments led to the eruption of these mini-filaments. This, in turn, resulted in the ejection of the jets as seen in TR plasma. A recent observational study conducted by Qi et al. (2019) examined the link between network jets and coronal plumes, concluding that jets are more energetic in regions with visible plumes. This led them to surmise that the stronger magnetic convergence witnessed in the regions with plumes creates an environment with faster shocks or more small-scale reconnection that would drive the more dynamic jets. From a simulation standpoint, Yang et al. (2018) show that flux emergence can trigger both warm ($\approx 10^5$ K) network jets and cool ($\approx 10^4$ K) spicules through reconnection and pressure gradients, respectively.

While the presence of TR jets has been well-established, a discussion regarding the veracity of their high-speed mass flows remains open. Previous studies (such as e.g., Tian et al. 2014, Narang et al. 2016, Chen et al. 2019) relied on narrow-band imagery and sit-and-stare spectroscopic scans, which made it difficult to do more than track intensity movements along the jets or transverse jet motions. There is a debate about whether or not the assumed shooting upward movement of plasma is mostly just propagating thermal fronts, wave motions, or some weighted combination of the aforementioned (Chintzoglou et al. 2018, De Pontieu et al. 2017). Specifically, Rouppe van der Voort et al. (2015) point to the need for further study of the individual line profiles to better understand noted blueward asymmetries in jet spectra. In this context, capturing an ongoing network jet event while it is happening, along with its spectroscopic properties from its photospheric footpoints into the TR, would shed light on the nature of driving mechanisms and potential

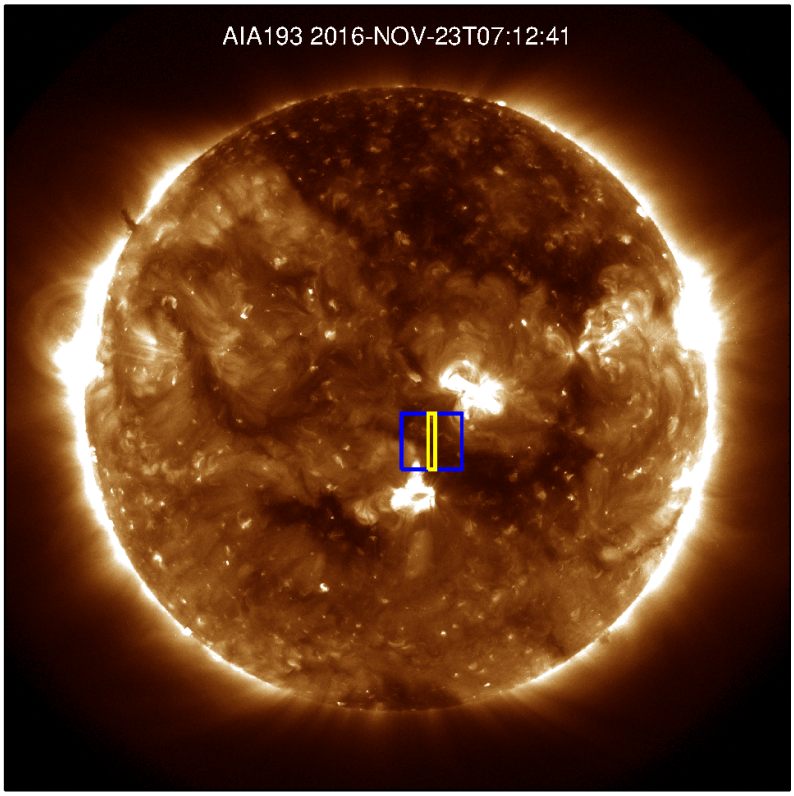

Figure 3.1: Context image. AIA 193 Å full-disk overview of the Sun on November 23, 2016, at 07:12:41 UT. The fields of view (FOV) for the IRIS raster and slit-jaw imagery are outlined in yellow and blue, respectively. Solar north is pointed up. See Sect. 3.4.

mass motions. However, such a clear spectroscopic observation of a jet event is rarely captured.

We have investigated a network jet in both narrow-band imagery and IRIS spectroscopic rasters, tracing it from its signatures in the TR down through the chromosphere to its magnetic footpoint in the photosphere. Due to the advantageous timing and spatial coverage of the raster slit, we were able to follow the spectral evolution of the jet along its (projected) length. Here, we report on the results of this analysis and provide insights into the nature of the flow of mass and energy within small-scale jets.

3.3 Observations and data analysis

IRIS observed an equatorial CH at disk-center bounded by two active regions (ARs) on November 23, 2016, from 07:12:43–07:46:33 UT. This observation, which is centered at $[x, y] = [110'', -134'']$, is comprised of a very-large dense raster scan with accompanying contextual slit-jaw imagery. The raster scanned the CH in 64 steps with 30 s exposure times (the step cadence is about 32 s, and the step size is 0.35″ in the scan direction; the observation is spatially binned such that the image scale along the slit is 0.33″ pixel^{-1}).

The raster covered a field of view (FOV) of 22″ × 175″. The entire far-UV (FUV) and near-UV (NUV) detector windows were read out. All four of the slit-jaw channels (i.e., 1330, 1400, 2796, and 2832) were operating. For the purposes of this study, only the 1400 and 2796 SJI channels are discussed. These channels recorded 16 images each, at a cadence of 127 s. The total SJI FOV was 167″×175″. For the SJI, similar to the raster, the data are binned in the y-direction. We also binned the SJI data in the x-direction during processing, resulting in a final pixel-scale of $[x, y] = [0.33'', 0.33'']$. Within each IRIS SJI channel, we normalized the images by exposure time and aligned them to one another.

We complemented IRIS data with extreme ultraviolet (EUV) observations from the Atmospheric Imaging Assembly (AIA; Lemen et al. 2012) on board the Solar Dynamics Observatory (SDO; Pesnell et al. 2012). In particular, we used AIA 193 Å EUV filter images for context. These data have a cadence of 12 s and an image scale of 0.6″ pixel^{-1}. They were normalized by exposure time and co-registered to an AIA reference map taken at 07:27:54 UT on the day of the observation.

To study the magnetic field distribution underlying IRIS' FOV, we used line of sight (LOS) magnetic field maps from the Helioseismic and Magnetic Imager (HMI; Scherrer et al. 2012) on board SDO. These HMI data have a cadence of 45 s, an image scale of about 0.5″ pixel^{-1}, and were co-registered to the reference AIA image.

Using a cross-correlation technique, we aligned the SDO and IRIS data to enable easier feature location and comparison. The final product shown here is an aligned set of AIA, HMI, and IRIS SJI maps that share the same pixel size [0.33″ × 0.33″] and orientation, with solar north pointed up. In addition to the co-aligned imagery, the original, high-resolution spectra acquired by the IRIS raster scan were analyzed. To determine TR plasma properties, we fit a single-Gaussian (SG) model to the TR Si IV 1394 Å line. This was done using the procedure iris_auto_fit.pro available in the SolarSoft[2] (SSW) library. In regions of the jet where strong deviations from a SG profile were detected, double-Gaussian (DG) fits were also performed using the SSW procedure dgf_1lp.pro, which was modified slightly to suit our needs.

3.4 Results

Overview imagery reveals the solar environment in which the jet originates. Figure 3.1 shows the full Sun as imaged by the 193 Å channel of AIA at the time of the jet observation. A crescent-shaped CH is flanked on opposite sides by two bright ARs. The jet is located at the border between the CH and the lower AR. This general environment of the jet is more readily seen in Fig. 3.2, which is zoomed into the slit-jaw FOV. The jet emanates from a magnetic network region, as outlined by bright patches in IRIS SJI1400 intensity (panel b) and HMI LOS magnetic field concentrations (panel c).

[2]https://www.lmsal.com/solarsoft

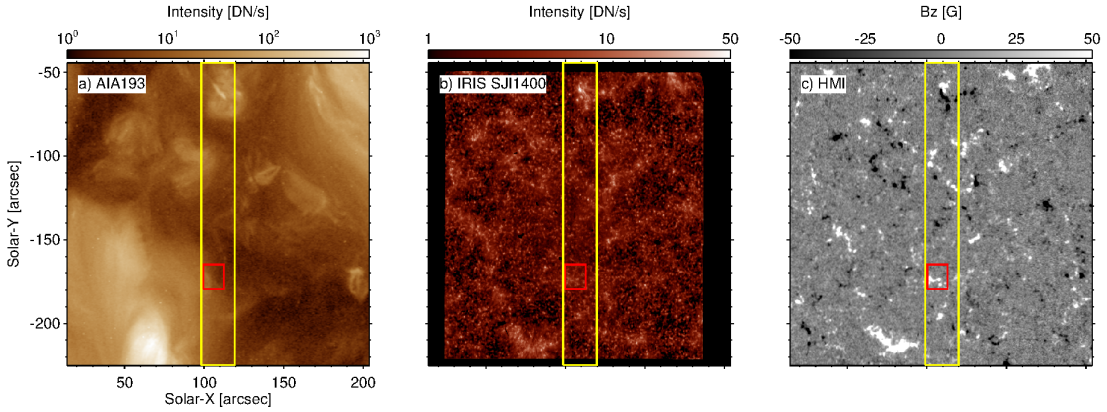

Figure 3.2: Co-aligned maps of observation for AIA 193 Å, IRIS slit-jaw imager (SJI) 1400 channel, and HMI LOS magnetogram. Each image is selected at the nearest observation time to when the jet is seen in IRIS SJI1400 at 07:21 UT. The FOV for the IRIS raster scan is outlined in yellow and the red box marks the region of interest for the network jet, which is also the FOV for panel (b) in Fig. 3.3. See Sect. 3.4.

3.4.1 Jet in the transition region

The jet's immediate surroundings across different layers of the solar atmosphere, as shown in Fig. 3.3, provide insight into the dynamics at play for this event. The clearest signal from the jet is seen in the SG-fitted Dopplergram as a strip of upflowing material (blueshifted region in panel b). Based on these fits, we find that the observed jet has a LOS velocity reaching -30 km s^{-1}.

This strip appears in the intensity imagery taken by the SJI1400 channel (panel a), and it resembles the jets seen by Tian et al. (2014). However, in our observation, the jet is only found in a single SJI frame. This is due to the SJI's low cadence of 2 min. The jet is also not easily detectable in any of the other SJI channels or in AIA. Below the jet, there is an area of increased activity in the chromospheric SJI2796 channel (panel c), and this region overlies clumps of positive polarity network magnetic field concentration seen in the HMI magnetogram (panel d).

Since the jet is only seen in one image frame, the jet's lifetime and apparent velocity within the plane-of-sky cannot be well constrained using slit-jaw images. With a cadence of 127 s, the maximum lifetime is estimated as the time between three frames, or 254 s. However, the minimum duration of observed upward-flowing material can also be constrained as the time it takes the raster to sweep across the jet. There are 7 slit positions with blueshifts recorded along the jet, with a cadence of 32 s between each position. The minimum duration of upflows is then 224 s. Together with the above estimates, this implies that the jet lifetime should be somewhere between 224 s and 254 s, that is on the order of about 4 min.

Parameters derived from the SG fits of the Si IV 1394 Å line (formation temperature $\log T$ [K] = 4.8) outline the shape and extent of the jet within the TR. Maps of the peak intensity, Doppler velocity, and full-width at half maximum (FWHM) derived from the

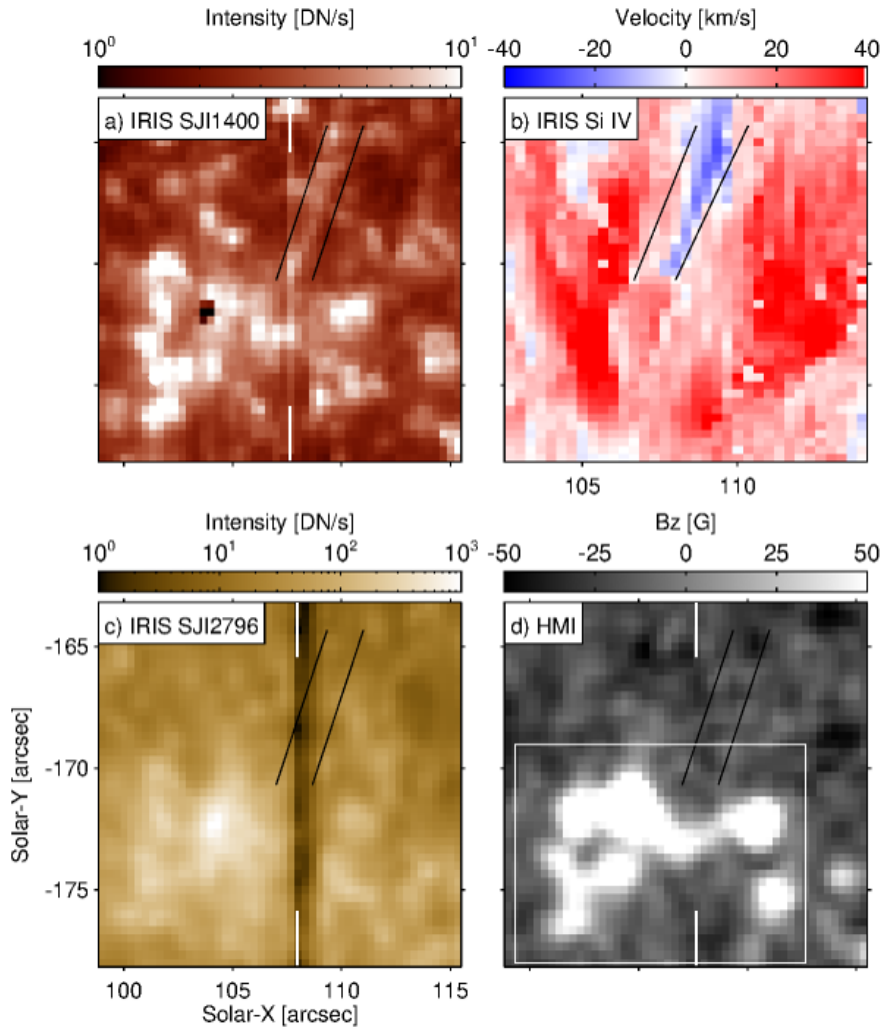

Figure 3.3: Close-up view of jet. The region of interest for the network jet is shown from four different instruments: (a) IRIS SJI1400, (b) IRIS raster Dopplergram for Si IV 1394 Å, (c) IRIS SJI2796, (d) HMI LOS magnetogram. For (b), the FOV is the same as that demarcated in red in Fig. 3.2. However, for panels (a), (c), and (d), the FOV has been extended 3.3″ (10 pixels) to the east (which is outside of the raster scan's spatial coverage) in order to fully encompass the observed activity at the jet's magnetic footpoint. For each panel, the jet is outlined in black. (a), (c), and (d) are co-aligned images taken at 07:21 UT and the location of the raster slit at that time is overplotted with white whiskers. The time evolution for panel (d) is available as an online movie published with the original article. Panel (b) is calculated from single-Gaussian fits applied to the original IRIS raster data and has a smaller FOV due to the limited spatial extent of the scan. See Sect. 3.4 for discussion.

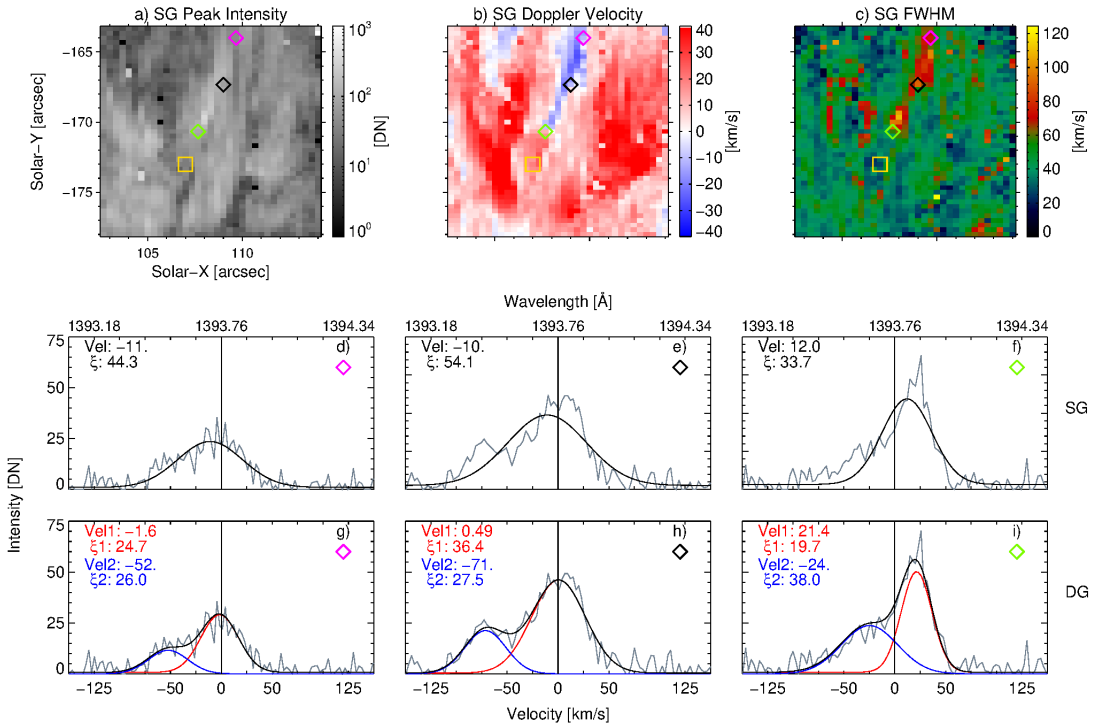

Figure 3.4: Si IV 1394 Å Gaussian parameters and selected spectra from jet. Panels (a)–(c) show the single-Gaussian (SG) parameter maps for peak intensity [DN], Doppler velocity [km s^{-1}], and full-width at half maximum (FWHM) [km s^{-1}] for Si IV, respectively. The colored diamonds mark the three individual pixels whose spectral profiles are shown in the bottom two rows, while the gold square marks, for reference, a fourth pixel whose spectrum is shown in Fig. 3.5. Panels (d)–(f) display the individual pixels' spectra in gray [DN] with the SG fitted curve overlaid in black. The Doppler velocity (Vel) and non-thermal width (ξ) are listed in the upper left. Panels (g)–(i) show the same three spectra, except a double-Gaussian (DG) fitted curve is overlaid in black and its two components are drawn in red (primary component) and blue (secondary component). The primary and secondary Doppler velocities (Vel1, Vel2) and non-thermal widths (ξ1, ξ2) are listed in the upper left. For all panels (d)–(i), a vertical black line in the center marks the location of zero-velocity, for reference. See Sects. 3.4.1 and 3.5.2.

SG fits are included in Fig. 3.4. They show that the jet consists of a narrow spire of increased intensity with broadened line widths. In comparison, directly beneath this spire are downflows (redshifted pixels) whose SG-fits have a lower peak intensity and FWHM. The Dopplergram shows a gradual increase in blueshift magnitude along the jet's spire from roughly 5–10 km s^{-1} at its base up to 30 km s^{-1} near the top.

While the parameter maps provide an overview of the event, the individual spectra are better at showing the flow structure within the jet. Spectra from three pixels representative of the upper, middle, and bottom portions of the jet are shown in panels (d)–(i) of Fig. 3.4, with either SG or DG fits applied. The SG fits plotted in the middle row seem to visually represent the observed intensities fairly well. However, most profiles along the jet show a two-component flow behavior that is best described by a DG fit (bottom row). This is supported by the reduced-chi-square metric, which is improved in virtually all cases where the DG fit is applied, with an average reduction by a factor of four. Further examples of DG-like intensity profiles are shown in Fig. 3.7.

The spectral profiles along the length of the blueshifted segment of the jet (as seen in the SG Dopplergram) exhibit a secondary blueshifted component. Such profiles with a secondary blueshifted component are observed even at those locations that are redshifted when fit with a SG. At this base, the secondary component has a blueshift of -13 km s^{-1}, which increases to almost -80 km s^{-1} farther up along the jet spire. The average secondary component velocity is -51 km s^{-1} (see Figs. 3.4 and 3.7). When comparing blueshifts, Doppler velocities of the secondary component of the DG fit are always larger than those derived from the SG fits. Panels (e) and (h) of Fig. 3.4 show the SG and DG curves for the same pixel in the middle of the jet. The DG fit secondary component has a velocity equal to -71 km s^{-1}, yet the SG fit velocity only has a line shift of -10 km s^{-1}. Comparable discrepancies can be seen all along the jet's spire. In addition to velocity, the secondary component has excess line widths ($\xi 2$; non-thermal velocity) that exceed typical non-thermal widths of 20 km s^{-1} in the TR at ≈ 0.1 MK (De Pontieu et al. 2015). We find that most of the secondary component non-thermal widths exceed this typical value, even by up to a factor of two or more. On average, the non-thermal width of the primary component is less than that for the secondary.

3.4.2 Jet as seen in the chromosphere

The jet's chromospheric activity is investigated using the Mg II 2796 Å line, which is formed in the upper chromosphere within a temperature range of roughly $\log T$ [K] = 3.7–4.2. The normalized Mg II k intensity profiles from along the jet and at its base, as plotted in panels (d)–(g) in Fig. 3.5, show that, while the Mg II intensities along the upper spire of the jet are comparable to the QS profile, they become enhanced at its base (i.e., south of the region exhibiting blueshifts in Si IV). These spectra located in the bright patch of activity beneath the jet can get to be around four times as intense as the QS (panel g). The intensity maps obtained around the k2r and k3 features of the Mg II line (panels (a) and (b) in Fig. 3.5) represent the intensities in the middle to top of the chromosphere at the base of the TR. There are still traces of the jet spire in these chromospheric layers. However, signatures of the spire are absent in the deeper layers of the chromosphere sampled with the Mg II k1r feature (see panel c). Rather, only the bright patches (associated with the

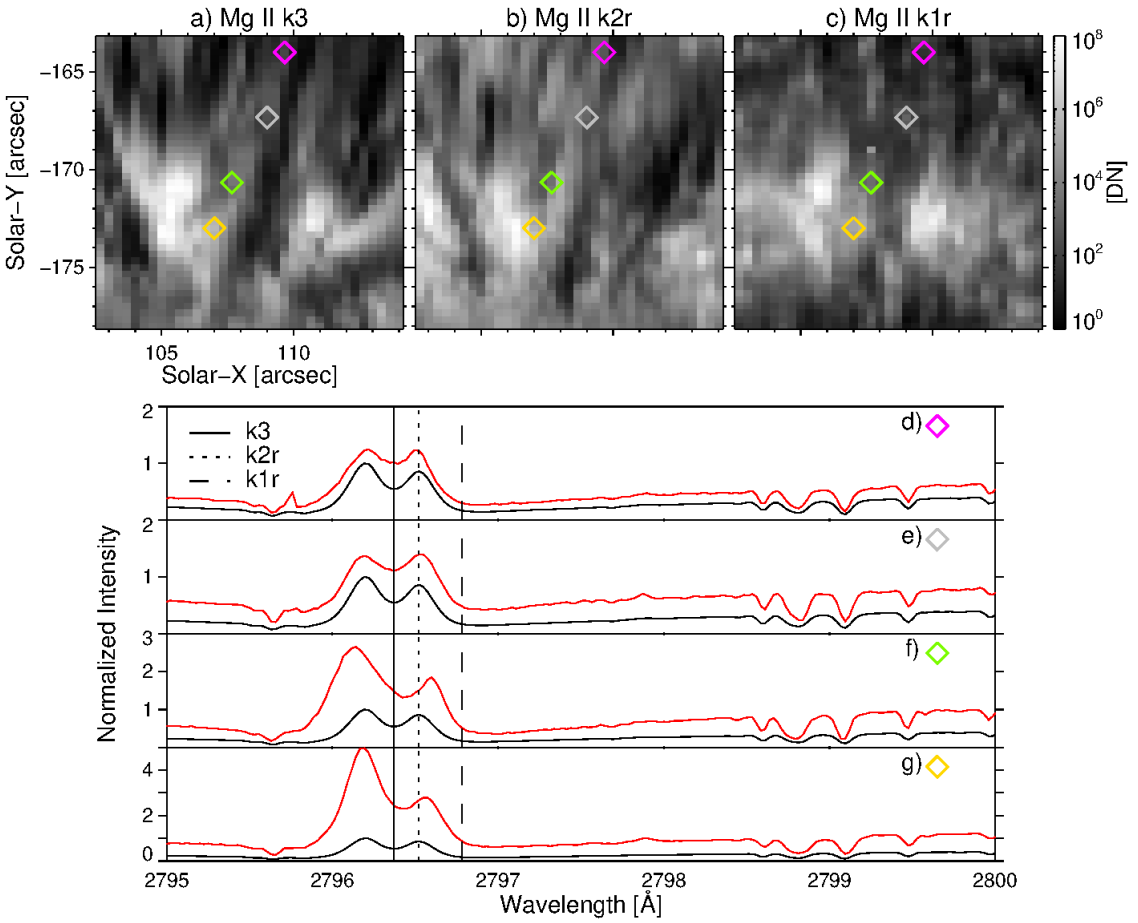

Figure 3.5: Chromospheric activity at base of jet. Maps of the intensity [DN] at three wavelength points along the Mg II line are shown in the top row. The wavelength locations are: (a) k3: 2796.37 Å, (b) k2r: 2796.52 Å, and (c) k1r: 2796.78 Å. Each map shares the same axis-scaling, spatial extent, and pixel markers as that in Fig. 3.4. Mg II k spectra from these pixels are shown in the bottom four rows, panels (d)–(g). The black curve in each panel shows the same normalized, average intensity profile for Mg II for this observation, calculated using a large portion of quiet Sun. The k3, k2r, and k1r wavelength points were selected based on the shape of this profile and are marked by the vertical solid, dotted, and dashed lines, respectively. The k2v peak of this curve is used as the normalization factor for both the averaged profile and the individual pixel profiles (red curves). See Sect. 3.4.2.

magnetic network) at the jet's footpoint are visible.

It is possible to make inferences about the speed within the chromosphere by comparing the relative shifts and intensity variations along the Mg II k line. Using the analysis procedure described in Pereira et al. (2013), the pixels near the jet's footpoint show redshifts of the k3 depression that are consistent with downflows at the top of the chromosphere of about 5–10 km s^{-1}. Intensity asymmetries between the k2r and k2v peaks can also be exploited to reveal the presence of up- or downflows. When the k2v peak is enhanced compared to k2r, as is seen for this observation at the base of the jet, this signifies that

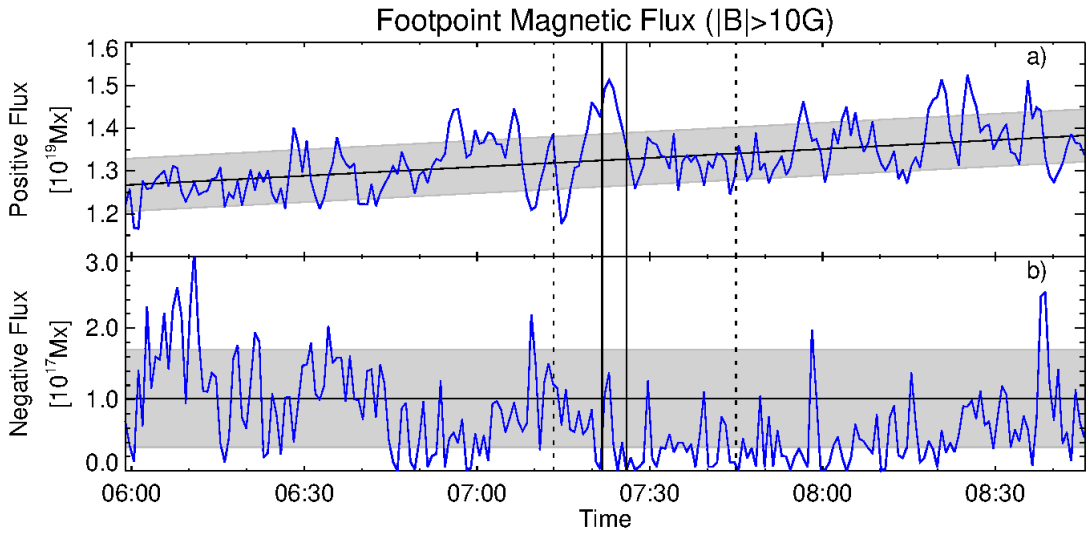

Figure 3.6: Magnetic flux vs. time at jet's footpoint. Magnetic flux of positive (panel a) and negative (panel b) polarity magnetic concentrations within the footpoint region of the jet (white box in Fig. 3.3d) for pixels stronger than 10 G are shown. The dotted vertical lines mark the start and stop times for the entire observation period of the IRIS slit-jaws: 07:13:15–07:44:58 UT. The solid vertical lines mark the period when the raster is scanning across the jet: 07:21:43–07:25:46 UT. The SJI1400 frame wherein the jet is seen occurs at 07:21:43 UT. In panel (a), the black line shows the linear trend. The gray shading covers the root-mean-square error (RMSE) from this fit. Panel (b) shows the root-mean-square (RMS) and the RMSE for the calculated values from the RMS by the black horizontal line and the gray shading, respectively. See Sects. 3.4.3 and 3.5.3.

plasma above the k2 formation height is moving downwards (see Leenaarts et al. 2013, Pereira et al. 2013). The utility of chromospheric diagnostics using shifts of the k3 depression and comparison of the k2v to k2r peak intensities has also been analyzed and confirmed by Bose et al. (2019, 2021). Thus, both of these diagnostics consistently and coherently reveal that there are downflows present in the upper chromosphere below or at the base of the jet.

3.4.3 Magnetic structure at base

The features detected in the LOS component of the magnetic field can be linked to the overlying jet structure. Comparing panels (c) and (d) from Fig. 3.3 shows that the increased chromospheric activity (i.e., radiation) beneath the jet is spatially aligned with strong concentrations of magnetic field. The raster maps from Fig. 3.5 agree with this spatial overlapping of bright Mg II intensity and magnetic field patches. The time sequence of this region reveals that the resolved clumps of positive polarity magnetic field rearrange themselves, separating and coalescing, in the period of time surrounding the jet (see online movie associated with Fig. 3.3d).

A more quantitative view of the magnetic evolution is provided by the time evolution

of the magnetic flux. Figure 3.6 illustrates how the magnetic flux, of both positive and negative polarity patches, at the footpoint of the jet changes with time. Here, the footpoint is defined by the white box in panel (d) of Fig. 3.3. To avoid noise, only pixels with magnetic flux density greater than 10 G were integrated to derive magnetic flux (this was done separately for positive and negative polarity regions). Although, selecting different cut-off strengths of 5 G, 10 G, 15 G, or 20 G showed no significant difference in the time series of magnetic flux, underlining that our results are not affected by noise. Magnetic flux contained by negative polarity patches in this region is two orders of magnitude weaker than that of the positive polarity patches. In addition, variations in the magnetic flux of negative polarity magnetic concentrations are generally within the computed root-mean-square-error (RMSE) for the whole time series. For the magnetic flux of positive polarity fields, however, a few things are noted. First, a general, linearly increasing trend is detected over the observing period of three hours. The fit to this trend was used to calculate the RMSE. Around the time of the jet, the positive flux shows strong fluctuations above the level of the RMSE. In the ten minutes preceding the jet, magnetic flux rises sharply and then decreases significantly after the jet is seen in SJI1400. There are a few other instances of such strong changes in positive flux outside of the IRIS observing time, though none are of the same net magnitude seen during the jet's lifetime.

3.5 Discussion

Most TR jet studies have been conducted using slit-jaw imagery or sit-and-stare rasters. As a result of this, any actual mass motions along a jet's trajectory are not easily identified. Propagating intensity fronts in SJIs could correspond to moving heat fronts or wave motions. Stationary-slit rasters, when at the limb, would only likely pick up transverse motions. When near disk-center, such rasters typically only cross small sections of a jet, thereby making it difficult to determine if upward flows are persistent along the rest of the structure. With this observation, however, we have the good luck that the raster scan was both co-temporal and co-spatial with the jet motions along its length, allowing for verification of the presence of mass flows and deeper inspection of spectral profiles.

3.5.1 Jet properties

Various jet properties, including the propagation speed and lifetime, can be estimated but not fully constrained, owing to various limitations of the observation. Due to the unknown inclination of the jet, exact speeds along its trajectory cannot be precisely calculated. Using the plane-of-sky propagation of the jet based only on the spatial extent of the blueshifted pixels as seen in Figs. 3.3b and 3.4b ($\approx$ 20 pixels amounting to a total length of 5 Mm) and the time it takes the raster to scan across them (7 scans at a cadence of 32 s amounting to 224 s total), it can be estimated as a lower bound that the jet propagates laterally at 22 km s^{-1}. If we further assume a simplistic triangular geometry, where the plane-of-sky speed calculated above is used for the horizontal speed and the average LOS velocity of the jet material represents the vertical velocity (51 km s^{-1}, see Sect. 3.4.1), then we can calculate a propagation speed of 55 km s^{-1}. This speed is 1.5–4.5 times lower than that determined for typical CH jets by Tian et al. (2014) and Narang et al. (2016),

but that leads us to presume the jet is traveling with speeds greater than the observational cadences are able to resolve. The projected length of the blueshifted material does agree with previous estimates (Tian et al. 2014, Narang et al. 2016), rounding out to be between 4.5 and 5.2 Mm. As we stated previously, with only one slit-jaw image showing the jet, it is impossible to provide accurate estimates of the jet's lifetime. An upward estimate of 4 min 14 s, or the time between three slit-jaw images, grossly outlasts the average established jet lifetime of 20–80 s, as given by Tian et al. (2014). This number can be further winnowed, albeit slightly, by considering how long the raster takes to scan across the jet. In that case, a lifetime of 3.75 min is calculated (see Sect 3.4.1).

3.5.2 Multiple flow components

Plasma outflows (blueshifted region along the spire) confirm the presence of real mass motions. The physical extent of the jet actually extends beyond what is inferred solely from SG blueshifts of Si IV (see, e.g., Fig. 3.4). The jet is traced down to its region of origin by analyzing the individual spectra, whose intensities reveal asymmetric profiles. These asymmetries are well-described by double-Gaussian fits to the observed Si IV line profiles. The primary component of the DG is representative of the typical TR redshifted material emitting beneath (i.e., below) the source region of the secondary component, which corresponds to the blueshifted jet material. By evaluating the secondary component, the behavior of the jet is elucidated.

Previous work has investigated the common appearance of asymmetrical emission lines formed in the corona and TR (see, e.g., Peter 2001, Hara et al. 2008, Tian et al. 2011, Yardley et al. 2021). As is the conclusion of this work, such line asymmetries are mostly attributed to the overlapping of background emission (primary component) and high-speed flows (secondary component). Tian et al. (2011) discovered a link between the secondary emission component and upward propagating disturbances seen in AIA. Ubiquitous, propagating torsional motions associated with dynamic features within the TR and chromosphere were first observed at small scales with IRIS and have been reported by De Pontieu et al. (2014a). Kayshap et al. (2018) attribute a change in Doppler shift of the secondary component from red to blue across network jets to twisting motions. For the event we describe here, however, the DG profiles are not interpreted as signatures of large-scale twist. One reason for this is that the secondary component remains blueshifted compared to the primary component, regardless of which side of the feature we regard. While there may be unresolved plasma motions that can be interpreted as small-scale torsional motions within the jet as evidenced by the non-thermal widths, a general, coherent overturning rotation of the structure is not supported by the observational data.

The blueward flow component associated with the jet material is fast enough that it might contribute to the solar wind if the magnetic fields that confine the jet open into the heliosphere. This secondary component exhibits vertical speeds up to 50–75 $\mathrm{km\,s^{-1}}$ (see Fig. 3.4). Comparing this to the sound speed in the source region of Si IV that forms in ionization equilibrium at around 80 000 K ($\approx 43\ \mathrm{km\,s^{-1}}$), these outward flows are supersonic. Such high-speed flows accelerate further as they ascend into progressively less dense plasma, and, if connected to an open field line within the CH, could escape into the solar wind. However, in order to be comparable with the solar wind speeds of a few

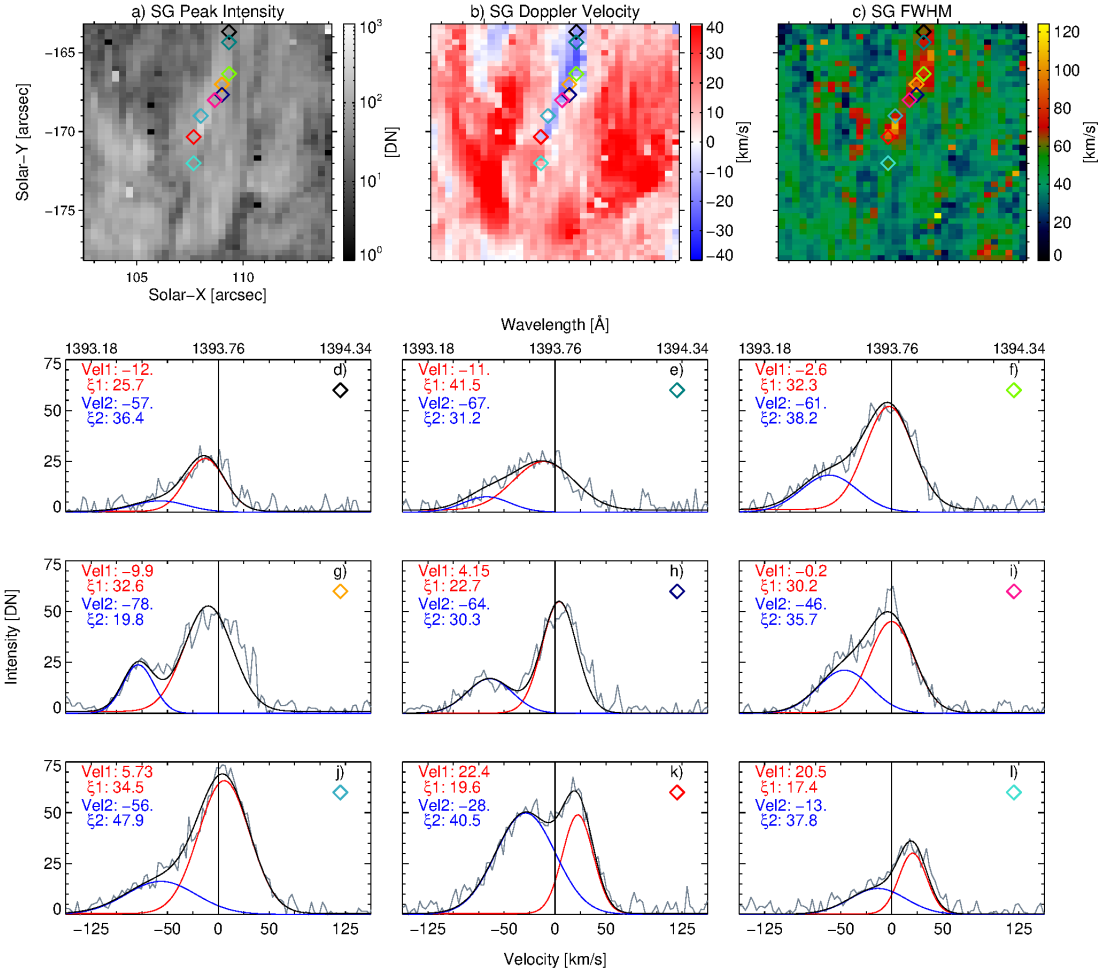

Figure 3.7: More DG-fitted spectra along jet. Panels (a)–(c) are the same as in Fig. 3.4, except for the colored diamond markers, which mark nine different pixels whose spectral profiles are shown in the bottom three rows. The style and layout of the spectra in panels (d)–(l) also match those for panels (g)–(i) in Fig. 3.4. This figure was originally published in the article's appendix.

hundred km s^{-1} recorded at 1 AU, these TR velocities would need to accelerate by at least a factor of six or more (and then the plasma has to be lifted out of the gravity field of the Sun). Hence, further acceleration would be required to eject this plasma as solar wind.

An extra source of energy to propel the jet into the solar wind could be derived from its non-thermal velocities. The jet has non-thermal widths of up to 45 km s^{-1} along its spire (see Fig. 3.4). If these unresolved motions are assumed to be wavelike in nature, caused by an Alfvén wave, an energy flux can be calculated and compared to what is needed in terms of extra energy. The Alfvén wave energy flux, f, can be estimated from:

$$f = \rho \, \xi^2 \, V_A \,, \tag{3.1}$$

where ρ is the mass density, ξ is the non-thermal velocity, and V_A is the Alfvén speed.

We use the average calculated non-thermal velocity of 34 $\mathrm{km\,s^{-1}}$ and the propagation speed estimated in Sect. 3.5.1, as well as a mass density of 1.8×10^{-14} $\mathrm{g\,cm^{-3}}$, which is calculated assuming a typical TR density of 10^{10} $\mathrm{cm^{-3}}$ (see Supplementary Materials in Tian et al. 2014). This results in an energy flux of 1.2 $\mathrm{kW\,m^{-2}}$, which is an order of magnitude greater than the 100–200 $\mathrm{W\,m^{-2}}$ needed on average to drive the solar wind (Schwenn 1990). Certainly, this is a significant amount of energy that could travel upward and boost the jet material at higher altitudes, thereby powering the solar wind. However, it could also be the case that the energy is not carried up high enough and is dissipated before it reaches a regime favorable for acceleration into the wind.

3.5.3 Magnetic driver

We can now look towards determining the jet's driver. We see signatures of increased activity in the Mg II line extending below the jet's line of expression in Si IV. This intense patch is the presumed region of origin for the jet as it is located above strong concentrations of vertical magnetic field.

Unfortunately, the behavior of the magnetic field at the jet's footpoint on both long and short timescales does not point unambiguously to a specific driving mechanism. Overall, no obvious signs of systematic flux cancelation are detected, but the positive flux linearly increases by around 9% across a period of three hours, which is potentially a sign of flux emergence (see Sect. 3.4.3 and Fig. 3.6). Interesting fluctuations, which are significant above the threshold set by the RMSE-level, are seen over the timescale during which the jet evolves. The sharp increase in positive magnetic flux immediately preceding the jet followed by a stark decrease during the jet's activity might be a signature of local reconnection (see the evolution in Fig. 3.6a from 07:20–07:25 UT indicated by the vertical lines). Similar magnetic field fluctuations before and after the event, while not quite as intense, could also be potential signatures of persistent jet activity in this region. However, a lack of IRIS coverage at those times makes it impossible to say whether or not this is true.

Though large-scale flux cancelation is not obvious from the HMI data due to a lack of noticeable available negative field concentrations, the movie of the magnetic field at the base of the jet shows merging and separation of positive magnetic clumps (see online movie associated with Fig. 3.3d). This could further support the theory of small-scale reconnection between the strong, resolved positive magnetic flux and nearby, unresolved areas of negative flux. The plausibility of such a scenario is demonstrated by Chitta et al. (2017a) who show that, using the balloon-borne mission SUNRISE (Solanki et al. 2010, 2017), small jets at the base of coronal loops are driven by flux cancelation and reconnection between large-scale, dominant polarity patches and small-scale elements of the opposite polarity. When comparing the same observational area using HMI, however, the non-dominant polarity is not clearly seen. Similarly, Chitta et al. (2019) observe transient magnetic flux emergence and cancelation events using the Swedish 1-m Solar Telescope (SST; Scharmer et al. 2003), which has five times the resolution as HMI. These transient magnetic events are seen at granular spatial scales and are found to appear in photospheric plage regions with a predominantly unipolar vertical magnetic field. The authors compare these observations with 3D radiation magnetohydrodynamic (rMHD)

simulations, verifying the presence of these magnetic events wherein emerging, small-scale and non-dominant polarity magnetic elements cancel with the surrounding dominant unipolar magnetic field. They find that these events can appear on even smaller spatial and temporal scales than that resolved by observations.

Chen et al. (2019) discuss the relationship between explosive events (EEs) and network jets. Two relevant categories of EEs that the authors define are for line profiles displaying either two peaks of comparable magnitude or enhancement at the blue wing, and they label these as categories (ii) and (iii), respectively. They find that EEs of the latter group are mainly located on network jets, away from the jet footpoints, while those of the former are either seen at the footpoints of jets or on transient compact brightenings not associated with network jets. For the jet evaluated in our study, the spectral profiles along the jet's spire show strong blue wing enhancements similar to those of category (iii), while closer to the base, some profiles exhibit category (ii)-type double peaks of commensurate intensity (see, e.g., Fig. 3.7, panel k). We find here that not only are the locations of the different profile types consistent with the previous work, but they also further the proposal of reconnection stemming from the shifting magnetic elements identified at the footpoint.

3.5.4 Location of energy release

In our observation, we find that the chromospheric plasma mainly exhibits downflows at the jet's base, whereas plasma sampling the TR at 0.1 MK is propelled upwards and thus blueshifted (see Sects. 3.4.1 and 3.4.2). This suggests that the actual location of energy release is located between the up- and downflows; in response to the energy deposition, the gas is propelled away from the release site and is channeled by the magnetic field in roughly up- and downward directions.

This is essentially the same setup as in an EE (Dere et al. 1989), where spectroscopic observations showed a bi-directional outflow from a reconnection site (Innes et al. 1997). In those EEs, the up- and downflows were seen in the same spectral line, meaning they happened at the same temperature. This might be due to the fact that the reconnection process is happening in a low-beta regime (well above the chromosphere) where the plasma is locally heated by plasmoid-mediated reconnection (Peter et al. 2019). Observations suggest that in (some) EUV bursts the X-type neutral point where the reconnection occurs is located within the chromosphere some 500 km above the photosphere, closer to where plasma beta is near unity (Chitta et al. 2017b). Still, if the energy deposition is strong enough, those EUV bursts could show up- and downflows in a TR line like Si IV (Peter et al. 2014), even if the reconnection is located almost as deep in the atmosphere as it is for Ellerman bombs (Georgoulis et al. 2002).

Our scenario that these network jets are driven from the top of the chromosphere is similar to earlier concepts, albeit in a different context. In previous works, a dichotomy of red- and blueshifts is seen in the QS TR (red) and corona (blue) in terms of temperature – below about 0.5 MK the plasma is redshifted, while above 0.5 MK it is blueshifted (Peter 1999, Peter and Judge 1999). This can be understood in terms of the 3D MHD model of Hansteen et al. (2010). In their work, the authors showed that the highest energy deposition per particle was found in the middle TR through episodic heating events. In

response, the plasma expands and produces the redshifts of the TR and blueshifts of the coronal lines.

Applying this model to our jet scenario, where energy is deposited at the top of the chromosphere, localized plasma heating creates a plug of increased pressure. The gas expands along field lines on both sides, which leads to downflows into the upper chromosphere seen in Mg II and upflows towards the corona seen in Si IV. While the ultimate driver might be found in the photospheric stretching of the magnetic field (e.g., Priest et al. 2002), the actual energy release that drives the jet we observe might be released at the top of the chromosphere.

3.6 Conclusion

We have observed a network jet with mass motions as inferred from secondary blueshifted components (20–70 km s^{-1}) in the spectral profiles. By comparing the magnetic field data with spectral information from the Mg II and Si IV lines, the jet has been followed from its footpoint location in the photosphere up through the chromosphere and into the TR.

We find that the energy that drives the network jet is released at the top of the chromosphere such that it drives parts of the plasma downwards into the chromosphere and other parts upwards into the upper atmosphere. The line broadening suggests that there should be sufficient surplus energy available to drive the jet plasma to join the solar wind originating from the coronal hole wherein this jet is embedded.

This work is serendipitous in that the raster slit happened to be scanning across roughly the length of a jet just as it was accelerating. However, the findings are limited to a single jet that is only seen in one SJI frame. Thus, future work should attempt to obtain similar observations that round out these shortcomings. Such similar observations would be dense raster scans located within or at the boundary of CHs at disk center with accompanying slit-jaw imagery. Preferably, the slit-jaw imagery would have a higher cadence than the observation presented herein (127 s) in order to capture any jet events in more than one frame; however, the cadence should not be too high so as to degrade the signal-to-noise beyond the point of utility. In addition to having multiple, similarly well-aligned raster observations of small-scale jets, higher resolution magnetic field data would help to better constrain possible driving mechanisms. Also, higher cadence SJIs would be useful for directly comparing the jet motions in the image plane with its motions along the LOS.

4 Beyond small-scale transients: A closer look at the diffuse quiet solar corona

[1] *This chapter's contents were published in Astronomy and Astrophysics under the same title by J. Gorman, L.P. Chitta, H. Peter, D. Berghmans, F. Auchère, R. Aznar Cuadrado, L. Teriaca, S.K. Solanki, C. Verbeeck, E. Kraaikamp, K. Stegen, and S. Gissot (2023), A&A 678, A188, DOI:10.1051/0004-6361/202345892. Reproduced with permission from Astronomy & Astrophysics, © ESO*

Contributions to the paper: *I analyzed the data, generated the figures, and wrote the first draft of the manuscript, the majority of which has been preserved after the editing and review process.*

4.1 Abstract

Within the quiet Sun corona imaged at 1 MK, much of the field of view consists of diffuse emission that appears to lack the spatial structuring that is so evident in coronal loops or bright points. Our aim is to determine if these diffuse regions are categorically different in terms of their intensity fluctuations and spatial configuration from the better-studied dynamic coronal features. We analyzed a time series of observations from Solar Orbiter's High Resolution Imager in the extreme ultraviolet to quantify the characterization of the diffuse corona at high spatial and temporal resolutions. We then compared this to the dynamic features within the field of view, mainly a coronal bright point. We find that the diffuse corona lacks visible structuring, such as small embedded loops, and that this is persistent over the 25 min duration of the observation. The intensity fluctuations of the diffuse corona, which are within ±5%, are significantly smaller in comparison to the coronal bright point; however, the total intensity observed in the diffuse corona is on the same order as the bright point. It seems inconsistent with our data that the diffuse corona is a composition of small loops or jets or that it is driven by discrete, small heating events that follow a power-law-like distribution. We speculate that small-scale processes such as magnetohydrodynamic turbulence might be energizing the diffuse regions, but at this point we cannot offer a conclusive explanation for the nature of this feature.

[1] The acknowledgments for this chapter are located at the end of the thesis.

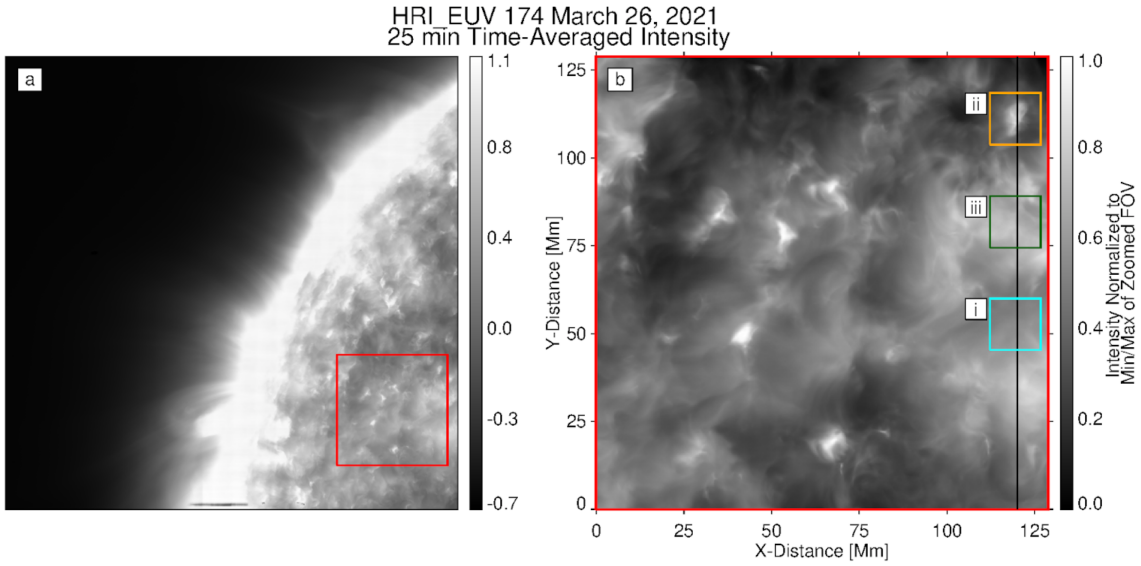

Figure 4.1: Observation summary. Panel (a): full field of view (FOV) covered in the 17.4 nm band of HRI_{EUV}. The red box outlines the zoomed-in FOV shown in panel (b). Both panels show the time-averaged normalized intensity (to the minimum and maximum in the area in panel b). Panel (b): location of the cut (vertical black line) that is used in the time–distance plot displayed in Fig. 4.2 and the intensity–distance plot shown in Fig. 4.3. The cyan box (i) and the orange box (ii) outline the diffuse region and the bright point used in Fig. 4.4. The green box (iii) outlines the loop-like features shown zoomed into in Fig. 4.6 (see Sect. 4.4.1).

4.2 Introduction

In studying the coronal heating problem, three main regions are acknowledged to have been observed within the corona. These are active regions (ARs), coronal holes (CHs), and the quiet Sun (QS). Active regions are the brightest and most dynamic portions of the corona, often associated with underlying strong magnetic field patches including sunspots, that consist of coronal loops as observed in the extreme ultraviolet (EUV) and X-rays. In contrast, CHs are the darkest portions in the solar corona in EUV and are attributed to open magnetic fields that connect the solar surface to the heliosphere. Physically beyond ARs and CHs, is the QS region. As the QS makes up the largest proportion of the solar surface, understanding the processes at work within this portion of the corona is crucial to understanding coronal heating.

Based on observations, a variety of small-scale dynamic features, such as nanoflares, coronal bright points, and jets, are all considered to be of high importance to balance the overall energy losses from the QS corona (e.g., Aschwanden et al. 2000, Hosseini Rad et al. 2021, Shen 2021, Chitta et al. 2021a). More recently, based on high spatial resolution and high-cadence EUV observations from the Extreme Ultraviolet Imager (EUI; Rochus et al. 2020) on board the Solar Orbiter (Müller et al. 2020), Berghmans et al. (2021) observed compact, isolated coronal brightenings termed campfires. A main characteristic of all these nanoflare-type heating events, including campfires, is that they are all clearly distinguishable from the local background coronal emission. Whether these observable

discrete heating events are sufficient to explain the energy losses from the QS corona is still an open question (Aschwanden et al. 2000, Chitta et al. 2021a). While much focus has been placed on these more distinguishable elements or events in the past, there remains much to be learned from the quieter portions of plasma that are devoid of these obvious localized transient brightenings. In particular, we are referring to the areas of seemingly stable and featureless EUV emission in the QS that we call the diffuse corona.

Diffuse emission associated with ARs has been studied in the past. Viall and Klimchuk (2011) looked at the diffuse portions of AR emission (i.e., areas not associated with any distinguishable loops or loop footpoints) and determined that these regions encompass a majority of the emitting portion of ARs; are only marginally less bright (10–35%) compared to AR loops; and are dynamically heated, as opposed to being energized by some steady process. Whether or not a similar significance and heating mechanism can be attributed to the diffuse corona in the QS remains to be seen.

In most studies, however, this diffuse emission is only considered a background. Usually, no particular consideration is given to it, apart from the urge to correct for (i.e., subtract) it when looking at features resolved in space and time embedded in this background.

In this work, we analyze the evolution of the diffuse quiescent corona observed with the high spatial and temporal resolution allowed by the EUI instrument. We compare the diffuse emission and its fluctuations to those seen in the more dynamic features within the observational field of view (FOV). We find that not only is the diffuse corona an enduring contributor of seemingly stable and unstructured emission, but that it also is more widespread and is therefore considered to be an important factor in the overall energy balance of the solar corona.

4.3 Observations

On March 26, 2021, Solar Orbiter (Müller et al. 2020) was located at a distance of 0.72 AU from the Sun on the far side with respect to Earth. The EUV High Resolution Imager ($\mathrm{HRI_{EUV}}$) on the Extreme Ultraviolet Imager was pointed toward the limb at a latitude of about 30°, and recorded images with very high cadence of 2 s (1.65 s exposure) between 23:32:20 UT and 23:57:18 UT (25 min).[2]

The $\mathrm{HRI_{EUV}}$ has a plate scale of 0.492″ $\mathrm{pixel^{-1}}$, which amounts to roughly 260 km $\mathrm{pixel^{-1}}$ on the Sun (as seen from Solar Orbiter) for this data set. The passband of $\mathrm{HRI_{EUV}}$ is centered at 17.4 nm, and its response peaks at temperatures of about 1 MK due to the presence of spectral lines of Fe IX (at 17.11 nm) and Fe X (at 17.45 nm and 17.72 nm). Before conducting our analysis, we aligned the level 2 (L2) data to remove the jitter in the image sequence as described in Chitta et al. (2022).

The region observed by EUI is a QS region outside CHs. While the target area was not visible from Earth-based telescopes, the Full Sun Imager (FSI) of EUI acquired images in the 304 Å and the 174 Å channels. These show a north polar coronal hole at latitudes

[2]Data release 4.0 2021-12. DOI: https://doi.org/10.24414/s5da-7e78

well above 60° north, while the FOV of HRI_{EUV} is below 55° north (i.e., located far from the coronal hole).

4.4 Results

We focus on the on-disk portion of these observations that also covered the limb and regions off the disk. An overview of the observational FOV, including the primary areas of interest for this study, is shown in Fig. 4.1. Panel (a) depicts the full FOV of HRI_{EUV}, and panel (b) shows a zoomed-in image of the on-disk portion of the observation that is of interest for this study. For both panels, the intensity shown was averaged over the entire 25 min observing time of this EUI sequence, and then was normalized by the minimum and maximum intensities within the zoomed-in FOV shown in panel (b). Thus, the image color scales in the full FOV and the zoomed-in FOV in Fig. 4.1 are different. With the above normalization for panel (b) it is limited between 0 and 1 and for panel (a), which contains pixels with both greater and weaker intensities, it ranges from −0.7 to 1.1.

4.4.1 Diffuse region, loop-like features, and coronal bright points

We find several distinct regions in the corona at ∼1 MK. There are dark patches (with normalized intensities of 0.25 or less), bright patches associated with loop-like structures and coronal bright points containing intensities at or near the saturation limit of the detector, and, finally, what we refer to as "diffuse" regions.

These diffuse regions are areas that seem to lack structure in both time and space. They are hazy portions seen throughout the FOV with time-averaged normalized intensities mostly in the range 0.25–0.6. An example patch of diffuse corona is outlined by the cyan box (panel i) in Fig. 4.1b. The diffuse corona appears to cover a significant area when compared to the brighter regions in the FOV. However, the diffuse corona lacks any of the obvious structuring that is associated with the well-studied structures of the quiet solar corona, such as coronal bright points that are composed of ∼10 Mm long loops (see, e.g., the review article on coronal bright points by Madjarska 2019).

Our analysis aims to compare these differing regions in both a qualitative and quantitative manner to determine the extent of this apparent discrepancy in terms of spatial structuring. For this we investigated a cut through the FOV that runs through these different features (black line in Fig. 4.1b): diffuse regions, loop-like features, and a coronal bright point. While many bright features are saturated in the exposure, in particular at the limb, this bright point is not. The intensity along this cut as a function of time is presented in a time–distance plot (see Fig. 4.2). It is evident from this plot that the bright point stretching from y = 106 Mm to 117 Mm shows intensity structuring in both space and time. The same also applies to the clear loop-like features situated around y = 65 Mm to 100 Mm. The bright point and the loop-like features appear to be continually evolving on spatial scales of roughly a few Mm and timescales on the order of a few minutes, although the loop-like features are less variable than the bright point.

The bright point is a typical small coronal bright point in appearance and size. It consists of a number of short coronal loops with the core region (Fig. 4.4 ii) having a size of

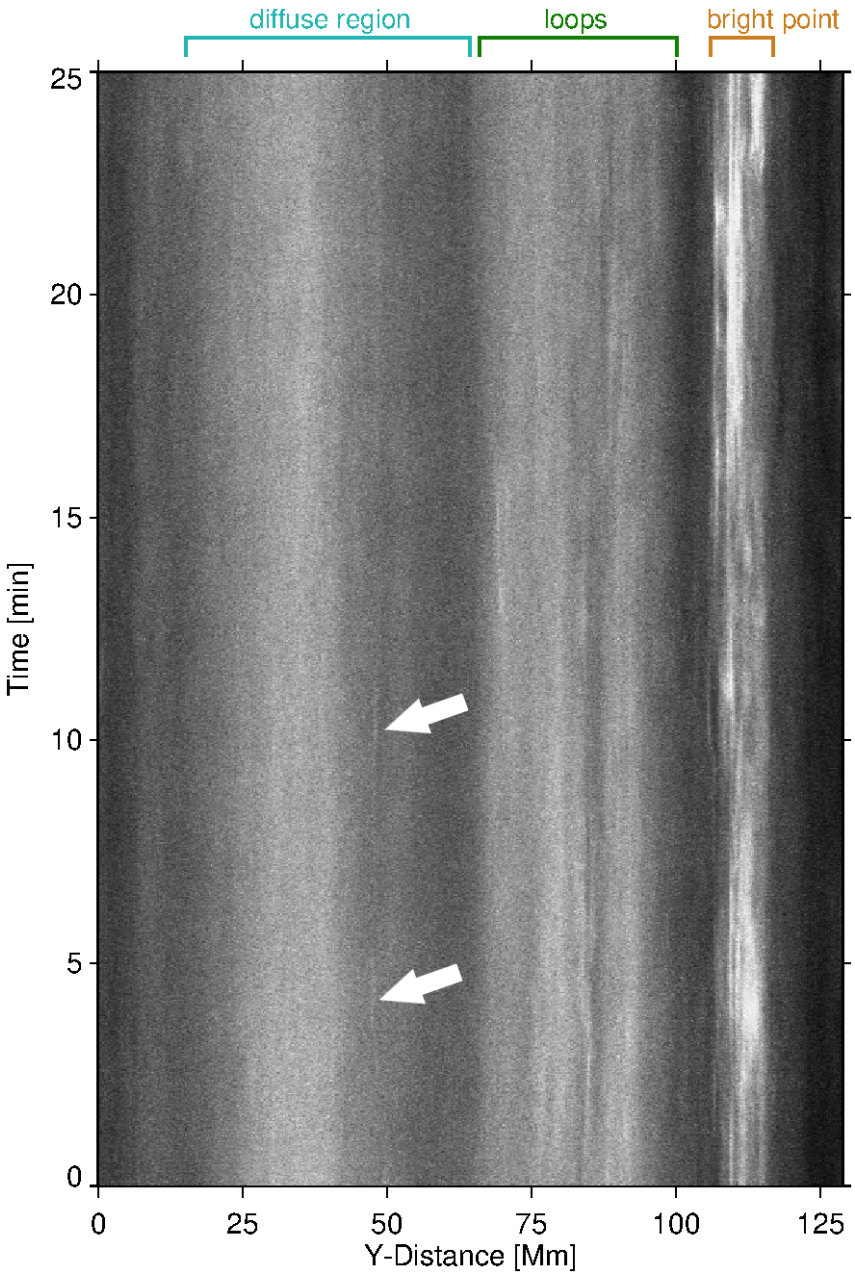

Figure 4.2: Temporal evolution of cut through the diffuse region and coronal bright point. This time–distance plot shows the intensity in $\mathrm{HRI_{EUV}}$ from along the cut (1 pixel in x) outlined by the black vertical line in Fig. 4.1b as it evolves over the entire 25 min observing time. The intensity is scaled linearly from 915 DN $\mathrm{s^{-1}}$ (black) to 2500 DN $\mathrm{s^{-1}}$ (white). Above the panel the locations in the y-direction of three types of regions are labeled. The two arrows indicate transient brightenings in the diffuse region (see Sects. 4.4.1, and 4.5.2).

just over 5 Mm (cf. Madjarska 2019). Such compact, small-loop-type bright points are found in abundance in the QS and have been used, for example, to determine the coronal rotation (Brajša et al. 2001, 2002), even though the spatial resolution of the older data was inadequate to sufficiently resolve the internal structure of the bright points. The

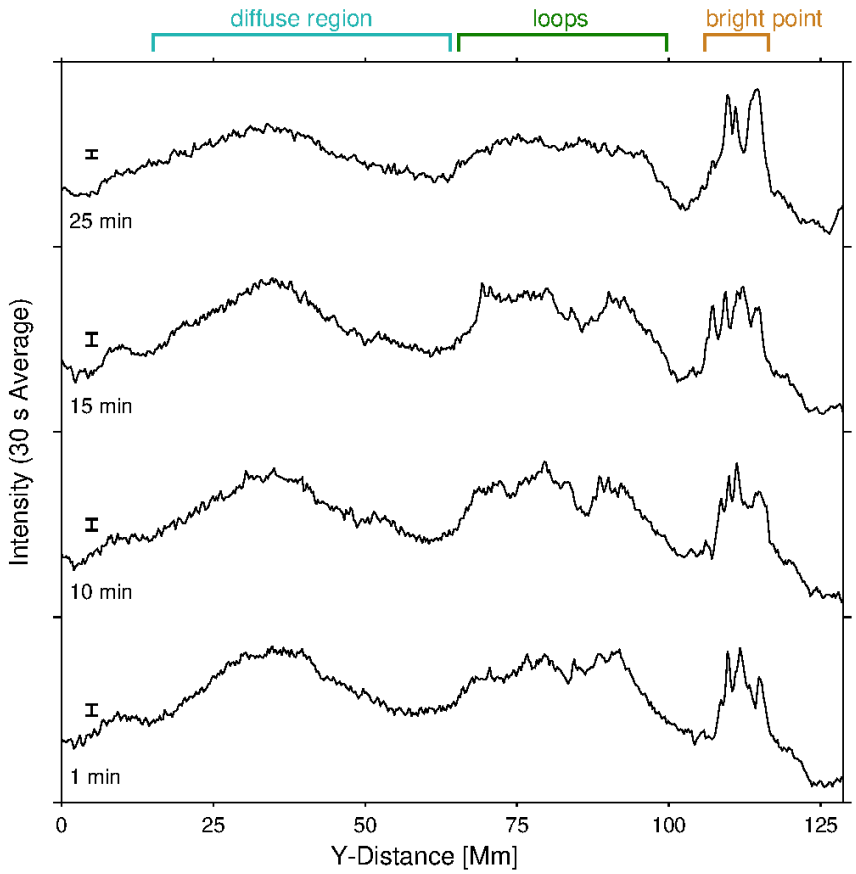

Figure 4.3: Spatial variability along a cut through a diffuse region, loop-like features, and a coronal bright point at four different times. This intensity–distance plot shows the intensity along the cut outlined by the black vertical line in Fig. 4.1b for several intervals of time during the observation. For each 30 s interval (15 time-consecutive images), the intensity at each pixel along the cut is averaged over that time period and plotted as a function of distance. Four of these light curves are shown as a stack: the bottom curve is the intensity–distance 30 s average (starting at 30 s) ending at 1 min, the curve directly above it is the 30 s average ending at 10 min, and so on. The black vertical bars with each curve show the maximum error for that curve (see Sect. 2.2.2). Above the panel the locations in the *y*-direction of the three types of regions are labeled (see Sects. 4.4.2 and 4.5.1).

region with loop-like features does not show clearly distinguishable loops, but (in the time-averaged image) elongated features reminiscent of loops (Fig. 4.6 iii). Because we concentrate in this study on the diffuse regions, we do not follow this up (see Sect. 4.4.3 for a further discussion of the loop-like features).

In contrast to these more dynamic features, the diffuse regions seen in Fig. 4.2 are invariable. The time–distance plot reveals the overall temporal stability of the diffuse corona. The emission is diffuse in the *y*-direction in a range of 15–65 Mm, with two seemingly distinct regions of differing intensity levels: a brighter portion between 15–42 Mm and a darker portion from 42–65 Mm. For both portions, there is a hazy quality that remains stable throughout the 25 min observing time on spatial scales comparable to

that of a supergranule. The brighter and darker sections both show no obvious jumps in intensity across their width. There is a small brightening at about $y = 48$ Mm occurring periodically over intervals of time limited to a few minutes (highlighted by arrows in Fig. 4.2). This could be categorized as an $\mathrm{HRI_{EUV}}$ campfire (see Berghmans et al. 2021). However, the brightening is only a few pixels in width and makes up only a small fraction of the overall emission in that region.

We note that the data shown in the space–time plot in Fig. 4.2 have a time cadence of only 2 s and a spatial sampling of 260 km on the Sun. This implies that transient small-scale features should be visible if they are present (down to those temporal and spatial scales).

4.4.2 Spatial and temporal variability

We now inspect the time–distance plot for a closer look at the difference between the coronal bright points and the diffuse regions. To this end, the intensity along the cut from Fig. 4.1b was averaged over each subsequent 30 s interval, which are displayed as line plots of time-averaged intensity versus distance, several of which are shown stacked in Fig. 4.3. Essentially, these stacked plots are horizontal cuts through Fig. 4.2 for a given time span.

Across these diffuse regions (i.e., $y = 15$–65 Mm), spatial changes in the intensity are gradual. As we discuss below, the small fluctuations seen in addition to this gradual variation are at the level of the calculated maximum error. The shape of the curve is also similar for each plot, although there are 5–10 min of separation between them. This implies that the diffuse corona behaves in a spatially coherent fashion over its entire extent corresponding to the scale of a supergranule of about 20 Mm.

The peak intensity in the brighter diffuse area (at $y \approx 35$ Mm) is only slightly less than, or even equal to the peak intensity seen in the bright point and loop-like features (in particular before $t = 15$ min). Conversely, the morphology of the loop-like features and coronal bright point changes markedly over time, and the intensity fluctuations within these features at each point in time varies significantly (i.e., well-above the maximum error). This further differentiates the characteristics of the diffuse regions from those of the bright points and loop-like features.

To quantitatively characterize the temporal stability of the diffuse corona, its relative intensity fluctuations provide clearer insight (Fig. 4.4). Here we compared the absolute and relative intensity variations of the diffuse corona (box (i) in Fig. 4.1b) to that within the coronal bright point (box ii). The absolute fluctuations are derived by simply spatially averaging the intensity within each of the sub-fields (a) to (d) for each snapshot. The relative fluctuations were then calculated by subtracting the overall time-averaged intensity within each sub-field from its spatially averaged intensity and then dividing this difference by the time-averaged intensity. Figures 4.4i and 4.4ii show which sub-fields of the observation are sampled, either from a diffuse region (a, b) or from a bright point (c, d).

The relative fluctuations in the sub-fields of the diffuse region (a, b) remain within a few percentage points (less than ±5%) over the entire 25 min (Figs. 4.4a, b). In contrast,

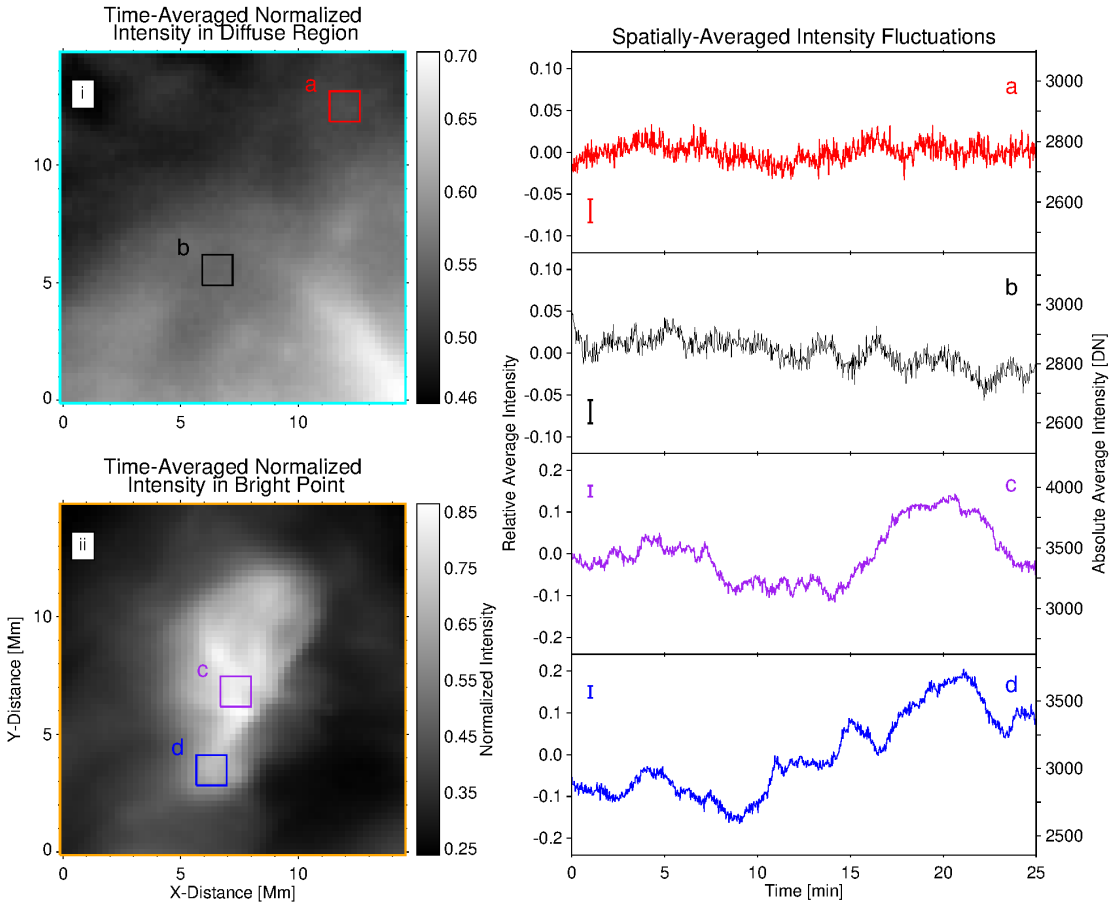

Figure 4.4: Intensity fluctuations in diffuse and bright point regions. The two left panels show the zoomed-in FOV covering the diffuse region (panel i) and bright point (panel ii) outlined by the cyan and orange boxes in Fig. 4.1b, respectively. Each image is the same time-averaged and normalized figure as shown in Fig. 4.1b, except the intensity range shown is further limited to the minimum and maximum for each zoomed-in FOV. Within the regions of interest, four smaller sub-fields (a)–(d) are outlined. Each of these boxes has the same area. The spatially averaged relative (left y-axis) and absolute (right y-axis) intensities for the respective sub-fields are plotted as a function of time on the right in panels (a)–(d). The vertical bars shown in each of these panels represent the maximum error for each time-series (see Sect. 2.2.2).

in the sub-fields of the coronal bright point (c, d), the intensity changes by over 10% on shorter timescales of about 5 min and can sway by up to almost 40% over the entire 25 min (Figs. 4.4c, d).

To judge the significance of these fluctuations, we have to compare the observed variability to the measurement errors. In Sect. 2.2.2 we discuss how we calculate the maximum estimated error. As a very rough estimate of this, for our current data set in regions that are moderately bright, the typical error of the intensity is on the order of 3%.

In general, the sub-fields of the bright point show trends that rise well above the level

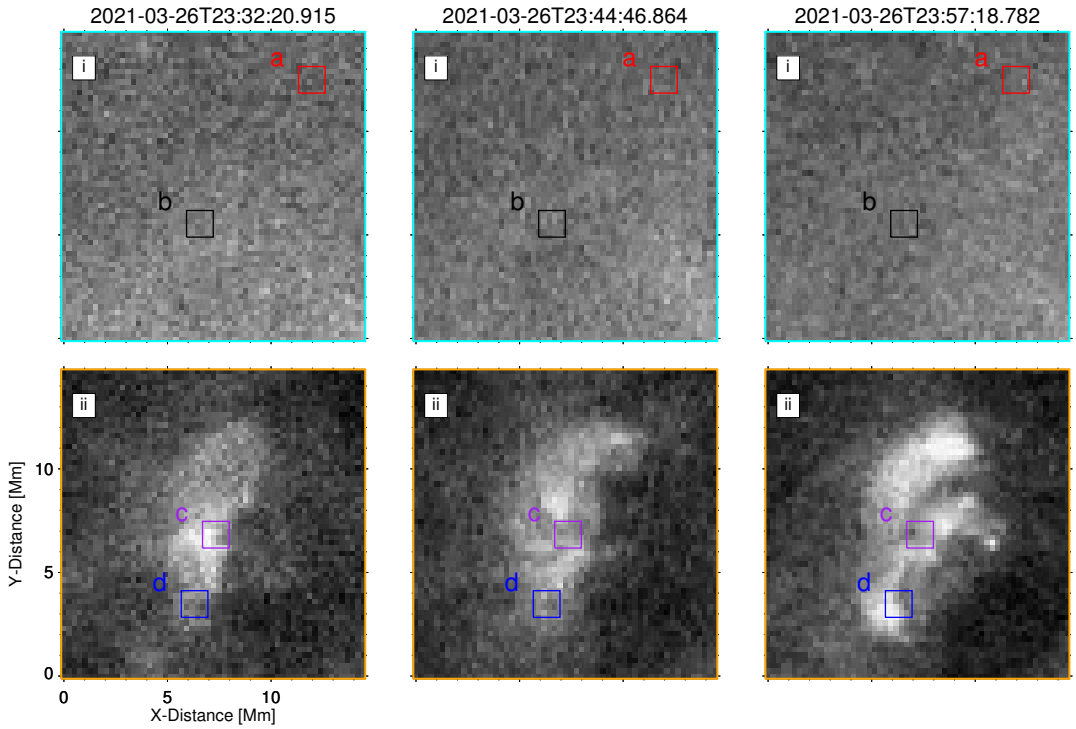

Figure 4.5: Snapshots of diffuse region and bright point without time-averaging. The snapshots at three times as indicated by the time stamps are shown in the three columns. The top row shows the diffuse region (marked i) and the bottom row the bright point (marked ii). Images are commonly scaled to the same minimum and maximum values of intensity. Boxes (a)–(d) have the same meaning as in Fig. 4.4 (see Sects. 4.4.2 and 4.5.1).

of the maximum estimated error, both on shorter and longer timescales. In contrast, in the diffuse regions the variability we see would essentially be consistent with measurement errors. There might be some dynamics within the diffuse regions with amplitudes just above the noise that persist for more than a few time steps, but these fluctuations are still smaller than the overall level of fluctuations over the observing period (of 25 min). While the fluctuations shown here are only for two subsections of each feature, the behavior is similar when more subsections are analyzed.

This relative temporal stability of the diffuse corona and the larger variability seen in the coronal bright point are further demonstrated using the respective snapshots, at three instances, without time-averaging (see Fig. 4.5). It is clear from these images that the diffuse region is not only temporally stable compared to the bright point, but it also lacks any distinguishable spatial structuring.

This time series analysis emphasizes that the diffuse corona, often considered as mere background, contributes a significant amount of the coronal emission in the QS (for a quantitative estimate of this contribution, see Sect. 4.5.1).

4.4.3 Region of loop-like features

[3] So far, we have concentrated on the properties of the diffuse region and compared them to the coronal bright point. Here we concentrate on an area with loop-like features (green box (iii) in Fig. 4.1). This region shows a spatio-temporal structuring of a higher degree than the diffuse region but much less variability than the bright point (see Fig. 4.2).

The time-averaged intensity map of this region shows distinct structures, even though it is not simple to attribute a particular nature to these features. The left panel of Fig. 4.6 shows a zoomed-in view of this area. In contrast to the diffuse region (Fig. 4.4i) it shows clear elongated structures. For simplicity we call these structures loop-like features.

The fluctuations seen in this region are comparable to or larger than in the diffuse region, but much less pronounced than in the bright point. This is evident when comparing the time variability near the center of the loop-like features (Fig. 4.6e) to the corresponding variability seen in the other regions (Figs. 4.4a–d).

The individual snapshots in this region of loop-like features are noisy, but still show distinct structures. For example, the first snapshot in Fig. 4.7 shows some short-lived individual compact brightenings and the last snapshot some elongated structures (at low contrast) from the bottom left to the top right. This presence of spatial structures is markedly different from the snapshots of the diffuse region (top row of Fig. 4.5). The levels of the count rates are comparable in the diffuse region and the loop-like features, hence noise cannot explain the absence of structures in the diffuse region.

From this discussion we conclude that the region with loop-like features (box (iii) in Fig. 4.1) hosts small-scale distinct features that cannot be identified in the diffuse region, even though the count rates are comparable. We can speculate if this region with loop-like features is in a transition phase from diffuse to more active, like the bright point, or vice versa. To draw solid conclusions on this a more comprehensive study of loop-like features would be required, in particular including data on the magnetic field configuration in the photosphere below.

4.5 Discussion

We note the general pervasiveness of the diffuse corona seen at temperatures of 1 MK with $\mathrm{HRI_{EUV}}$. These regions remain featureless in both time and space, and yet are relatively bright compared to the more dynamic features within the FOV. This naturally leads to questions about the significance of these regions in terms of their contribution to the emission of the 1 MK corona and about the possible heating mechanisms operating in such regions. Similarly, questions arise regarding the reasoning behind the lack of noticeable structuring and how this is related to the overall energy balance within the solar atmosphere.

[3] This section and Figs. 4.6 and 4.7 were published in the original article as Appendix B and have been modified slightly.

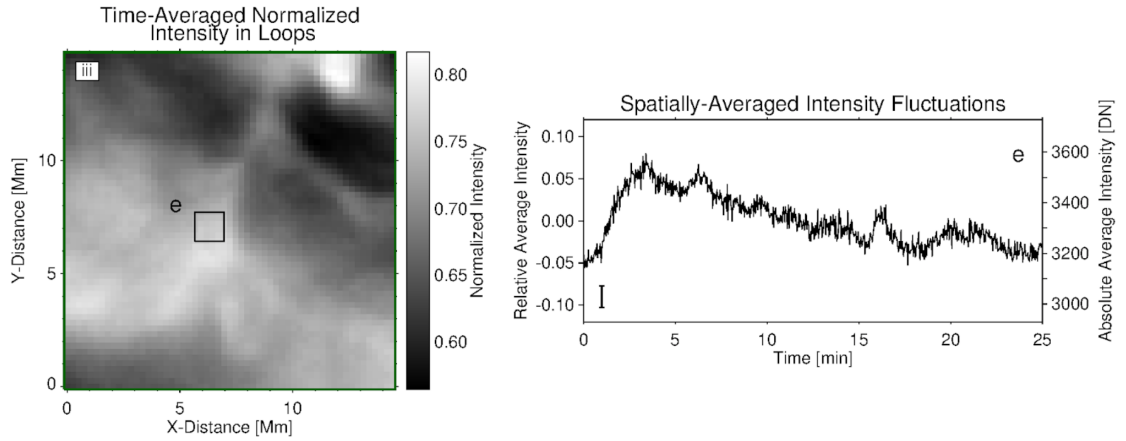

Figure 4.6: Intensity fluctuations in the region with loop-like features. The layout of this figure corresponds to Fig. 4.4. The left panel shows a zoomed-in image of the green box in Fig. 4.1b (region iii). Within this region a smaller sub-field (e) is outlined. This has the same area as the sub-fields in Figs. 4.4i and 4.4ii. The spatially averaged relative (left y-axis) and absolute (right y-axis) intensities for sub-field (e) are plotted as a function of time in the right panel. The vertical bar represents the maximum error for the time-series (see Sect. 2.2.2)

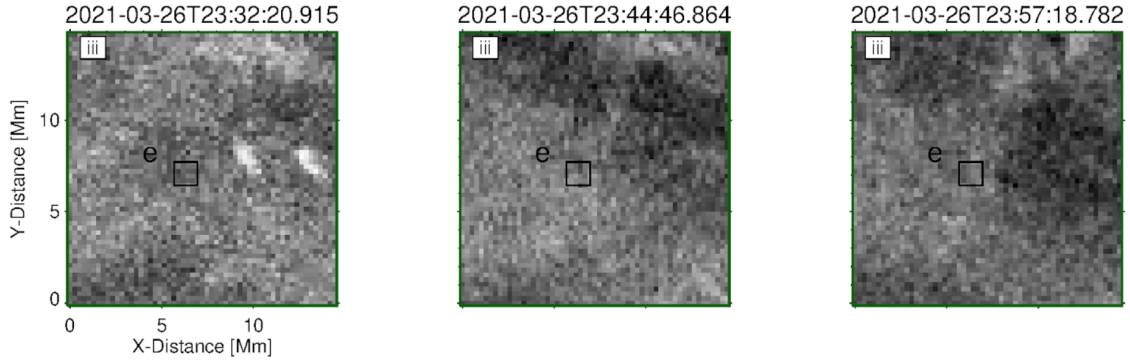

Figure 4.7: Snapshots of region with loop-like features without time averaging. This figure corresponds to Fig. 4.5. The snapshots are shown at three times, as indicated by the time stamps. Images are commonly scaled to the same minimum and maximum values of intensity. Box (e) has the same meaning as in Fig. 4.6 (see Sect. 4.4.3).

4.5.1 Contribution of diffuse regions to radiative losses

The intensity observed in the diffuse regions is relatively strong, even when compared with bright points. This is illustrated in Figs. 4.4a–d where we show the relative and absolute average intensity values [DN] within sub-fields of the diffuse and bright point regions. We see that, over the entire observing period, the time-averaged diffuse intensity (i.e., radiative flux per area) is about 80% that of the bright point (i.e., on the same order of magnitude). In addition, in Fig. 4.3, the peak intensities along the cut from the brighter diffuse portion (around y = 35 Mm) are very similar to those from the bright point (around y = 110 Mm) and are also about equal to those from the loop-like features sampled be-

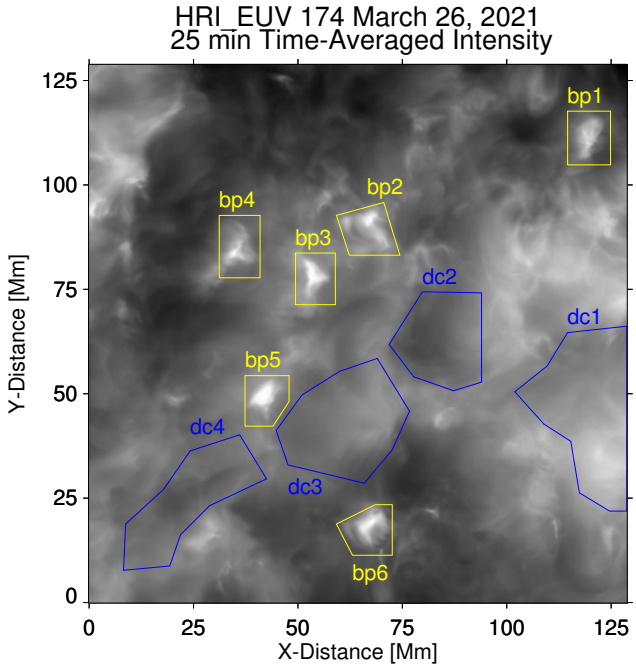

Figure 4.8: Grouping of diffuse coronal regions and bright points in QS. The intensity image is the same as Fig. 4.1b. The diffuse coronal regions (dc1 to dc4) are outlined in blue; the bright points (bp1 to bp6) are highlighted in yellow (see Sect. 4.5.1).

tween y = 65 Mm and 100 Mm. All of this points to the conclusion that the emission coming from the diffuse regions is non-negligible and should be an important consideration in any coronal heating model, in particular when considering that the diffuse corona can cover a large fraction of the QS.

We further investigate the significance of diffuse emission by conducting a rough estimate of the total emission contribution from the diffuse areas compared to the bright points within the FOV. For this we classify the regions in the FOV in Fig. 4.1b into areas covered by coronal bright points and diffuse regions by a simple by-eye estimate. These regions are marked and labeled in Fig. 4.8. Some of the bright points host a few pixels that are saturated on the detector. Hence our estimate for the bright point emission will be a lower limit only. However, this effect should be well below a factor of two and thus our calculation should be just fine for the order-of-magnitude estimate we aim for here.

Based on the integration of the emission from the respective diffuse and bright point areas, we find that the seemingly quiet diffuse areas provide almost 2.7 times more emission than the more dynamic features. Thus overall, the diffuse emission would dominate the QS radiative losses at around 1 MK, while discernible bright features would contribute a minor fraction, maybe half at best. This is not surprising since these diffuse regions defined by-eye also have almost three times more area than the bright points (see Fig. 4.8).

4.5.2 Diffuse quiet-Sun corona and small loops

The magnetic field is space-filling and is the driver behind the energetics of the corona. The work of Dowdy et al. (1986) described the solar magnetic scene as comprised of both (locally) open field lines expanding into funnels with height and small-scale closed loops that connect back to the surface. Based on studies of magnetic field extrapolations, these loops are expected to be rooted not only in the network regions at the edges of supergranules, but also in the internetwork within a few Mm of the network boundaries (Schrijver and Title 2003, Wiegelmann et al. 2010).

Quiet Sun observations reveal the presence of very short loops clearly distinguishable in EUV observations, only a few Mm long. They probably come at high coronal temperatures (Peter et al. 2013, Barczynski et al. 2017) as well as at lower TR temperatures (Hansteen et al. 2014). These short loops have lifetimes of only a few minutes. More recent observations also reveal the dynamic nature and substructure of such small EUV loops including propagating features (Mandal et al. 2021) and small jets associated with them (Chitta et al. 2021b). Transition region loops crossing a supergranular cell in the QS (i.e., with a length of ca. 20 Mm), have also been reported (e.g., Fig. 1 in Teriaca et al. 2004). However, all of these types of loops are discrete units and are far from space-filling.

Even so, the presence of loops in the QS would mean that we should expect the presence of small-scale coronal loops (a few Mm in length) in our observation even within the so-called diffuse areas. As discussed above, these smaller loops are expected to be dynamic, showing brightness fluctuations on timescales on the order of minutes (see also Reale 2010). Similar lifetimes of (magnetic) loops of a few minutes are also found based on magnetic field extrapolations from time series of high-resolution QS magnetograms (Wiegelmann et al. 2010). As a case in point, our observations do show such brightness fluctuations in the coronal bright points, which are indeed on shorter timescales compared to the 25 min of observed stability for our diffuse areas.

If the diffuse areas were composed of such smaller loops, then we would expect loop-like brightenings at some point during our analysis unless a different loop emission behavior is at play. We do see that there are a limited number of small-scale brightenings occurring within some diffuse portions of Fig. 4.2 (see white arrows) that last for a few minutes at a time and are only a few pixels in length (i.e., ~500 km in y-distance). These brightenings, however, are not ubiquitous, as would be expected for the typical picture of low-lying loops crisscrossing everywhere in the FOV. In addition, these small intensity enhancements barely rise above the level of the local diffuse region (or background). When compared to the intensity level local to the area of the brightening in the minutes before and after its enhancement, the brightening only rises to a level of 5% above this background.

The coherent spatial intensity variations on supergranular scales in these diffuse regions indicate that all the constituting smaller loops, if present, must evolve in unison, which is unlikely. Based on this, we think that the small coronal loops reported above may not be the source of emission from the diffuse regions. In that case we should occasionally see a transient brightening caused by one of the transient megameter-scale loops that have been

reported before, but we do not see them.

4.5.3 Diffuse quiet-Sun corona and jets

Chromospheric spicules (de Pontieu et al. 2007) and TR network jets (Tian et al. 2014) are other common small-scale jet features whose imprint should be seen everywhere on the QS. Spicules are chromospheric jets and are categorized as two types (de Pontieu et al. 2007). Type I spicules are longer-lived, and are seen to both rise and fall at the limb, remaining at chromospheric temperatures throughout their lifetime. Type II spicules are more transitory and often appear to shoot up before disappearing from chromospheric imaging channels, sometimes then appearing in the hotter channels imaging TR plasma (Pereira et al. 2014), which can also include the return flows when cooling back down from hotter temperatures (Bose et al. 2021). Spicules have typical speeds ranging from tens of $\mathrm{km\,s^{-1}}$ (type I) to 100 $\mathrm{km\,s^{-1}}$ (type II), lifetimes of several minutes, and characteristic lengths ranging from a few hundred to several thousand km (e.g., Tsiropoula et al. 2012, and references therein).

While spicular material is easiest to detect at the cooler temperatures found in the chromosphere and TR ($T \leq 10^5$ K), recent investigations show that there are exceptions to this where spicule signatures can be observed as corrugations in the EUV emission. For example, signatures have been found that the on-disk counterparts of spicules, namely dynamic fibrils, show EUV emission (Mandal et al. 2023). This might indicate higher temperatures of more than 10^5 K, although this is not yet conclusive (Henriques et al. 2016, Martínez-Sykora et al. 2018, Samanta et al. 2019). Similarly, coronal counterparts of network jets remain elusive (Kayshap et al. 2018, Gorman et al. 2022).

Small coronal jets are, in general, a common phenomenon in QS regions. In particular, recent EUI observations have shown an abundance of small-scale jets (e.g., Chitta et al. 2021b, Mandal et al. 2022). Small jets and their substructures (e.g., plasmoids) have recently also been observed in radio emission (e.g., Shimojo et al. 2017, Rodger et al. 2019). Still, the question remains whether highly dynamic small-scale features such as these jets or spicules can provide an explanation for the diffuse corona.

At 2 s cadence and about 500 km resolution, the observation from $\mathrm{HRI_{EUV}}$ that we analyze in this study could certainly pick up any spicules or network jets that showed counterparts in the EUV. However, we do not detect any such signatures in the far-reaching diffuse areas. This either means that these jets only very rarely reach coronal temperatures or at least that they do not get heated to 1 MK in the magnetic regime that is responsible for the diffuse emission. Another possibility could be that those small-scale jets that do reach coronal temperatures might lose their identity and structuring as their energy gets dissipated.

4.5.4 Diffuse quiet-Sun corona and small-scale heating events

The simple presence of a diffuse, seemingly featureless structure has implications for the heating mechanism that has to sustain the hot corona. The energization has to be either continuous or be concentrated in a very large number of small-scale heating events so that

this does not leave an imprint at the resolution of our observations. Hence, we explore the applicability of several proposed heating mechanisms for the diffuse corona. Clearly, we cannot relate our findings to all possible heating scenarios; instead, we picked those we considered most relevant for our study. We refer to recent reviews that discuss the heating problem in general (e.g., Klimchuk 2006), with respect to 3D models (e.g., Peter 2015), in terms of waves (e.g., Van Doorsselaere et al. 2020), or in light of field-line braiding (e.g., Pontin and Hornig 2020).

One heating scenario involves a power-law distribution of the number of brightening events with energy characterized by a slope of -2, at least for the smaller flare-like events with less than 10^{26} ergs (Hudson 1991). This requires there to be an increasingly larger number of distinct events on ever-smaller spatial and energy scales. These events would be so small that they are not yet resolvable by Sun-observing instruments (Parnell and Jupp 2000, Chitta et al. 2021a). To date, however, results are mixed regarding whether or not the energy distribution for impulsive heating events has the necessary slope to account for coronal heating (e.g., Berghmans et al. 1998, Krucker and Benz 1998, Aschwanden et al. 2000, Parnell and Jupp 2000, Pauluhn and Solanki 2007, Aschwanden and Shimizu 2013). It has also been pointed out that even if the power index is greater than 2, this is not necessarily sufficient to heat the QS (Berghmans 2002). Joulin et al. (2016) argue that regardless of the actual energy distribution slope, it is inherently unlikely to be able to detect high-frequency small-scale brightenings against the background coronal emission. The authors state that their study combined with the works of others before them shows that heating cannot be guaranteed to be observed as broken up into discrete events.

Perhaps such unresolved, impulsive brightenings are what is the cause behind the diffuse corona. If there were a sufficiently high number of small-scale events resulting in the diffuse emission that we see, they would still have to be driven in a spatially coherent fashion to create a diffuse region of about 10 to 20 Mm in size (i.e., the size of a supergranule). Considering the significant structuring found at the base below the corona, in the chromosphere, it is not very plausible that the diffuse corona is driven by small-scale events.

Should small-scale events drive and heat the diffuse coronal patches, we would also expect larger events in these regions. This is based on the finding that even on the smallest scales resolved to date, power-law-like distributions prevail (Berghmans et al. 2021). However, with two exceptions of events barely resolved by $\mathrm{HRI_{EUV}}$ (arrows in Fig. 4.2), we do not see any distinguishable transient brightenings in the diffuse regions (above the noise level). A more rigorous statistical analysis is required to draw a final conclusion, but at this point we consider it unlikely that individual events distributed through a power law could create a diffuse corona, as we observe here.

It is possible to speculate that some form of magnetohydrodynamic (MHD) turbulence might lead to energy dissipation far below the scales resolvable by current observations, thus creating a quasi-continuous heating in these regions. This would raise the question of why this should be operating in the diffuse regions, while other areas show much higher contrast in the coronal QS features. As this discussion would go far beyond the scope of this observational study, we refrain here from any further speculation.

4.5.5 Diffuse quiet-Sun corona and wave heating

If the energization of the hot diffuse QS corona has to be quasi-continuous, then wave heating could also be an option. In the first theoretical attempts to explain the hot outer atmosphere, heating through waves had already been suggested, at that time through the dissipation of sound waves (Biermann 1946, Schwarzschild 1948). On average, an energy flux of about 100 W m^{-2} is required to balance the energy losses of the corona in the QS (e.g., Withbroe and Noyes 1977), and in general upward-propagating magneto-acoustic waves have the potential to heat the plasma in magnetically closed structures (see, e.g., review by Arregui 2015). Such waves have been observed (e.g., Tomczyk et al. 2007), and they carry an energy flux sufficient to heat the QS corona (e.g., McIntosh et al. 2011).

Assuming that the upward-propagating waves are generated by p-mode leakage (e.g., de Moortel 2009), we might expect quite a homogeneous distribution of the energy flux into the upper atmosphere. In the photosphere we can expect a spatial structure on the scale of granulation; however, the rapid expansion of the magnetic field with height guiding the wave flux might quickly even out spatial inhomogeneities. However, a detailed investigation of the expansion of the underlying magnetic field in the diffuse coronal regions would be required before drawing any final conclusions on this.

In the time series of small sub-fields, some indications for three-minute oscillations might be found. A by-eye inspection of Figs. 4.4a–d suggests the presence of fluctuations on a timescale of a few minutes in the diffuse corona (panels a, b) and the bright point (c, d). If such fluctuations were present, that would indeed support the leakage of wave power from the photosphere into the higher atmospheric regions seen in the diffuse corona. Just as with the expansion of the magnetic field, a detailed analysis of a possible presence of three-minute oscillations in the diffuse regions will have to be conducted in the future.

4.6 Conclusions

We analyzed the diffuse quiescent corona observed by $\mathrm{HRI_{EUV}}$ on board Solar Orbiter. Here we find large patches of diffuse corona lacking resolvable physical structuring on scales below those of a supergranule (i.e., about 20 Mm). Even so, the coronal emission from these diffuse regions is of comparable brightness to the more dynamic features, such as loop-like features or coronal bright points. The spatial variability in the diffuse corona is below about 5%. The diffuse corona remains temporally stable throughout the observing period (i.e., for at least 25 min).

This diffuse regime is rather commonplace within the coronal makeup, contributing a large proportion of the emission seen at 1 MK, yet its underlying nature is still unclear. We consider it unlikely to be connected to features such as spicules or small loops. A power-law-like distribution of discrete heating events seems inconsistent with our observations. We speculate that small-scale processes like MHD turbulence or upward-propagating waves might be energizing the diffuse regions, but at this point we cannot offer a conclusive explanation for the nature of the diffuse regions.

The lower atmosphere in the QS shows a high degree of temporal and spatial complexity. This is illustrated, for example, by the cartoon suggested by Wedemeyer-Böhm et al.

(2009) in their Fig. 16. The diffuse region we investigated in this study might well be related to the mixture of structures in the internetwork, above and below the canopy domain. This would also fit into the interpretation of Milanović et al. (2023) of a diffuse region between network patches of the same polarity on opposite sides of a supergranular cell.

A more extensive investigation of this diffuse component of the QS corona, using increasingly diverse data sets would help to better estimate how common this component is, including observations of plasma at other temperatures. The brightness distribution in the diffuse patches, the lifetimes and size distributions of such diffuse patches, and whether wave patterns (of whatever nature) are commonly seen in them also need further consideration. Just as important will be studies combining EUV data with magnetic field measurements provided by the SO/PHI instrument (Solanki et al. 2020), for example. Finally, there is also a clear need for studies of possible heating mechanisms leading to such diffuse parts of the corona.

5 Conclusion

The content of this thesis explored the observational implications of the coronal heating balance, either through a detailed look at the evolution and energetics of a small-scale jet embedded in the TR, or through the analysis and discussion of the peculiar stability of the so-called diffuse corona at 1 MK.

Chapter 3 discussed the serendipitous observation of a TR network jet wherein the spectral slit was scanning across the jet's structure as it was being launched. This allowed for the identification of true mass motions belonging to the jet as determined via a high-speed, upward moving secondary component of Si IV emission along the LOS. Also, the analysis of the chromospheric Mg II emission showed that the jet was likely launched from the upper chromosphere, perhaps by magnetic reconnection occurring at these heights. This case study furthers the discussion of network jets being plausible contributors to the solar wind, and thus that they act as important components in the coronal energy balance.

A roughly half-hour observation of the 1 MK corona imaged by Solar Orbiter at high spatial and temporal resolutions was presented in Ch. 4. Within this data set, supergranular-sized regions of strong emission, as compared to dynamic features such as coronal loops and bright points, were seen to persist throughout the observing time without any obvious structuring in time or space. In other words, within the boundaries of these portions of diffuse corona there were no strong jumps or dips in intensity across their spatial domains and only low levels of fluctuations (on the order of the calculated noise) over the time domain. The result of this work was that the theories of nanoflare and wave heating were brought into question, as it was peculiar to see such a stable heating source occurring on such large scales throughout the FOV over such an extended period of time. While this observation certainly doesn't rule out either theory completely, it just requires that any big-picture heating models must take this component of the diffuse corona into account.

In the end and as previously mentioned, coronal heating is not actually believed to be caused by just one preferred theory or method, but rather is considered to be attributed to a mixture of causes. The puzzling and dichotomous outcomes of this thesis show just how complicated and nuanced the problem continues to be. On the one hand, impulsive and ubiquitous small-scale jets do appear to carry actual mass from the deeper layers upward. On the other hand, why these injections are not actually witnessed over large swaths of coronal area, despite the observation having a high temporal and spatial resolution, is unclear.

The question of coronal heating remains an interesting topic of many-sided splendor. Research into solar atmospheric dynamics continues to show that a large range of scales

are at play in the final heating equation, and that the solution cannot be boiled down to just one correct response. Future work to expand upon that found in this thesis would best include the continued analysis of the diffuse corona using observations from Solar Orbiter at even better resolutions. In particular, the use of co-temporal and co-spatial photospheric magnetic field data provided by Solar Orbiter's PHI instrument would be most helpful in examining the possible reasons behind the stability of the emission higher up. Also interesting would be to acquire an even longer data set to see just how stable the diffuse corona truly is, and if it is outlasting the expected turnover time for coronal structures cooled through basic radiative and conductive means. Of course, expansion of the network jet case study into a statistical study would also be helpful as future work and to allow for the cementing of the theories brought forth herein. It is likely that such similarly well-poised jet observations currently exist and are waiting for analysis. The only missing ingredient is the observer's motivation and ability to sift through what is out there.

Bibliography

Abbasvand, V., Sobotka, M., Švanda, M., Heinzel, P., García-Rivas, M., Denker, C., Balthasar, H., Verma, M., Kontogiannis, I., Koza, J., Korda, D., Kuckein, C., 2020, Observational study of chromospheric heating by acoustic waves, A&A, 642, A52, 2008.02688

Arregui, I., 2015, Wave heating of the solar atmosphere, Philosophical Transactions of the Royal Society of London Series A, 373, 20140 261–20140 261, 1501.06708

Aschwanden, M. J., Parnell, C. E., 2002, Nanoflare Statistics from First Principles: Fractal Geometry and Temperature Synthesis, ApJ, 572, 1048–1071

Aschwanden, M. J., Shimizu, T., 2013, Multi-wavelength Observations of the Spatio-temporal Evolution of Solar Flares with AIA/SDO. II. Hydrodynamic Scaling Laws and Thermal Energies, ApJ, 776, 132, 1308.5198

Aschwanden, M. J., Tarbell, T. D., Nightingale, R. W., Schrijver, C. J., Title, A., Kankelborg, C. C., Martens, P., Warren, H. P., 2000, Time Variability of the "Quiet" Sun Observed with TRACE. II. Physical Parameters, Temperature Evolution, and Energetics of Extreme-Ultraviolet Nanoflares, ApJ, 535, 1047–1065

Athay, R. G., Holzer, T. E., 1982, The role of spicules in heating the solar atmosphere, ApJ, 255, 743–752

Barczynski, K., Peter, H., Savage, S. L., 2017, Miniature loops in the solar corona, A&A, 599, A137, 1611.08513

Beckers, J. M., 1968, Solar Spicules (Invited Review Paper), Sol. Phys., 3, 367–433

Beckers, J. M., 1971, The Measurement of Solar Magnetic Fields, in Solar Magnetic Fields, (Ed.) R. Howard, vol. 43, p. 3

Benz, A. O., 2008, Flare Observations, Living Reviews in Solar Physics, 5, 1

Berghmans, D., 2002, Getting hot by nanoflares, in Solar Variability: From Core to Outer Frontiers, (Ed.) A. Wilson, vol. 2 of ESA Special Publication, pp. 501–508

Berghmans, D., Clette, F., Moses, D., 1998, Quiet Sun EUV transient brightenings and turbulence. A panoramic view by EIT on board SOHO, A&A, 336, 1039–1055

Berghmans, D., Auchère, F., Long, D. M., Soubrié, E., Mierla, M., Zhukov, A. N., Schühle, U., Antolin, P., Harra, L., Parenti, S., Podladchikova, O., Aznar Cuadrado, R., Buchlin, É., Dolla, L., Verbeeck, C., Gissot, S., Teriaca, L., Haberreiter, M., Katsiyannis, A. C., Rodriguez, L., Kraaikamp, E., Smith, P. J., Stegen, K., Rochus, P., Halain, J. P., Jacques, L., Thompson, W. T., Inhester, B., 2021, Extreme-UV quiet Sun brightenings observed by the Solar Orbiter/EUI, A&A, 656, L4, 2104.03382

Biermann, L., 1946, Zur Deutung der chromosphärischen Turbulenz und des Exzesses der UV-Strahlung der Sonne, Naturwiss., 33, 118–119

Boerner, P., Edwards, C., Lemen, J., Rausch, A., Schrijver, C., Shine, R., Shing, L., Stern, R., Tarbell, T., Title, A., Wolfson, C. J., Soufli, R., Spiller, E., Gullikson, E., McKenzie, D., Windt, D., Golub, L., Podgorski, W., Testa, P., Weber, M., 2012, Initial Calibration of the Atmospheric Imaging Assembly (AIA) on the Solar Dynamics Observatory (SDO), Sol. Phys., 275, 41–66

Bogdan, T. J., Carlsson, M., Hansteen, V. H., McMurry, A., Rosenthal, C. S., Johnson, M., Petty-Powell, S., Zita, E. J., Stein, R. F., McIntosh, S. W., Nordlund, Å., 2003, Waves in the Magnetized Solar Atmosphere. II. Waves from Localized Sources in Magnetic Flux Concentrations, ApJ, 599, 626–660

Bose, S., Henriques, V. M. J., Joshi, J., Rouppe van der Voort, L., 2019, Characterization and formation of on-disk spicules in the Ca II K and Mg II k spectral lines, A&A, 631, L5, 1910.05533

Bose, S., Rouppe van der Voort, L., Joshi, J., Henriques, V. M. J., Nóbrega-Siverio, D., Martínez-Sykora, J., De Pontieu, B., 2021, Evidence of the multi-thermal nature of spicular downflows. Impact on solar atmospheric heating, A&A, 654, A51, 2108.02153

Brajša, R., Wöhl, H., Vršnak, B., Ruždjak, V., Clette, F., Hochedez, J. F., 2001, Solar differential rotation determined by tracing coronal bright points in SOHO-EIT images. I. Interactive and automatic methods of data reduction, A&A, 374, 309–315

Brajša, R., Wöhl, H., Vršnak, B., Ruždjak, V., Clette, F., Hochedez, J. F., 2002, Solar differential rotation determined by tracing coronal bright points in SOHO-EIT images. II. Results for 1998/99 obtained with interactive and automatic methods, A&A, 392, 329–334

Buchlin, É., Vial, J. C., 2007, Coronal Turbulence And Intermittency From Solar Orbiter Observations, in Second Solar Orbiter Workshop, (Eds.) E. Marsch, K. Tsinganos, R. Marsden, L. Conroy, vol. 641 of ESA Special Publication, p. 23

Chen, Y., Tian, H., Huang, Z., Peter, H., Samanta, T., 2019, Investigating the Transition Region Explosive Events and Their Relationship to Network Jets, ApJ, 873, 79, 1901.11215

Chintzoglou, G., De Pontieu, B., Martínez-Sykora, J., Pereira, T. M. D., Vourlidas, A., Tun Beltran, S., 2018, Bridging the Gap: Capturing the Lyα Counterpart of a Type-II

Spicule and Its Heating Evolution with VAULT2.0 and IRIS Observations, ApJ, 857, 73, 1803.03405

Chitta, L. P., Peter, H., Solanki, S. K., Barthol, P., Gandorfer, A., Gizon, L., Hirzberger, J., Riethmüller, T. L., van Noort, M., Blanco Rodríguez, J., Del Toro Iniesta, J. C., Orozco Suárez, D., Schmidt, W., Martínez Pillet, V., Knölker, M., 2017a, Solar Coronal Loops Associated with Small-scale Mixed Polarity Surface Magnetic Fields, ApJS, 229, 4, 1610.07484

Chitta, L. P., Peter, H., Young, P. R., Huang, Y. M., 2017b, Compact solar UV burst triggered in a magnetic field with a fan-spine topology, A&A, 605, A49, 1706.08059

Chitta, L. P., Sukarmadji, A. R. C., Rouppe van der Voort, L., Peter, H., 2019, Energetics of magnetic transients in a solar active region plage, A&A, 623, A176, 1902.01650

Chitta, L. P., Peter, H., Young, P. R., 2021a, Extreme-ultraviolet bursts and nanoflares in the quiet-Sun transition region and corona, A&A, 647, A159, 2102.00730

Chitta, L. P., Solanki, S. K., Peter, H., Aznar Cuadrado, R., Teriaca, L., Schühle, U., Auchère, F., Berghmans, D., Kraaikamp, E., Gissot, S., Verbeeck, C., 2021b, Capturing transient plasma flows and jets in the solar corona, A&A, 656, L13, 2109.15106

Chitta, L. P., Peter, H., Parenti, S., Berghmans, D., Auchère, F., Solanki, S. K., Aznar Cuadrado, R., Schühle, U., Teriaca, L., Mandal, S., Barczynski, K., Buchlin, É., Harra, L., Kraaikamp, E., Long, D. M., Rodriguez, L., Schwanitz, C., Smith, P. J., Verbeeck, C., Zhukov, A. N., Liu, W., Cheung, M. C. M., 2022, Solar coronal heating from small-scale magnetic braids, A&A, 667, A166, 2209.12203

Chitta, L. P., Zhukov, A. N., Berghmans, D., Peter, H., Parenti, S., Mandal, S., Aznar Cuadrado, R., Schühle, U., Teriaca, L., Auchère, F., Barczynski, K., Buchlin, É., Harra, L., Kraaikamp, E., Long, D. M., Rodriguez, L., Schwanitz, C., Smith, P. J., Verbeeck, C., Seaton, D. B., 2023, Picoflare jets power the solar wind emerging from a coronal hole on the Sun, Science, 381, 867–872, 2308.13044

Couvidat, S., Rajaguru, S. P., Wachter, R., Sankarasubramanian, K., Schou, J., Scherrer, P. H., 2012, Line-of-Sight Observables Algorithms for the Helioseismic and Magnetic Imager (HMI) Instrument Tested with Interferometric Bidimensional Spectrometer (IBIS) Observations, Sol. Phys., 278, 217–240

de Moortel, I., 2009, Longitudinal Waves in Coronal Loops, Space Sci. Rev., 149, 65–81

de Pontieu, B., McIntosh, S., Hansteen, V. H., Carlsson, M., Schrijver, C. J., Tarbell, T. D., Title, A. M., Shine, R. A., Suematsu, Y., Tsuneta, S., Katsukawa, Y., Ichimoto, K., Shimizu, T., Nagata, S., 2007, A Tale of Two Spicules: The Impact of Spicules on the Magnetic Chromosphere, PASJ, 59, S655, 0710.2934

De Pontieu, B., McIntosh, S. W., Carlsson, M., Hansteen, V. H., Tarbell, T. D., Schrijver, C. J., Title, A. M., Shine, R. A., Tsuneta, S., Katsukawa, Y., Ichimoto, K., Suematsu, Y., Shimizu, T., Nagata, S., 2007, Chromospheric Alfvénic Waves Strong Enough to Power the Solar Wind, Science, 318, 1574

De Pontieu, B., Rouppe van der Voort, L., McIntosh, S. W., Pereira, T. M. D., Carlsson, M., Hansteen, V., Skogsrud, H., Lemen, J., Title, A., Boerner, P., Hurlburt, N., Tarbell, T. D., Wuelser, J. P., De Luca, E. E., Golub, L., McKillop, S., Reeves, K., Saar, S., Testa, P., Tian, H., Kankelborg, C., Jaeggli, S., Kleint, L., Martinez-Sykora, J., 2014a, On the prevalence of small-scale twist in the solar chromosphere and transition region, Science, 346, 1255732, 1410.6862

De Pontieu, B., Title, A. M., Lemen, J. R., Kushner, G. D., Akin, D. J., Allard, B., Berger, T., Boerner, P., Cheung, M., Chou, C., Drake, J. F., Duncan, D. W., Freeland, S., Heyman, G. F., Hoffman, C., Hurlburt, N. E., Lindgren, R. W., Mathur, D., Rehse, R., Sabolish, D., Seguin, R., Schrijver, C. J., Tarbell, T. D., Wülser, J. P., Wolfson, C. J., Yanari, C., Mudge, J., Nguyen-Phuc, N., Timmons, R., van Bezooijen, R., Weingrod, I., Brookner, R., Butcher, G., Dougherty, B., Eder, J., Knagenhjelm, V., Larsen, S., Mansir, D., Phan, L., Boyle, P., Cheimets, P. N., DeLuca, E. E., Golub, L., Gates, R., Hertz, E., McKillop, S., Park, S., Perry, T., Podgorski, W. A., Reeves, K., Saar, S., Testa, P., Tian, H., Weber, M., Dunn, C., Eccles, S., Jaeggli, S. A., Kankelborg, C. C., Mashburn, K., Pust, N., Springer, L., Carvalho, R., Kleint, L., Marmie, J., Mazmanian, E., Pereira, T. M. D., Sawyer, S., Strong, J., Worden, S. P., Carlsson, M., Hansteen, V. H., Leenaarts, J., Wiesmann, M., Aloise, J., Chu, K. C., Bush, R. I., Scherrer, P. H., Brekke, P., Martinez-Sykora, J., Lites, B. W., McIntosh, S. W., Uitenbroek, H., Okamoto, T. J., Gummin, M. A., Auker, G., Jerram, P., Pool, P., Waltham, N., 2014b, The Interface Region Imaging Spectrograph (IRIS), Sol. Phys., 289, 2733–2779, 1401.2491

De Pontieu, B., McIntosh, S., Martinez-Sykora, J., Peter, H., Pereira, T. M. D., 2015, Why is Non-Thermal Line Broadening of Spectral Lines in the Lower Transition Region of the Sun Independent of Spatial Resolution?, ApJ, 799, L12, 1710.06807

De Pontieu, B., Martínez-Sykora, J., Chintzoglou, G., 2017, What Causes the High Apparent Speeds in Chromospheric and Transition Region Spicules on the Sun?, ApJ, 849, L7, 1710.06803

Dere, K. P., Bartoe, J. D. F., Brueckner, G. E., 1989, Explosive Events in the Solar Transition Zone, Sol. Phys., 123, 41–68

Doschek, G. A., Warren, H. P., Laming, J. M., Mariska, J. T., Wilhelm, K., Lemaire, P., Schühle, U., Moran, T. G., 1997, Electron Densities in the Solar Polar Coronal Holes from Density-Sensitive Line Ratios of Si VIII and S X, ApJ, 482, L109–L112

Dowdy, J. F., J., Rabin, D., Moore, R. L., 1986, On the Magnetic Structure of the Quiet Transition Region, Sol. Phys., 105, 35–45

Ellerman, F., 1917, Solar Hydrogen “bombs”, ApJ, 46, 298

Georgoulis, M. K., Rust, D. M., Bernasconi, P. N., Schmieder, B., 2002, Statistics, Morphology, and Energetics of Ellerman Bombs, ApJ, 575, 506–528

Goldreich, P., Sridhar, S., 1995, Toward a Theory of Interstellar Turbulence. II. Strong Alfvenic Turbulence, ApJ, 438, 763

Gorman, J., Chitta, L. P., Peter, H., 2022, Spectroscopic observation of a transition region network jet, A&A, 660, A116, 2202.11375

Hansteen, V., De Pontieu, B., Carlsson, M., Lemen, J., Title, A., Boerner, P., Hurlburt, N., Tarbell, T. D., Wuelser, J. P., Pereira, T. M. D., De Luca, E. E., Golub, L., McKillop, S., Reeves, K., Saar, S., Testa, P., Tian, H., Kankelborg, C., Jaeggli, S., Kleint, L., Martínez-Sykora, J., 2014, The unresolved fine structure resolved: IRIS observations of the solar transition region, Science, 346, 1255757, 1412.3611

Hansteen, V. H., Hara, H., De Pontieu, B., Carlsson, M., 2010, On Redshifts and Blueshifts in the Transition Region and Corona, ApJ, 718, 1070–1078, 1001.4769

Hara, H., Watanabe, T., Harra, L. K., Culhane, J. L., Young, P. R., Mariska, J. T., Doschek, G. A., 2008, Coronal Plasma Motions near Footpoints of Active Region Loops Revealed from Spectroscopic Observations with Hinode EIS, ApJ, 678, L67

Harrison, R. A., 1997, EUV Blinkers: The Significance of Variations in the Extreme Ultraviolet Quiet Sun, Sol. Phys., 175, 467–485

Harrison, R. A., Harra, L. K., Brković, A., Parnell, C. E., 2003, A study of the unification of quiet-Sun transient-event phenomena, A&A, 409, 755–764

Heggland, L., De Pontieu, B., Hansteen, V. H., 2007, Numerical Simulations of Shock Wave-driven Chromospheric Jets, ApJ, 666, 1277–1283, astro-ph/0703498

Henriques, V. M. J., Kuridze, D., Mathioudakis, M., Keenan, F. P., 2016, Quiet-Sun Hα Transients and Corresponding Small-scale Transition Region and Coronal Heating, ApJ, 820, 124, 1602.04820

Heyvaerts, J., Priest, E. R., 1983, Coronal heating by phase-mixed shear Alfven waves., A&A, 117, 220–234

Hollweg, J. V., 1978, Alfvén waves in the solar atmosphere., Sol. Phys., 56, 305–333

Hosseini Rad, S., Alipour, N., Safari, H., 2021, Energetics of Solar Coronal Bright Points, ApJ, 906, 59

Hudson, H. S., 1991, Solar flares, microflares, nanoflares, and coronal heating, Sol. Phys., 133, 357–369

Innes, D. E., Inhester, B., Axford, W. I., Wilhelm, K., 1997, Bi-directional plasma jets produced by magnetic reconnection on the Sun, Nature, 386, 811–813

Ionson, J. A., 1978, Resonant absorption of Alfvénic surface waves and the heating of solar coronal loops., ApJ, 226, 650–673

Joulin, V., Buchlin, E., Solomon, J., Guennou, C., 2016, Energetic characterisation and statistics of solar coronal brightenings, A&A, 591, A148, 1605.02780

Kayshap, P., Murawski, K., Srivastava, A. K., Dwivedi, B. N., 2018, Rotating network jets in the quiet Sun as observed by IRIS, A&A, 616, A99, 1805.02517

Klimchuk, J. A., 2006, On Solving the Coronal Heating Problem, Sol. Phys., 234, 41–77, astro-ph/0511841

Krucker, S., Benz, A. O., 1998, Energy Distribution of Heating Processes in the Quiet Solar Corona, ApJ, 501, L213–L216

Leenaarts, J., Pereira, T. M. D., Carlsson, M., Uitenbroek, H., De Pontieu, B., 2013, The Formation of IRIS Diagnostics. II. The Formation of the Mg II h&k Lines in the Solar Atmosphere, ApJ, 772, 90, 1306.0671

Lemen, J. R., Title, A. M., Akin, D. J., Boerner, P. F., Chou, C., Drake, J. F., Duncan, D. W., Edwards, C. G., Friedlaender, F. M., Heyman, G. F., Hurlburt, N. E., Katz, N. L., Kushner, G. D., Levay, M., Lindgren, R. W., Mathur, D. P., McFeaters, E. L., Mitchell, S., Rehse, R. A., Schrijver, C. J., Springer, L. A., Stern, R. A., Tarbell, T. D., Wuelser, J.-P., Wolfson, C. J., Yanari, C., Bookbinder, J. A., Cheimets, P. N., Caldwell, D., Deluca, E. E., Gates, R., Golub, L., Park, S., Podgorski, W. A., Bush, R. I., Scherrer, P. H., Gummin, M. A., Smith, P., Auker, G., Jerram, P., Pool, P., Soufli, R., Windt, D. L., Beardsley, S., Clapp, M., Lang, J., Waltham, N., 2012, The Atmospheric Imaging Assembly (AIA) on the Solar Dynamics Observatory (SDO), Sol. Phys., 275, 17–40

Lin, H., Rimmele, T., 1999, The Granular Magnetic Fields of the Quiet Sun, ApJ, 514, 448–455

Littlefield, T. A., Thorley, N., 1979, The Zeeman Effect, pp. 183–195, Springer US, Boston, MA, ISBN 978-1-4684-1470-7

Liu, Y., Hoeksema, J. T., Scherrer, P. H., Schou, J., Couvidat, S., Bush, R. I., Duvall, T. L., Hayashi, K., Sun, X., Zhao, X., 2012, Comparison of Line-of-Sight Magnetograms Taken by the Solar Dynamics Observatory/Helioseismic and Magnetic Imager and Solar and Heliospheric Observatory/Michelson Doppler Imager, Sol. Phys., 279, 295–316

Madjarska, M. S., 2019, Coronal bright points, Living Reviews in Solar Physics, 16, 2

Mandal, S., Peter, H., Chitta, L. P., Solanki, S. K., Aznar Cuadrado, R., Teriaca, L., Schühle, U., Berghmans, D., Auchère, F., 2021, Propagating brightenings in small loop-like structures in the quiet-Sun corona: Observations from Solar Orbiter/EUI, A&A, 656, L16, 2111.08106

Mandal, S., Chitta, L. P., Peter, H., Solanki, S. K., Cuadrado, R. A., Teriaca, L., Schühle, U., Berghmans, D., Auchère, F., 2022, A highly dynamic small-scale jet in a polar coronal hole, A&A, 664, A28, 2206.02236

Mandal, S., Peter, H., Chitta, L. P., Cuadrado, R. A., Schühle, U., Teriaca, L., Solanki, S. K., Harra, L., Berghmans, D., Auchère, F., Parenti, S., Zhukov, A. N., Buchlin, É., Verbeeck, C., Kraaikamp, E., Rodriguez, L., Long, D. M., Schwanitz, C., Barczynski, K., Pelouze, G., Smith, P. J., Liu, W., Cheung, M. C., 2023, Signatures of dynamic fibrils at the coronal base: Observations from Solar Orbiter/EUI, A&A, 670, L3, 2212.05025

Martínez-Sykora, J., De Pontieu, B., De Moortel, I., Hansteen, V. H., Carlsson, M., 2018, Impact of Type II Spicules in the Corona: Simulations and Synthetic Observables, ApJ, 860, 116, 1805.06475

McGlasson, R. A., Panesar, N. K., Sterling, A. C., Moore, R. L., 2019, Magnetic Flux Cancellation as the Trigger Mechanism of Solar Coronal Jets, ApJ, 882, 16, 1906.06452

McIntosh, S. W., de Pontieu, B., Carlsson, M., Hansteen, V., Boerner, P., Goossens, M., 2011, Alfvénic waves with sufficient energy to power the quiet solar corona and fast solar wind, Nature, 475, 477–480

Milanović, N., Chitta, L. P., Peter, H., 2023, Diffuse solar coronal features and their spicular footpoints, A&A, 673, A81, 2303.13161

Müller, D., Nicula, B., Felix, S., Verstringe, F., Bourgoignie, B., Csillaghy, A., Berghmans, D., Jiggens, P., García-Ortiz, J. P., Ireland, J., Zahniy, S., Fleck, B., 2017, JHelioviewer. Time-dependent 3D visualisation of solar and heliospheric data, A&A, 606, A10, 1705.07628

Müller, D., St. Cyr, O. C., Zouganelis, I., Gilbert, H. R., Marsden, R., Nieves-Chinchilla, T., Antonucci, E., Auchère, F., Berghmans, D., Horbury, T. S., Howard, R. A., Krucker, S., Maksimovic, M., Owen, C. J., Rochus, P., Rodriguez-Pacheco, J., Romoli, M., Solanki, S. K., Bruno, R., Carlsson, M., Fludra, A., Harra, L., Hassler, D. M., Livi, S., Louarn, P., Peter, H., Schühle, U., Teriaca, L., del Toro Iniesta, J. C., Wimmer-Schweingruber, R. F., Marsch, E., Velli, M., De Groof, A., Walsh, A., Williams, D., 2020, The Solar Orbiter mission. Science overview, A&A, 642, A1, 2009.00861

Murawski, K., Musielak, Z. E., 2010, Linear Alfvén waves in the solar atmosphere, A&A, 518, A37

Nakariakov, V. M., Kolotkov, D. Y., 2020, Magnetohydrodynamic Waves in the Solar Corona, ARA&A, 58, 441–481

Narang, N., Arbacher, R. T., Tian, H., Banerjee, D., Cranmer, S. R., DeLuca, E. E., McKillop, S., 2016, Statistical Study of Network Jets Observed in the Solar Transition Region: a Comparison Between Coronal Holes and Quiet-Sun Regions, Sol. Phys., 291, 1129–1142, 1604.06295

Nishizuka, N., Nakamura, T., Kawate, T., Singh, K. A. P., Shibata, K., 2011, Statistical Study of Chromospheric Anemone Jets Observed with Hinode/SOT, ApJ, 731, 43

Osterbrock, D. E., 1961, The Heating of the Solar Chromosphere, Plages, and Corona by Magnetohydrodynamic Waves., ApJ, 134, 347

Panesar, N. K., Sterling, A. C., Moore, R. L., Chakrapani, P., 2016, Magnetic Flux Cancelation as the Trigger of Solar Quiet-region Coronal Jets, ApJ, 832, L7, 1610.08540

Panesar, N. K., Sterling, A. C., Moore, R. L., 2018, Magnetic Flux Cancelation as the Trigger of Solar Coronal Jets in Coronal Holes, ApJ, 853, 189, 1801.05344

Parker, E. N., 1983, Magnetic Neutral Sheets in Evolving Fields - Part Two - Formation of the Solar Corona, ApJ, 264, 642

Parker, E. N., 1987, Stimulated dissipation of magnetic discontinuities and the origin of solar flares., Sol. Phys., 111, 297–308

Parker, E. N., 1988, Nanoflares and the Solar X-Ray Corona, ApJ, 330, 474

Parnell, C. E., Jupp, P. E., 2000, Statistical Analysis of the Energy Distribution of Nanoflares in the Quiet Sun, ApJ, 529, 554–569

Pauluhn, A., Solanki, S. K., 2007, A nanoflare model of quiet Sun EUV emission, A&A, 462, 311–322, astro-ph/0612585

Pereira, T. M. D., Leenaarts, J., De Pontieu, B., Carlsson, M., Uitenbroek, H., 2013, The Formation of IRIS Diagnostics. III. Near-ultraviolet Spectra and Images, ApJ, 778, 143, 1310.1926

Pereira, T. M. D., De Pontieu, B., Carlsson, M., Hansteen, V., Tarbell, T. D., Lemen, J., Title, A., Boerner, P., Hurlburt, N., Wülser, J. P., Martínez-Sykora, J., Kleint, L., Golub, L., McKillop, S., Reeves, K. K., Saar, S., Testa, P., Tian, H., Jaeggli, S., Kankelborg, C., 2014, An Interface Region Imaging Spectrograph First View on Solar Spicules, ApJ, 792, L15, 1407.6360

Pesnell, W. D., Thompson, B. J., Chamberlin, P. C., 2012, The Solar Dynamics Observatory (SDO), Sol. Phys., 275, 3–15

Peter, H., 1999, Analysis of Transition-Region Emission-Line Profiles from Full-Disk Scans of the Sun Using the SUMER Instrument on SOHO, ApJ, 516, 490–504

Peter, H., 2001, On the nature of the transition region from the chromosphere to the corona of the Sun, A&A, 374, 1108–1120

Peter, H., 2015, What can large-scale magnetohydrodynamic numerical experiments tell us about coronal heating?, Philosophical Transactions of the Royal Society of London Series A, 373, 20150055–20150055

Peter, H., Judge, P. G., 1999, On the Doppler Shifts of Solar Ultraviolet Emission Lines, ApJ, 522, 1148–1166

Peter, H., Bingert, S., Klimchuk, J. A., de Forest, C., Cirtain, J. W., Golub, L., Winebarger, A. R., Kobayashi, K., Korreck, K. E., 2013, Structure of solar coronal loops: from miniature to large-scale, A&A, 556, A104, 1306.4685

Peter, H., Tian, H., Curdt, W., Schmit, D., Innes, D., De Pontieu, B., Lemen, J., Title, A., Boerner, P., Hurlburt, N., Tarbell, T. D., Wuelser, J. P., Martínez-Sykora, J., Kleint, L., Golub, L., McKillop, S., Reeves, K. K., Saar, S., Testa, P., Kankelborg, C., Jaeggli, S., Carlsson, M., Hansteen, V., 2014, Hot explosions in the cool atmosphere of the Sun, Science, 346, 1255726, 1410.5842

Peter, H., Huang, Y. M., Chitta, L. P., Young, P. R., 2019, Plasmoid-mediated reconnection in solar UV bursts, A&A, 628, A8, 1907.04335

Pneuman, G. W., 1968, Some General Properties of Helmeted Coronal Structures, Sol. Phys., 3, 578–597

Pontin, D. I., Hornig, G., 2020, The Parker problem: existence of smooth force-free fields and coronal heating, Living Reviews in Solar Physics, 17, 5

Priest, E. R., Heyvaerts, J. F., Title, A. M., 2002, A Flux-Tube Tectonics Model for Solar Coronal Heating Driven by the Magnetic Carpet, ApJ, 576, 533–551

Qi, Y., Huang, Z., Xia, L., Li, B., Fu, H., Liu, W., Sun, M., Hou, Z., 2019, On the Relation Between Transition Region Network Jets and Coronal Plumes, Sol. Phys., 294, 92, 1906.10353

Raouafi, N. E., Patsourakos, S., Pariat, E., Young, P. R., Sterling, A. C., Savcheva, A., Shimojo, M., Moreno-Insertis, F., DeVore, C. R., Archontis, V., Török, T., Mason, H., Curdt, W., Meyer, K., Dalmasse, K., Matsui, Y., 2016, Solar Coronal Jets: Observations, Theory, and Modeling, Space Sci. Rev., 201, 1–53, 1607.02108

Reale, F., 2010, Coronal Loops: Observations and Modeling of Confined Plasma, Living Reviews in Solar Physics, 7, 5, 1010.5927

Reale, F., 2014, Coronal Loops: Observations and Modeling of Confined Plasma, Living Reviews in Solar Physics, 11, 4

Rochus, P., Auchère, F., Berghmans, D., Harra, L., Schmutz, W., Schühle, U., Addison, P., Appourchaux, T., Aznar Cuadrado, R., Baker, D., Barbay, J., Bates, D., BenMoussa, A., Bergmann, M., Beurthe, C., Borgo, B., Bonte, K., Bouzit, M., Bradley, L., Büchel, V., Buchlin, E., Büchner, J., Cabé, F., Cadiergues, L., Chaigneau, M., Chares, B., Choque Cortez, C., Coker, P., Condamin, M., Coumar, S., Curdt, W., Cutler, J., Davies, D., Davison, G., Defise, J. M., Del Zanna, G., Delmotte, F., Delouille, V., Dolla, L., Dumesnil, C., Dürig, F., Enge, R., François, S., Fourmond, J. J., Gillis, J. M., Giordanengo, B., Gissot, S., Green, L. M., Guerreiro, N., Guilbaud, A., Gyo, M., Haberreiter, M., Hafiz, A., Hailey, M., Halain, J. P., Hansotte, J., Hecquet, C., Heerlein, K., Hellin, M. L., Hemsley, S., Hermans, A., Hervier, V., Hochedez, J. F., Houbrechts, Y., Ihsan, K., Jacques, L., Jérôme, A., Jones, J., Kahle, M., Kennedy, T., Klaproth, M., Kolleck, M., Koller, S., Kotsialos, E., Kraaikamp, E., Langer, P., Lawrenson, A., Le Clech', J. C., Lenaerts, C., Liebecq, S., Linder, D., Long, D. M., Mampaey, B., Markiewicz-Innes, D., Marquet, B., Marsch, E., Matthews, S., Mazy, E., Mazzoli, A., Meining, S., Meltchakov, E., Mercier, R., Meyer, S., Monecke, M., Monfort, F., Morinaud, G., Moron, F., Mountney, L., Müller, R., Nicula, B., Parenti, S., Peter, H., Pfiffner, D., Philippon, A., Phillips, I., Plesseria, J. Y., Pylyser, E., Rabecki, F., Ravet-Krill, M. F., Rebellato, J., Renotte, E., Rodriguez, L., Roose, S., Rosin, J., Rossi, L., Roth, P., Rouesnel, F., Roulliay, M., Rousseau, A., Ruane, K., Scanlan, J., Schlatter, P., Seaton, D. B., Silliman, K., Smit, S., Smith, P. J., Solanki, S. K., Spescha, M., Spencer, A., Stegen, K., Stockman, Y., Szwec, N., Tamiatto, C., Tandy, J., Teriaca, L., Theobald, C., Tychon, I., van Driel-Gesztelyi, L., Verbeeck, C., Vial, J. C., Werner, S., West, M. J.,

Westwood, D., Wiegelmann, T., Willis, G., Winter, B., Zerr, A., Zhang, X., Zhukov, A. N., 2020, The Solar Orbiter EUI instrument: The Extreme Ultraviolet Imager, A&A, 642, A8

Rodger, A. S., Labrosse, N., Wedemeyer, S., Szydlarski, M., Simões, P. J. A., Fletcher, L., 2019, First Spectral Analysis of a Solar Plasma Eruption Using ALMA, ApJ, 875, 163, 1902.01319

Rosenthal, C. S., Bogdan, T. J., Carlsson, M., Dorch, S. B. F., Hansteen, V., McIntosh, S. W., McMurry, A., Nordlund, Å., Stein, R. F., 2002, Waves in the Magnetized Solar Atmosphere. I. Basic Processes and Internetwork Oscillations, ApJ, 564, 508–524

Rosner, R., Tucker, W. H., Vaiana, G. S., 1978, Dynamics of the quiescent solar corona., ApJ, 220, 643–645

Rouppe van der Voort, L., De Pontieu, B., Pereira, T. M. D., Carlsson, M., Hansteen, V., 2015, Heating Signatures in the Disk Counterparts of Solar Spicules in Interface Region Imaging Spectrograph Observations, ApJ, 799, L3, 1412.4531

Rouppe van der Voort, L. H. M., De Pontieu, B., Hansteen, V. H., Carlsson, M., van Noort, M., 2007, Magnetoacoustic Shocks as a Driver of Quiet-Sun Mottles, ApJ, 660, L169–L172, astro-ph/0703535

Samanta, T., Tian, H., Yurchyshyn, V., Peter, H., Cao, W., Sterling, A., Erdélyi, R., Ahn, K., Feng, S., Utz, D., Banerjee, D., Chen, Y., 2019, Generation of solar spicules and subsequent atmospheric heating, Science, 366, 890–894, 2006.02571

Scharmer, G. B., Bjelksjo, K., Korhonen, T. K., Lindberg, B., Petterson, B., 2003, The 1-meter Swedish solar telescope, in Innovative Telescopes and Instrumentation for Solar Astrophysics, (Eds.) S. L. Keil, S. V. Avakyan, vol. 4853 of Society of Photo-Optical Instrumentation Engineers (SPIE) Conference Series, pp. 341–350

Scherrer, P. H., Schou, J., Bush, R. I., Kosovichev, A. G., Bogart, R. S., Hoeksema, J. T., Liu, Y., Duvall, T. L., Zhao, J., Title, A. M., Schrijver, C. J., Tarbell, T. D., Tomczyk, S., 2012, The Helioseismic and Magnetic Imager (HMI) Investigation for the Solar Dynamics Observatory (SDO), Sol. Phys., 275, 207–227

Schrijver, C. J., Title, A. M., 2003, The Magnetic Connection between the Solar Photosphere and the Corona, ApJ, 597, L165–L168

Schwarzschild, M., 1948, On Noise Arising from the Solar Granulation, ApJ, 107, 1–5

Schwenn, R., 1990, Large-Scale Structure of the Interplanetary Medium, p. 99

Shebalin, J. V., Matthaeus, W. H., Montgomery, D., 1983, Anisotropy in MHD turbulence due to a mean magnetic field, Journal of Plasma Physics, 29, 525–547

Shen, Y., 2021, Observation and modelling of solar jets, Proceedings of the Royal Society of London Series A, 477, 217, 2101.04846

Shimojo, M., Shibata, K., 2000, Physical Parameters of Solar X-Ray Jets, ApJ, 542, 1100–1108

Shimojo, M., Hudson, H. S., White, S. M., Bastian, T. S., Iwai, K., 2017, The First ALMA Observation of a Solar Plasmoid Ejection from an X-Ray Bright Point, ApJ, 841, L5, 1704.04881

Solanki, S. K., Barthol, P., Danilovic, S., Feller, A., Gandorfer, A., Hirzberger, J., Riethmüller, T. L., Schüssler, M., Bonet, J. A., Martínez Pillet, V., del Toro Iniesta, J. C., Domingo, V., Palacios, J., Knölker, M., Bello González, N., Berkefeld, T., Franz, M., Schmidt, W., Title, A. M., 2010, SUNRISE: Instrument, Mission, Data, and First Results, ApJ, 723, L127–L133, 1008.3460

Solanki, S. K., Riethmüller, T. L., Barthol, P., Danilovic, S., Deutsch, W., Doerr, H. P., Feller, A., Gandorfer, A., Germerott, D., Gizon, L., Grauf, B., Heerlein, K., Hirzberger, J., Kolleck, M., Lagg, A., Meller, R., Tomasch, G., van Noort, M., Blanco Rodríguez, J., Gasent Blesa, J. L., Balaguer Jiménez, M., Del Toro Iniesta, J. C., López Jiménez, A. C., Orozco Suarez, D., Berkefeld, T., Halbgewachs, C., Schmidt, W., Álvarez-Herrero, A., Sabau-Graziati, L., Pérez Grande, I., Martínez Pillet, V., Card, G., Centeno, R., Knölker, M., Lecinski, A., 2017, The Second Flight of the Sunrise Balloon-borne Solar Observatory: Overview of Instrument Updates, the Flight, the Data, and First Results, ApJS, 229, 2, 1701.01555

Solanki, S. K., del Toro Iniesta, J. C., Woch, J., Gandorfer, A., Hirzberger, J., Alvarez-Herrero, A., Appourchaux, T., Martínez Pillet, V., Pérez-Grande, I., Sanchis Kilders, E., Schmidt, W., Gómez Cama, J. M., Michalik, H., Deutsch, W., Fernandez-Rico, G., Grauf, B., Gizon, L., Heerlein, K., Kolleck, M., Lagg, A., Meller, R., Müller, R., Schühle, U., Staub, J., Albert, K., Alvarez Copano, M., Beckmann, U., Bischoff, J., Busse, D., Enge, R., Frahm, S., Germerott, D., Guerrero, L., Löptien, B., Meierdierks, T., Oberdorfer, D., Papagiannaki, I., Ramanath, S., Schou, J., Werner, S., Yang, D., Zerr, A., Bergmann, M., Bochmann, J., Heinrichs, J., Meyer, S., Monecke, M., Müller, M. F., Sperling, M., Álvarez García, D., Aparicio, B., Balaguer Jiménez, M., Bellot Rubio, L. R., Cobos Carracosa, J. P., Girela, F., Hernández Expósito, D., Herranz, M., Labrousse, P., López Jiménez, A., Orozco Suárez, D., Ramos, J. L., Barandiarán, J., Bastide, L., Campuzano, C., Cebollero, M., Dávila, B., Fernández-Medina, A., García Parejo, P., Garranzo-García, D., Laguna, H., Martín, J. A., Navarro, R., Núñez Peral, A., Royo, M., Sánchez, A., Silva-López, M., Vera, I., Villanueva, J., Fourmond, J. J., de Galarreta, C. R., Bouzit, M., Hervier, V., Le Clec'h, J. C., Szwec, N., Chaigneau, M., Buttice, V., Dominguez-Tagle, C., Philippon, A., Boumier, P., Le Cocguen, R., Baranjuk, G., Bell, A., Berkefeld, T., Baumgartner, J., Heidecke, F., Maue, T., Nakai, E., Scheiffelen, T., Sigwarth, M., Soltau, D., Volkmer, R., Blanco Rodríguez, J., Domingo, V., Ferreres Sabater, A., Gasent Blesa, J. L., Rodríguez Martínez, P., Osorno Caudel, D., Bosch, J., Casas, A., Carmona, M., Herms, A., Roma, D., Alonso, G., Gómez-Sanjuan, A., Piqueras, J., Torralbo, I., Fiethe, B., Guan, Y., Lange, T., Michel, H., Bonet, J. A., Fahmy, S., Müller, D., Zouganelis, I., 2020, The Polarimetric and Helioseismic Imager on Solar Orbiter, A&A, 642, A11, 1903.11061

Sridhar, S., Goldreich, P., 1994, Toward a Theory of Interstellar Turbulence. I. Weak Alfvenic Turbulence, ApJ, 432, 612

Stenflo, J. O., 1978, REVIEW: The measurement of solar magnetic fields, Reports on Progress in Physics, 41, 865–907

Teriaca, L., Madjarska, M. S., Doyle, J. G., 2002, Transition region explosive events: Do they have a coronal counterpart?, A&A, 392, 309–317

Teriaca, L., Banerjee, D., Falchi, A., Doyle, J. G., Madjarska, M. S., 2004, Transition region small-scale dynamics as seen by SUMER on SOHO, A&A, 427, 1065–1074

Tian, H., McIntosh, S. W., De Pontieu, B., Martínez-Sykora, J., Sechler, M., Wang, X., 2011, Two Components of the Solar Coronal Emission Revealed by Extreme-ultraviolet Spectroscopic Observations, ApJ, 738, 18, 1106.1141

Tian, H., DeLuca, E. E., Cranmer, S. R., De Pontieu, B., Peter, H., Martínez-Sykora, J., Golub, L., McKillop, S., Reeves, K. K., Miralles, M. P., McCauley, P., Saar, S., Testa, P., Weber, M., Murphy, N., Lemen, J., Title, A., Boerner, P., Hurlburt, N., Tarbell, T. D., Wuelser, J. P., Kleint, L., Kankelborg, C., Jaeggli, S., Carlsson, M., Hansteen, V., McIntosh, S. W., 2014, Prevalence of small-scale jets from the networks of the solar transition region and chromosphere, Science, 346, 1255711, 1410.6143

Tian, H., Yurchyshyn, V., Peter, H., Solanki, S. K., Young, P. R., Ni, L., Cao, W., Ji, K., Zhu, Y., Zhang, J., Samanta, T., Song, Y., He, J., Wang, L., Chen, Y., 2018, Frequently Occurring Reconnection Jets from Sunspot Light Bridges, ApJ, 854, 92, 1801.06802

Tomczyk, S., McIntosh, S. W., Keil, S. L., Judge, P. G., Schad, T., Seeley, D. H., Edmondson, J., 2007, Alfvén Waves in the Solar Corona, Science, 317, 1192

Tsiropoula, G., Tziotziou, K., Kontogiannis, I., Madjarska, M. S., Doyle, J. G., Suematsu, Y., 2012, Solar Fine-Scale Structures. I. Spicules and Other Small-Scale, Jet-Like Events at the Chromospheric Level: Observations and Physical Parameters, Space Sci. Rev., 169, 181–244, 1207.3956

Van Doorsselaere, T., Srivastava, A. K., Antolin, P., Magyar, N., Vasheghani Farahani, S., Tian, H., Kolotkov, D., Ofman, L., Guo, M., Arregui, I., De Moortel, I., Pascoe, D., 2020, Coronal Heating by MHD Waves, Space Sci. Rev., 216, 140, 2012.01371

Viall, N. M., Klimchuk, J. A., 2011, Patterns of Nanoflare Storm Heating Exhibited by an Active Region Observed with Solar Dynamics Observatory/Atmospheric Imaging Assembly, ApJ, 738, 24, 1106.4196

Wang, Y. M., 2020, Small-scale Flux Emergence, Coronal Hole Heating, and Flux-tube Expansion: A Hybrid Solar Wind Model, ApJ, 904, 199, 2104.04016

Wang, Y. M., Sheeley, N. R., J., Socker, D. G., Howard, R. A., Brueckner, G. E., Michels, D. J., Moses, D., St. Cyr, O. C., Llebaria, A., Delaboudinière, J. P., 1998, Observations of Correlated White-Light and Extreme-Ultraviolet Jets from Polar Coronal Holes, ApJ, 508, 899–907

Webb, D. F., Howard, T. A., 2012, Coronal Mass Ejections: Observations, Living Reviews in Solar Physics, 9, 3

Wedemeyer-Böhm, S., Lagg, A., Nordlund, Å., 2009, Coupling from the Photosphere to the Chromosphere and the Corona, Space Sci. Rev., 144, 317–350, 0809.0987

Welsch, B. T., 2015, The photospheric Poynting flux and coronal heating, PASJ, 67, 18, 1402.4794

Wentzel, D. G., 1974, Coronal Heating by Alfvén Waves, Sol. Phys., 39, 129–140

Wiegelmann, T., Solanki, S. K., Borrero, J. M., Martínez Pillet, V., del Toro Iniesta, J. C., Domingo, V., Bonet, J. A., Barthol, P., Gandorfer, A., Knölker, M., Schmidt, W., Title, A. M., 2010, Magnetic Loops in the Quiet Sun, ApJ, 723, L185–L189, 1009.4715

Withbroe, G. L., Noyes, R. W., 1977, Mass and energy flow in the solar chromosphere and corona., ARA&A, 15, 363–387

Yang, L., Peter, H., He, J., Tu, C., Wang, L., Zhang, L., Yan, L., 2018, Formation of Cool and Warm Jets by Magnetic Flux Emerging from the Solar Chromosphere to Transition Region, ApJ, 852, 16

Yardley, S. L., Brooks, D. H., Baker, D., 2021, Widespread occurrence of high-velocity upflows in solar active regions, A&A, 650, L10, 2106.01396

Yokoyama, T., Shibata, K., 1995, Magnetic reconnection as the origin of X-ray jets and Hα surges on the Sun, Nature, 375, 42–44

Young, P. R., Tian, H., Peter, H., Rutten, R. J., Nelson, C. J., Huang, Z., Schmieder, B., Vissers, G. J. M., Toriumi, S., Rouppe van der Voort, L. H. M., Madjarska, M. S., Danilovic, S., Berlicki, A., Chitta, L. P., Cheung, M. C. M., Madsen, C., Reardon, K. P., Katsukawa, Y., Heinzel, P., 2018, Solar Ultraviolet Bursts, Space Sci. Rev., 214, 120, 1805.05850

Publications

Refereed publications

- **Gorman, J.**, Chitta, L.P., Peter, H., Berghmans, D., Auchère, F., Aznar Cuadrado, R., Teriaca, L., Solanki, S.K., Verbeeck, C., Kraaikamp, E., Stegen, K., Gissot, S., 2023, A&A 678, A188, doi:10.1051/0004-6361/202345892
- **Gorman, J.**, Chitta, L.P., Peter, H., 2022, A&A 660, A116, doi:10.1051/0004-6361/202142995,

Conference proceedings

- April 2024: Joint Solar Orbiter, Parker Solar Probe, and DKIST meeting (San Antonio, TX, USA)
  Poster: *Diffuse Quiet Solar Corona*
- October 2021: Hinode-14/IRIS-11 Joint Science Meeting (online)
  Contributed talk: *Transition Region Network Jet in a Coronal Hole Traced Down to the Chromosphere and Photosphere*
- September 2021: European Solar Physics Meeting (ESPM)-16 (online)
  Flash presentation: *Spectroscopic Observation of a Transition Region Network Jet*

Acknowledgments

I would like to start by thanking my primary supervisor, Hardi Peter, not only for providing excellent scientific guidance throughout my studies, but also for his moral and administrative support during the various ups and downs that have come along during this time. From global pandemics to major personal upheavals, I am beyond thankful to have had such a kind and flexible boss to work with.

Secondly, I thank Pradeep Chitta for being a superb advisor and all-around solar physics encyclopedia, who not only holds a wealth of knowledge, but also easily dispenses it to needy PhD students such as myself. Always available for short and long questions, IDL tutorials, and great research ideas, he has been key to my (and many other students') success.

I also want to thank MPS and its directors, as well as the University of Göttingen, for the opportunity to pursue physics at such a high level. I feel fortunate to have had such a good experience overall and especially lucky to have been able to receive higher education in Germany. Not only did I expand my view of the world and what is possible, but I received a wealth of support during very drastic life changes that would likely not have been provided in other places. For that, I am exceedingly grateful.

Next, I would be remiss not to thank all the IMPRS students who made this experience fun and multi-dimensional, and also were there providing the highest levels of social support. From an interview week that felt like a surreal version of summer camp in February where I met most of my cohort (Tanayveer, Argiris, Amanda, Jesper, Dusan, Simon, and others), to the times spent meeting previous cohorts and students (Nils, Philipp, Hannah, Cosima, and Juxhin, amongst many) as well as new recruits (Nikolina, Jonathan, Yara, Paula, Jonas, and the list continues), I feel lucky to say that there are too many people I've enjoyed getting to experience this with to name.

Finally, I of course thank my family near and far for their support and encouragement. Always a phone call (and even one visit during the PhD) away, my Grandma has continued to be a source of light and enjoyment by providing perspective and friendship. My family back in Alaska provides a stable base to return to, no matter how far or long I stay away, and I hope we can continue to be connected despite the continuing difficult and irreversible changes that are occurring.

Ryan, my best friend and lifelong travel partner, I thank you for inspiring this whole journey and for staying by my side no matter what. I continue to learn many life lessons from you, and sometimes I even learn a little engineering. I must thank Kartoffel for

brightening my days when many have been anything but that, and for being an ever-constant joy. Last but never least, Lorelei, my daughter, motivation, and inspiration, you completely upended our worlds during this time and I marvel at how lucky I am to learn and love you every day. By far, the best thing to have come out of our time in Göttingen (you, and your sibling, whom we hope to meet post-PhD).

Acknowledgments to Ch. 3

We thank the anonymous referee for providing helpful comments and suggestions. This work was supported by the International Max-Planck Research School (IMPRS) for Solar System Science at the University of Göttingen. IRIS is a NASA small explorer mission developed and operated by LMSAL with mission operations executed at NASA Ames Research Center and major contributions to downlink communications funded by ESA and the Norwegian Space Centre. SDO/AIA and HMI imagery and data are courtesy of NASA/SDO and the AIA, EVE, and HMI science teams.

Acknowledgments to Ch. 4

We would like to thank the anonymous referee for helpful comments on this paper. This work was supported by the International Max-Planck Research School (IMPRS) for Solar System Science at the University of Göttingen. L.P.C. gratefully acknowledges funding by the European Union (ERC, ORIGIN, 101039844). Views and opinions expressed are however those of the author(s) only and do not necessarily reflect those of the European Union or the European Research Council. Neither the European Union nor the granting authority can be held responsible for them. Solar Orbiter is a mission of international cooperation between ESA and NASA, operated by ESA. The EUI instrument was built by CSL, IAS, MPS, MSSL/UCL, PMOD/WRC, ROB, LCF/IO with funding from the Belgian Federal Science Policy Office (BELSPO/PRODEX PEA 4000134088, 4000112292, 4000117262, and 4000134474); the Centre National d'Etudes Spatiales (CNES); the UK Space Agency (UKSA); the Bundesministerium für Wirtschaft und Energie (BMWi) through the Deutsches Zentrum für Luft- und Raumfahrt (DLR); and the Swiss Space Office (SSO).